

EXPERIMENTAL AND THEORETICAL STUDIES OF SPATIO-TEMPORAL INSTABILITIES IN NOVEL MATERIALS

F 49620-95-1-0208

AND

AASERT F49620-94-1-0255

Final Contract Report



Elias C. Aifantis, Stephen A. Hackney and Walter W. Milligan
Center for Mechanics, Materials and Instabilities
Michigan Technological University, Houghton MI 49931

Table of Contents

<i>Item</i>	<i>Page</i>
Executive summary.....	3
Personnel supported and list of publications resulting from research.....	4
1. Background and State of the Art.....	8
2. Fundamental Aspects.....	11
3. Applications.....	14
3.1 Gradient Theory at the Nanoscale: Dislocation Cores / Crack Tips / Interfaces.....	14
3.2 Gradient Theory at the Micro / Meso Scales: Dislocation Patterning / PSBs.....	17
3.3 Macroscale: Forming Limit Diagrams and Chip Formation.....	20
4. Size Effects: Gradient Theory Interpretation.....	26
5. Nanomechanics: Experiments and Modeling.....	28

AFRL-SR-BL-TR-00-

0273

REPORT DOCUMENTATION PAGE

Public reporting burden for this collection of information is estimated to average 1 hour per response, including the time for reviewing the data needed, and completing and reviewing this collection of information. Send comments regarding this burden estimate or any other aspect of this collection of information, including suggestions for reducing this burden to Department of Defense, Washington Headquarters Services, Directorate for Information Operations and Reports, 1215 Jefferson Davis Highway, Suite 1204, Arlington, VA 22202-4302. Respondents should be aware that notwithstanding any other provision of law, no person shall be subject to a collection of information if it does not display a currently valid OMB control number. PLEASE DO NOT RETURN YOUR FORM TO THE ABOVE ADDRESS.

1. REPORT DATE (DD-MM-YYYY) 19-06-2000		2. REPORT TYPE		3. DATES COVERED (From - To) 15/02/95 - 14/02/98 01/07/94 - 31/12/97	
4. TITLE AND SUBTITLE Experimental and Theoretical Studies of Spatio-Temporal Instabilities in Novel Materials				5a. CONTRACT NUMBER	
				5b. GRANT NUMBER F 49620-95-1-0208 F 49620-94-1-0255	
				5c. PROGRAM ELEMENT NUMBER	
6. AUTHOR(S) E.C. Aifantis, W.W. Milligan, S.A. Hackney				5d. PROJECT NUMBER	
				5e. TASK NUMBER	
				5f. WORK UNIT NUMBER	
7. PERFORMING ORGANIZATION NAME(S) AND ADDRESS(ES) Michigan Technological University Houghton, Michigan 49931				8. PERFORMING ORGANIZATION REPORT NUMBER	
9. SPONSORING / MONITORING AGENCY NAME(S) AND ADDRESS(ES) Air Force Office of Scientific Research Bolling Air Force Base, DC 20332				10. SPONSOR/MONITOR'S ACRONYM(S)	
				11. SPONSOR/MONITOR'S REPORT NUMBER(S)	
12. DISTRIBUTION / AVAILABILITY STATEMENT					
13. SUPPLEMENTARY NOTES					
14. ABSTRACT Progress has been made on fundamentals and applications of gradient theory to unresolved problems in mechanics and materials at all scales of observations: from nano and micro scales to meso and macro scales. After a general overview of gradient theory is provided and state of the art background, five specific areas of accomplishments are discussed. 1.Fundamental aspects of gradient theory including the origin of gradient terms and form of gradient coefficients; 2.The use of gradient elasticity to study cracks and dislocations, and, in particular, to eliminate the strain singularities at the crack tip and dislocation core as well as the use of gradient theory to discuss the problem of elastic and inelastic interfaces. 3.The use of gradient-dependent dislocation dynamics and gradient plasticity to understand the ladder like dislocation structure of persistent slip bands and their spatial arrangement; 4.The use of gradient theory to understand size effects on mechanical properties; 5.Experimental and modeling studies on nanostructured metals. These are delivered in two parts a) deformation and fracture mechanisms at the nanoscale for thin films, b) massive shear band formation at the nanoscale for bulk materials. A list of 50 refereed publications which appeared during the last years included.					
15. SUBJECT TERMS Plasticity, material instabilities, nanostructured materials					
16. SECURITY CLASSIFICATION OF:			17. LIMITATION OF ABSTRACT	18. NUMBER OF PAGES 63	19a. NAME OF RESPONSIBLE PERSON
a. REPORT	b. ABSTRACT	c. THIS PAGE			19b. TELEPHONE NUMBER (include area code) (906) 487-2518

5.1 Physical Aspects of Nanostructured Materials.....	28
5.2 Experimental Studies on Nanostructured Metal Thin Films.....	30
5.3. Experimental Studies on Bulk Nanostructures.....	39
5.4. Modeling the Mechanical Properties of Nanostructures.....	46
6. References.....	57

Executive summary

An interdisciplinary research was undertaken to understand the deformation mechanisms and model material instabilities and phenomena occurring at small volumes including nanoscale thin films and ultrafine grain bulk materials. Both theoretical and experimental studies were conducted. The theoretical studies were concerned with further developing the gradient theory in order to capture the occurrence of spatio-temporal instabilities, interpret the relevant scale effects, and use the results in a number of advanced technology related applications. The experimental studies were concerned with the fabrication and mechanical testing of novel materials at various scales of observation, as well as the determination of the relevant deformation mechanisms. An ultimate goal would be the derivation of appropriate constitutive equations for each scale of observation and the determination of the extent at which constitutive equation at the macroscale can be used to describe the mechanical behavior at the microscales. For convenience, we present the results in five major sections.

In the first section we give the background and the state of the art on gradient theory and material instabilities, as this field was advanced by the PI and his MTU co-workers, as well as by researchers elsewhere.

In the second section we discuss fundamental aspects of gradient theory including elasticity, plasticity and dislocation dynamics. The simplest possible gradient models for each of these three categories are presented and the governing differential equations are written down. The nature and microscopic interpretation of the gradient coefficients are discussed and explicit expressions for them are provided.

In the third section we discuss applications of gradient theory at the nanoscale (dislocation cores, crack tips, interfaces), the micro and meso scales (dislocation patterns and persistent slip bands) and the macroscale (shear bands in metal forming and cutting technology). In discussing the structure of the dislocation cores and crack tips at the nanoscale we show that gradient elasticity can eliminate the strain singularity in these regions and provide an estimate for the size of dislocation core and the cohesive zone at the crack tip. Similarly, the structure of elastic and inelastic interfaces at the nanoscale are discussed and the strain distribution is obtained for both hardening (transition solutions) and softening (localized solutions) interfaces. In discussing the problem of dislocation patterning at the microscale, the ladderlike dislocation structure of persistent slip bands (PSBs) is analyzed as an example. The Walgraef-Aifantis model of reaction-diffusion for dislocation populations is revisited by providing further support to the form of the diffusive and kinetic forms adopted in terms of the underlying dislocation mechanisms. Moreover, the process of persistent slip band precipitation until the whole specimen is filled up by PSBs, is described in terms of a gradient plasticity model at the mesoscale involving also stochastic arguments. Finally, two applications of gradient plasticity theory at the macroscale are discussed in terms of shear band formation and control during sheet metal forming and cutting.

In the fourth section we discuss the issue of size effect and the calibration of gradient theory in terms of simple experiments to determine the value of the gradient coefficients. We show, in particular, that simple gradient elasticity and plasticity models can be used for the interpretation of size effect experiments in torsion and bending as well as in nanoindentation. In fact, the aforementioned gradient models are calibrated by fitting the corresponding gradient coefficients to the experimental data. Such type of size effect tests can thus be used for the experimental determination of the gradient coefficients.

Finally, in the fifth section we discuss a number of experiments performed on a class of novel thin film and bulk materials at the nanoscale. The nanoscopic mechanisms of deformation are revealed and models based on these mechanisms are developed to interpret the observed behavior. Specifically,

experiments on thin film nanostructured metals found that deformation occurred by grain boundary sliding and grain rotation in nanostructured gold deformed at room temperature, with grain sizes less than 25nm. Bulk iron-copper nanostructures with grain sizes in the 100nm size range exhibited perfectly plastic behavior and intense shear banding as the primary deformation mechanism. The models developed are able to determine the effects of grain size on strength, and to determine the constitutive behavior of nanostructured metals; In particular, the shear band angles, the shear band widths and the asymmetry in tension and compression.

Personnel Supported

The contract supported three senior researchers at Michigan Technological University, as well as 7 graduate students and 4 visiting scientists. The senior personnel were:

Faculty

Elias C. Aifantis, Professor of Mechanical Engineering and Engineering Mechanics (PI)

Stephen A. Hackney, Professor of Metallurgical and Materials Engineering

Walter W. Milligan, Professor of Metallurgical and Materials Engineering

Graduate Students

Amy Bergstrom, John Carsley, Andrew Fisher, Jun Huang, Santo Padula, Jie Ning, X. Zhu

Journal Publications

1. E.C. Aifantis (1995) Pattern formation in plasticity, *International Journal of Engineering Science*, **33**, 2161-2178.
2. M. Yu. Gutkin, A.E. Romanov and E.C. Aifantis (1995) Nonuniform misfit dislocation distributions in nanoscale thin layers, *Nanostructured Materials*, **6**, 771-774.
3. H. Zhu, H.M. Zbib and E.C. Aifantis (1995) On the role of strain gradients in adiabatic shear banding, *Acta Mechanica* **111**, 111-124.
4. T.W. Webb and E.C. Aifantis (1995), Oscillatory fracture in polymeric materials, *International Journal of Solids and Structures*, **32**, 2725-2743.
5. D.J. Unger and E.C. Aifantis (1995) The asymptotic solution of gradient elasticity for mode III, *International Journal of Fracture*, **71**, R27-R32.
6. J.E. Carsley, J. Ning, W.W. Milligan, S.A. Hackney and E.C. Aifantis (1995) A simple, mixtures based model for the grain size dependence of strength in nanophase metals, *Nanostructured Materials*, **5**, 441-448.
7. M. Ke, S.A. Hackney, W.W. Milligan, and E.C. Aifantis (1995) Observation and measurement of grain rotation and plastic strain in nanostructured metal thin films, *Nanostructured Materials*, **5**, 689-698.
8. J.E. Carsley, W.W. Milligan, S.A. Hackney and E.C. Aifantis (1995) Glass-like behavior in a nanostructured Fe/Cu alloy, *Metallurgical Transactions*, **26A**, 2479-2481.

9. M. Yu. Gutkin, A.E. Romanov, and E.C. Aifantis(1996) Screw dislocation near a triple junction of phases with different elastic moduli I. General solution, *Physica Status Solidi*, **153**, 65-75.
- 10.D.J. Unger and E.C. Aifantis (1996) Analytical gradient plasticity solution for mode III, *International Journal of Fracture*, **74**, R75-R79.
- 11.I. Vardoulakis, G. Exadaktylos and E.C. Aifantis (1996) Gradient elasticity with surface energy: Mode III crack problem, *International Journal of Solids and Structures*, **33**, 4531-4559 .
- 12.G. Exadaktylos, I. Vardoulakis and E.C. Aifantis (1996) Cracks in gradient elastic bodies with surface energy, *International Journal of Fracture*, **79**, 107-119.
- 13.E.C. Aifantis (1996) Non-linearity, periodicity and patterning in plasticity and fracture, *International Journal of Non-Linear Mechanics*, **31**, 797-809.
- 14.G.E. Exadaktylos and E.C. Aifantis (1996) Two and three dimensional problems in gradient elasticity, *Journal of Mechanical Behavior of Materials*, **7**, 93-117.
- 15.J. Ning and E.C. Aifantis (1996) Gradient theory and its applications to stability analysis of materials and structures, *Journal of Mechanical Behavior of Materials*, **7**, 235-263.
- 16.Y.W. Wang, S.A. Majlessi, J. Ning and E.C. Aifantis (1996) The strain gradient approach for deformation localization and forming limit diagrams, *Journal of Mechanical Behavior of Materials*, **7**, 265-277.
- 17.J. Huang, W.W. Olson, J.W. Sutherland and E.C. Aifantis (1996) On the shear instability in chip formation in orthogonal machining, *Journal of Mechanical Behavior of Materials*, **7**, 279-292.
- 18.M. Yu. Gutkin and E.C. Aifantis (1996) Screw dislocation in gradient elasticity, *Scripta Materialia*, **35**, 1353-1358.
- 19.M. Yu. Gutkin and E.C. Aifantis (1997) Edge dislocation in gradient elasticity, *Scripta Materialia*, **36**, 129-135.
- 20.T.W. Webb, X.H. Zhu and E.C. Aifantis (1997) A simple method for calculating shear band angles for pressure-sensitive plastic materials, *Mech. Res. Comm.* **24**, 69-74.
- 21.T.W. Webb and E.C. Aifantis (1997) Crack growth resistance curves and stick-slip fracture instabilities, *Mech. Res. Comm.* **24**, 123-130.
- 22.T.W. Webb and E.C. Aifantis (1997) Loading rate dependence of stick-slip fracture in polymers, *Mech. Res. Comm.* **24**, 115-121
- 23.H.T. Zhu, H.M. Zbib, and E.C. Aifantis (1997) Strain gradients and continuum modeling of size effect in metal matrix composites, *Acta Mechanica*, **121**, 165-176.
- 24.X.H. Zhu, J.E. Carsley, W.W. Milligan, and E.C. Aifantis (1997) On the failure of pressure-sensitive plastic materials: Part I. Models of yield and shear band behavior, *Scripta Materialia*, **36**, 721-726.

25. J.E. Carsley, W.W. Milligan, X.H. Zhu and E.C. Aifantis (1997) On the failure of pressure-sensitive plastic materials: Part II. Comparisons with experiments on ultra fine grained Fe-10% Cu alloys, *Scripta Materialia*, **36**, 727-732.
26. J. Huang and E.C. Aifantis (1997) A note on the problem of shear localization during chip formation in orthogonal machining, *Journal of Materials Engineering & Performance*, **6**, 25-26.
27. M. Zaiser, M. Avlonitis and E.C. Aifantis (1998) Stochastic and deterministic aspects of strain localization during cyclic plastic deformation, *Acta Materialia*, **46**, 4143-4151.
28. J.E. Carsley, A. Fisher, W.W. Milligan and E.C. Aifantis (1998) Mechanical behavior of a bulk nanostructured iron alloy, *Metallurgical and Materials Transactions*, **29A**, 2261-2271.
29. D.A. Konstantinidis and E.C. Aifantis (1998) On the "anomalous" hardness of nanocrystalline materials, *Nanostructured Materials*, **10**, 1111-1118.
30. X.H. Zhu, S.A. Majlessi and E.C. Aifantis (1998) Predicting the forming limit diagram (FLD) for sheet metals with planar anisotropy, *SAE Transactions: Journal of Materials & Manufacturing*, **107**, 56-64.
31. M. Zaiser and E.C. Aifantis (1999) Materials instabilities and deformation patterning in plasticity, in: *Recent Research Devel. Metallurg. & Materials Sci. (Research Signpost)* **3**, 79-103.
32. E.C. Aifantis (1999), Gradient deformation models at nano, micro, and macro scales, *Journal Eng. Mater. Tech.* **121**, 189-202.
33. G.R. Shaik and W.W. Milligan (1997) Consolidation of nanostructured metal powder by rapid forging: processing, modeling, and subsequent mechanical behavior, *Metallurgical and Materials Transactions A*, **A28**, 895-904.

Conference Proceedings

34. J.E. Carsley, G.R. Shaik, W.W. Milligan and E.C. Aifantis (1997) Mechanical behavior of bulk nanostructured Fe-Cu alloys, in Chemistry and Physics of Nanostructures and Related Non-Equilibrium Materials, Eds. E. Ma, B. Fultz, R. Shull and J. Morral, 183-192, TMS, Warrendale, PA.
35. E.C. Aifantis (1995) Higher order gradients and size effects, in: Size-Scale Effects in the Failure Mechanisms of Materials and Structures, Ed. A. Carpinteri, pp. 231-242, Chapman and Hall, New York.
36. J. Ning and E.C. Aifantis (1995) Anisotropic and inhomogeneous plastic flow of fibrous composites, in: Microstructure-Property Interactions in Composite Materials, Ed. R. Pyrz, pp. 223-234, Kluwer, Netherlands.
37. E.C. Aifantis (1995) An account of spatiotemporal instabilities in deformation and fracture, in: Fracture and Plastic Instabilities, AMD-Vol. 200, Ed. N. Ghoniem, pp.1-7, ASME, New York.
38. J. Ning and E.C. Aifantis (1995) Strain gradients and size effects in composites, in: Micromechanics and Constitutive Modelling of Composite Materials, AMD-Vol. 202, Eds. I. Demir and H.M. Zbib, pp. 31-37, ASME, New York.

- 39.H. Zhu, H.M. Zbib and E.C. Aifantis (1995) Flow strength and size effect in metal matrix composites, in: Micromechanics and Constitutive Modelling of Composite Materials, AMD-Vol. 202, Eds. I. Demir and H.M. Zbib, pp. 103-115, ASME, New York.
- 40.T.W. Webb and E.C. Aifantis (1995) Stick-slip instabilities in fracture, in: Computational Mechanics (ICES 95), Vol 1, Eds. S.N. Atluri, G. Yagawa and T. A Cruse, pp. 1353-1358, Springer-Verlag, Berlin.
- 41.E.C. Aifantis (1995) Adiabatic shear banding: Higher-order strain gradient effects, in: Constitutive Laws: Theory, Experiments and Numerical Implementation, Eds. A.M. Rajendran and R.C. Batra, pp. 139-146, CIMNE, Barchelona.
- 42.B.S. Altan and E.C. Aifantis (1995) Propagation of SH waves in laminated composites, Proc. 2nd Int. Conf. Composites Eng. (ICCE2), Ed. D Hui, pp. 21-22, New Orleans.
- 43.J.E. Carsley, W.W. Milligan, S.A. Hackney and E.C. Aifantis (1996) Deformation mechanisms in bulk Fe - 10% Cu nanostructures, in: Processing and Properties of Nanocrystalline Materials, Eds. C. Suryanarayana et al, pp. 415-420, TMS, Warrendale, PA.
- 44.S. Hackney, M. Ke, W.W. Milligan and E.C. Aifantis (1996) Grain size and strain rate effects on the mechanisms of deformation and fracture in nanostructured metals, in: Processing and Properties of Nanocrystalline Materials, Eds. C. Suryanarayana et al, pp. 421-426, TMS, Warrendale, PA.
- 45.E.C. Aifantis (1998) Recent progress on gradient theory and applications, in IUTAM Symp. Material Instabilities in Solids, Eds. R. de Borst and E. van der Giessen, pp. 533-548, Wiley, Chichester.
- 46.E.C. Aifantis (1998) Gradient models in elasticity and plasticity, in: Constitutive and Damage Modeling of Inelastic Deformation and Phase Transformation, Ed. A.S. Khan, pp. 455-458, Neat Press, Maryland.
- 47.J. Huang, J.W. Sutherland and E.C. Aifantis (1998) Application of gradient theory in machining: Localized chip formation, in: Constitutive and Damage Modeling of Inelastic Deformation and Phase Transformation, Ed. A.S. Khan, pp. 353-357, Neat Press, Maryland.
- 48.A.Majlessi, X. Zhu and E.C. Aifantis (1998) Instability analysis in sheet materials with planar anisotropy, in: Constitutive and Damage Modeling of Inelastic Deformation and Phase Transformation, Ed. A.S. Khan, pp. 495-498, Neat Press, Maryland.

Book Chapter

- 49.W.W. Milligan, S.A. Hackney and E.C. Aifantis (1995) Constitutive modeling for nanostructured materials, Chapter 11 in: Continuum Models for Materials with Microstructure, Ed. H.B. Muhlhaus, pp. 379-393, Wiley.
- 50.J. Ning and E.C. Aifantis (1996) Anisotropic and inhomogeneous deformation of polycrystalline solids, in: Unified Constitutive Laws of Plastic Deformation, Eds. A.S. Krausz and K. Krausz, pp. 319-341, Academic Press, San Diego.

EXPERIMENTAL AND THEORETICAL STUDIES OF SPATIO-TEMPORAL INSTABILITIES IN NOVEL MATERIALS

1. Background and State of the Art

A gradient approach to deformation was suggested by Aifantis [1,2] in 1982 to describe plastic instabilities, including dislocation patterning and spatial characteristics of shear bands [3,4]. In [5] the theory was readily applied to deduce the wavelength of persistent slip bands in fatigued copper single crystals, the width of stationary shear bands in metal polycrystals, as well as the width, spacing and velocity of Portevin-Le Chatelier bands in Al-5% Mg alloys deformed under constant stress rate conditions. This initial work and subsequent articles by Walgraef and Aifantis [6], Zbib and Aifantis [7], Vardoulakis and Aifantis [8], and Mühlhaus and Aifantis [9] have contributed to appreciating the potential and applicability of the gradient approach to a variety of material instability problems ranging from metal fatigue and polycrystal/soil shear banding to the failure of concrete and liquefaction.

At the same time, other researchers have contributed substantially to the gradient approach: Coleman and co-workers [10,11] on mathematical aspects of the theory in relation to necking and shear banding; Kubin and co-workers [12,13] on the physical origin of the gradient terms for both dislocation and strain localization problems; Kratochvil and co-workers [14,15] on formulation aspects in relation to dislocation patterning; Hähner and co-workers [16,17] on microscopic and probabilistic aspects; and, finally, de Borst and co-workers [18,19], Belytschko and co-workers [20,21] and Tomita and co-workers [22] made significant contributions with emphasis on numerical aspects of the theory and its implementation to finite element codes. In parallel, other approaches (commonly referred to as non local damage theories [23]) have appeared in the literature as an outgrowth of earlier works by Eringen [24,25], and recent works by Bazant and co-workers [26-29]. Several outstanding issues and research directions have emerged as an outgrowth of the gradient approach. Among them, we mention the discrete dislocation simulation modelling (Amodeo and Ghoniem [30], Kubin [31], Groma and Pawley [32], Hirth, Rhee and Zbib [33]), the derivation of microscopic expressions for the gradient coefficients in terms of interatomic potentials (Triantafyllidis and Bardenhagen [34]; see also Triantafyllidis and Aifantis [35]), and the development of gradient thermodynamics theories (Maugin [36], Maugin and Muschik [37], Valanis [38], Polizzotto and Borino [39]; see also Aifantis [4]). Another major research direction that has been evolved rapidly as an outgrowth of the gradient approach was the development of finite element codes where the gradient term is used as a localization limiter, i.e. as a means of preserving well-posedness and mesh-size independence in boundary value problems for strain softening ductile behavior and damage softening brittle behavior. In addition to the pioneer contributions of Belytschko and co-workers, de Borst and co-workers, Tomita and co-workers mentioned earlier, one should include here the original work of Schreyer and Chen [40], Oka et al [41], as well as the more recent ones of Sluys and Wang [42], Ramaswamy and Aravas [43], Pijaudier-Cabot et al [44], Geers et al [45], Comi and Driemeier [46]. In this connection, the gradient thermodynamic damage models of Fremond and co-workers [47,48] should be mentioned. Recently, important contributions have been advanced by Estrin et al [49] on a dislocation based gradient plasticity model, Tvergaard and co-workers [50,51] on a gradient plasticity model for necking and hydroforming of thin sheets, and Molinari and co-workers [52,53] on the use of higher order gradients for interpreting deformation patterning. Moreover, we refer to interesting contributions on the gradient coefficients made by Frantziskonis [54-56], Zbib [57,58], Ning et al [59], and Carmeliet [60]. [In this connection, it is noted that gradient terms with specific expressions for the corresponding phenomenological coefficients appear in recent constitutive models for random composites (see, for example, Drugan and Willis [61], Buryachenko [62]). Finally, the work of Romanov and co-

workers [63-65] on gradient dislocation dynamics for monotonic deformation and thin film problems, as well as an alternative approach of discrete dislocation dynamics simulations by van der Giessen and Needleman [66,67] are worth noting. It may not be an exaggeration to state that the motivation for all aforementioned work on gradient theory with applications to dislocation and deformation patterning may be traced back to the original article of the author [3] (see also [5]). In particular, the strain gradient plasticity models employed are based on a direct modification of flow stress to include the Laplacian of equivalent shear strain and the stress tensor in the resulting three-dimensional constitutive equations is symmetric (in contrast to the “asymmetric stress” or couple-stress theory of Cosserat type advocated by Fleck/Müller/Ashby/Hutchinson, their co-workers and followers, as will be discussed in detail below). Additional aspects of the gradient approach to deformation and its implications to instability and singularity problems at nano, micro and macro scales have been discussed by Aifantis in [68,69], as well as in [70,71] where theoretical estimates for the gradient coefficients are provided, and in [72] where nonlinear issues are emphasized.

As mentioned above, a couple-stress or “asymmetric stress” strain gradient plasticity theory has been advanced recently by Fleck and co-workers [73,74]. This theory is of Cosserat type (but for plastic instead of elastic deformations) and is motivated by Ashby’s concept of geometrically necessary dislocations. Some aspects on the relation between the Fleck et al. strain gradient plasticity theory and Aifantis’ original gradient theory with symmetric stress are discussed in [71] with respect to the capability of these theories in predicting size effects in torsion and smooth profiles of strain distribution across interfaces. In this connection, a similarly motivated strain gradient theory of plasticity based on incompatible lattice deformations was recently advanced by Acharya and Bassani [75,76] with a comparison between their formulation and the original gradient theory given in [76]. Following the publication of Fleck, Müller, Ashby and Hutchinson [73] a number of articles have appeared applying their theory to plasticity problems at the micron scale (i.e. over a scale which extends from about a fraction of a micron to tens of microns) as plasticity applications at this scale are of increasing interest in electronics and MEMS. Specific applications include indentation, wire torsion and film bending, as well as debonding of ceramic particles in a metal matrix, void growth in a plastically strained solid, and crack tip plasticity. A brief review on these issues is contained in a recent report (of the US National Committee on Theoretical and Applied Mechanics) by Hutchinson [77], while more detailed considerations can be found in recent papers by Ma and Clarke [78], Smyshlyaev and Fleck [79], Hutchinson and co-workers [80-82], Shu and co-workers [83,84], Huang and co-workers [85,86], Nix and Gao [87], Stolken and Evans [88].

While such renewed interest in gradient theories can be understood in view of the remedies they provided in determining spatial characteristics of dislocation patterns (mesoscopic scales) and shear bands (macroscopic scales), actual experiments for the direct measurement of the new phenomenological coefficients, the so-called gradient coefficients, are lacking. Since gradient theories become particularly useful for small volumes, where the internal length introduced by the gradient coefficient is comparable to the characteristic dimension of the system, it follows that such experiments would be difficult to design and interpret. Nevertheless, an initial effort in this direction was reported in [68] where the gradient coefficient was determined from four-point bending tests of aluminum bars whose microstructure was engineered to gradually vary the grain size along the specimen axis. Similar work is currently being further pursued in several laboratories by realizing pure bending and torsion conditions for rods of varying diameter and detecting yielding at the outer surface of the rods. Such types of tests will not only provide the value of the gradient coefficients, but they will also bring light into related size effect issues.

In fact, the size effect issue and the possibility of gradient theory to capture this effect has been another strong reason (in addition to providing estimates for shear band widths/spacings and wavelengths of dislocation patterns) for the renewed interest in gradient theories. The already mentioned recent work of Fleck et al [73] reports observations on increased normalized torsion hardening with decreased wire

diameter from 170 μm to 12 μm . Analogous results are reported by Stolken and Evans [88] (see also Stolken [89]) who observed an increased normalized bending hardening with decreased beam thickness from 50 μm to 12 μm . Similar behavior, i.e. increasing strength with decreasing size, has also been observed in indentation tests (e.g. [90-93]; see also [78]) for the regime of 10 - 1 μm indenter size for which the corresponding hardness is approximately doubled. The same has been observed in metal matrix composites as reported, for example, recently by Lloyd [94] for the strength of an aluminum-silicon matrix reinforced by silicon carbide particles which increases significantly as the particle diameter reduces from 16 μm to 7 μm for fixed volume fraction. Such size-dependent material behavior has long been known in several scientific fields ranging from composite engineering to geomechanics (see, for example, [95-97] and references quoted therein) but the current demand of understanding novel material behavior at small scales has revived interest in the subject and imposed the need for additional experimental work. Preliminary results for modeling size effects by using gradient theory are reported by Aifantis [95] (Vardoulakis and Aifantis [96] and references quoted therein) with emphasis on single phase materials and geomaterials, as well as by Zhu, Zbib and Aifantis [97] with emphasis on metal matrix composites.

In addition to the size effect issue, another problem for which the gradient theory has provided substantial insight was the topic of understanding at the nanoscale, the structure of crack tip and dislocation cores, as well as the structure of solid-solid interfaces. Preliminary results in this direction were reported by Aifantis [68,71], while detailed considerations can be found in more recent papers by Aifantis and co-workers [98-102]. These considerations, which can eliminate classical strain singularities or discontinuities predicted by standard theories, are especially important since they can provide direct theoretical support associated with the interpretation of findings from experimental procedures recently developed (e.g. Kim [103]) for capturing the details of material configuration and deformation characteristics near crack tips, dislocation cores and interfaces.

On returning to the issue of applications of gradient theory at the macroscale, two instability problems in manufacturing technology have been considered. Both problems are concerned with shear band formation in metal forming and metal cutting respectively. In particular, forming limit diagrams (FLDs) are shown to be obtained for sheet metal forming in closer agreement with experiments when a gradient-dependent modification of Hill's anisotropic yield criterion is used. Similarly, in metal cutting, it is shown that instability analysis during "discontinuous" chip formation may provide a relation between machine tool velocity (which controls the feeding rate or process efficiency) and shear band spacing (which controls the chip size). More details on both of these problems may be found in [104, 105].

We conclude with a brief discussion of the main experimental findings and modeling efforts on novel thin film and bulk nanostructured materials. This work has been conducted by the PI and his MTU co-workers in order to detect the deformation and fracture mechanisms at the nanoscale, and evaluate the applicability of macroscopic constitutive modeling and gradient theory for interpreting the experimental observations.

Nanostructured materials are a new, exciting class of materials which have only recently been studied. They have characteristic grain sizes approximately three orders of magnitude smaller than traditional structural materials. In situ transmission electron microscopy was used to study deformation mechanisms of thin film nanostructured metals, in order to ascertain deformation mechanisms directly. It was found that deformation occurred by grain boundary sliding and grain rotation when thin films with grain sizes of 10 nm were deformed at low rates. Direct evidence of grain rotation was obtained by tracking angles between crystallographic planes in adjacent grains during straining. These experiments were conducted on gold at room temperature, and these types of deformation mechanisms would not be expected in coarser grain sized materials at such a low temperature. At higher loading rates, intergranular

fracture occurred with little plasticity. Materials with grain sizes around 100 nm deformed by traditional dislocation-based plasticity. Bulk nanostructured metals were prepared by ball milling and HIP or forging techniques; these materials deformed by intense shear banding, and behaved in a nearly perfectly-plastic manner.

Several different types of modeling were accomplished for nanostructured materials. By considering that nanostructured metals consist of two “phases”, a boundary “phase” and a bulk “phase,” it was possible to predict the effects of grain size on strength into the nanostructured regime with a rule of mixtures approach. Such a model predicted that the strength of nanophase metals should deviate from Hall-Petch behavior at approximately 20 nm, and the strength may decrease with decreasing grain size, but only at grain sizes less than 5 nm. The model is in reasonable agreement with the available data, most of which is for grain sizes 10 nm. A model for the grain size dependence and strain rate dependence of dislocation generation was formulated. The model considers image forces on dislocations which may be grown into a polycrystalline aggregate, or pulled from a grain boundary source. This simple model predicted that no dislocations should be present in the 10 nm grain size material, as was experimentally observed. However, at 100 nm grain size the image forces were not sufficient to remove all dislocations, and therefore the observed dislocation-based plasticity was predicted. A gradient elasticity model was derived for nanostructured materials, using the same “two-phase” material assumption as in the earlier strength model. The model shows promise for understanding “wavy” crack paths and crack bifurcation behavior that was observed in nanostructured metal thin film experiments. Also, two viscoplastic constitutive models were derived for nanostructured materials, based closely on the observations of grain boundary sliding and pore evolution in the thin film experiments. Finally, a pressure-dependent yield condition, a zero-extension criterion, and the gradient theory prediction of shear band thickness were adopted to model the anisotropy in tension-compression of ultra fine grain metals and their dependence of strength on the grain size.

Details on all the above issues related to thin films and bulk nanostructures can be found in Refs [106-119].

2. Fundamental Aspects

The starting point of the gradient theory is to incorporate higher-order gradients of the relevant constitutive variables into the respective evolution or constitutive equations. In the simplest case, the resulting gradient modification of dislocation dynamics, flow stress, and Hooke’s law read respectively

$$\partial \rho / \partial t = D \nabla^2 \rho + f(\rho), \quad (2.1)$$

$$\tau = \kappa(\gamma) - c \nabla^2 \gamma, \quad (2.2)$$

$$\sigma_{ij} = \lambda \varepsilon_{kk} \delta_{ij} + 2\mu \varepsilon_{ij} - c \nabla^2 (\lambda \varepsilon_{kk} \delta_{ij} + 2\mu \varepsilon_{ij}), \quad (2.3)$$

where ρ denotes the dislocation density, (τ, γ) denote effective stress and strain for plastic flow and $(\sigma_{ij}, \varepsilon_{ij})$ denote the stress and strain tensors for elastic deformation. The quantity $f(\rho)$ is the standard source term of dislocation dynamics, $\kappa(\gamma)$ is the standard homogeneous part of the flow stress and (λ, μ) are the Lamé constants. The gradient coefficients D in Eq.(2.1), c in Eq.(2.2) and c in Eq.(2.3) denote gradient phenomenological coefficients the value of which is to be determined from appropriate experiments and/or appropriate microscopic arguments depending on the prevailing deformation mechanisms and the underlying microstructure. The strain rate and temperature dependence have been suppressed in Eqs.(2.1-2.3) for convenience. Such dependence is particularly important in problems of creep and recrystallization, as well as for dynamic shear banding and strain-rate dependent materials.

The gradient-dependent expressions of Eqs.(2.1-2.3) have been used successfully to predict dislocation patterning phenomena, shear band widths and spacings, as well as to eliminate strain singularities from elastic crack tips (e.g. Aifantis [5,68]). The value of the gradient coefficients can be inferred from such dislocation pattern wavelengths and shear band widths measurements, as well as measurements pertaining to the extent of dislocation cores and the structure of crack tip opening profiles. Direct estimates for the gradient coefficients can also be obtained from properly designed experiments. For example, pure bending experiments of asymmetrically deforming beams (due to an inhomogeneous engineered microstructure - e.g. grain size distribution along the beam axis) can provide estimates of the gradient coefficient c in Eq.(2.2). Preliminary results have already been obtained and a brief outline of this possibility has been reviewed by Aifantis [68,71]. The aforementioned experimental estimates for the gradient coefficients seem to be in good agreement with theoretical estimates obtained by using self-consistent arguments as discussed, for example, by Aifantis [71] and more extensively considered by Ning and Aifantis [99]. The self-consistent estimate for the gradient coefficient c gives the expression $|c| = (\beta+h)(d^2/10)$, where β relates explicitly to the elastic constants of the material in a fashion depending on the self-consistent model used, while h is the plastic hardening modulus. The parameter d stands for the grain size.

The above discussion suggests the need for additional work on the interpretation of the gradient coefficients entering in Eqs.(2.1-2.3). For example, for the diffusion-like coefficient D , various dislocation mechanisms can be considered to obtain special expressions for it. They all lead to an expression of the form $D = \bar{\ell} \langle v \rangle$, where $\bar{\ell}$ denotes a mean free path and $\langle v \rangle$ the average dislocation velocity. Research in progress suggests that $\bar{\ell} \sim \langle \delta \tau_{\text{eff}}^2 \rangle \ell_{\text{corr}} / S^2$, where $\langle \delta \tau_{\text{eff}}^2 \rangle$ stands for the amplitude of effective stress fluctuations, ℓ_{corr} denotes the corresponding correlation length and S is the strain rate sensitivity. If a cross-slip mechanism is assumed then it turns out that $\bar{\ell} = (\bar{h}^2 / \ell_s) [1 + 2(h_0/\bar{h}) + \frac{1}{2}(h_0/\bar{h})^2] \exp(-h_0/\bar{h})$, where ℓ_s denotes an average distance between cross-slip events, h_0 denotes the distance of dislocation immobilization for dipole formation [$h_0 = \mu b / 2\pi(1-\nu)(\tau - \tau_f)$; μ is the shear modulus, b is the Burgers vector, ν is the Poisson's ratio, τ is the resolved shear stress and τ_f is the friction stress], and $\bar{h} = \int h P(h) dh$ with $P(h)$ denoting the probability for the cross-slip height to be h . A simpler expression for $\bar{\ell}$ has been proposed in the past of the form $\bar{\ell} = \Pi \gamma_c^3 / 3$, where Π denotes the cross-slip probability per unit glide area. For a polycrystalline situation with the elementary volume assumed to contain a large number of grains, it turns out that $\bar{\ell} = d \langle \tan^2 \phi \rangle / 4$ where d denotes the grain size and $\langle \tan^2 \phi \rangle$ is a numerical factor resulting from the averaging of all gliding and grain orientations. If we distinguish between mobile and immobile dislocations, write standard dislocation dynamics evolution equations for both of them (without including diffusion-like coefficients at the outset), and then adiabatically eliminate the "slow variable" of immobile dislocation density, we obtain a diffusion term in the corresponding evolution equation for the mobile dislocation density which is now of the form of Eq.(2.1) with $D = \bar{\ell} \langle v \rangle$ with $\bar{\ell} = v t_{\text{life}}$, with v being the velocity and t_{life} the mean lifetime of mobile dislocations.

Similar arguments may be employed to derive microscopic expressions for the gradient coefficient c in Eq.(2.2) and a self-consistent argument leading to an explicit relation for c in terms of the grain size and the material constants was already provided above. The self-consistent method or an improved averaging procedure may be employed to consider different than polycrystalline situations; for example, a continuous distribution of dislocations, a continuous distribution of flat cracks, a continuous distribution of spherical voids, etc. In each case a different expression for the gradient coefficient c would result depending on the geometric characteristics of the underlying microstructure and the associated internal lengths (e.g. void size and spacing). In this connection, it is pointed out that special

configurations of "geometrically necessary dislocations" have been employed recently [120] for deducing an expression for the strain gradient coefficient of the "asymmetric stress" strain gradient theory of Fleck et al [73,74]. Such static considerations are also possible for the gradient theory embodied in Eq.(2.2) and various types of gradient terms of different degree and order may result depending on the particular configurations on the dislocation arrangement assumed (e.g. Taylor lattice, tilt walls, dipolar walls, etc.). Instead of elaborating further on the above mentioned static dislocation considerations in producing strain gradient terms, we consider below a dislocation kinetics origin of Eq.(2.2).

Instead of Eq.(2.2), one may start with a standard expression $\tau = \kappa(\gamma, \alpha)$ where α is an internal variable whose evolution equation contains both a rate and a flux term (Aifantis [68,69]). For example, α may be identified with a dislocation density evolving according to Eq.(2.1). Then, in a one-dimensional setting, we may assume $\dot{\alpha} = D\alpha_{xx} + \psi(\gamma) - \phi(\gamma)\alpha$ where (ψ, ϕ) are nonlinear functions of the plastic strain γ . By considering the Fourier transform of the linearized part of this equation and "adiabatically" eliminating the fast variable α (note that for the spatial scales considered, α attains steady states much faster than γ), it turns out that α in the flow stress dependence $\tau = \kappa(\gamma, \alpha)$ is replaced by a second gradient term in γ . In fact, for a linear dependence of the form $\tau = \kappa(\gamma, \alpha) = \lambda\alpha$, the resulting equation is of the form of Eq.(2.2) with $c = \lambda\Lambda D/M^2$. If, in addition, a cross slip diffusion mechanism is assumed for the dislocation-like variable $\alpha \equiv \rho$, preliminary research gives the estimates $\lambda = (-\partial\tau/\partial\rho)$, $\Lambda \sim (\tau^{-1} \partial\tau/\partial\gamma) \langle v \rangle$, $D \sim \bar{h}^2 v / \ell$, where \bar{h} , ℓ , and $\langle v \rangle$ have been defined earlier. Typical values of the parameters involved give a value for the gradient coefficient $|c| \approx 10^{-3} \text{ N}$ which is of the same order of magnitude as those obtained from self-consistent models and size effect calibrations [71].

The final issue to be discussed here is an outline of research in progress on a more general probabilistic approach that can be employed to deduce expressions for the gradient coefficients. Thus, by assuming that the strain $\hat{\gamma}(\Gamma)$ is a random field given by a function of a random microstrain variable Γ , an expansion around the mean $\langle \Gamma \rangle$ of the form $\hat{\gamma}(\Gamma) = \hat{\gamma}(\langle \Gamma \rangle) + \hat{\gamma}_r(\Gamma - \langle \Gamma \rangle) + \frac{1}{2} \hat{\gamma}_{rr}(\Gamma - \langle \Gamma \rangle)^2$ yields the expression $\langle \hat{\gamma}(\Gamma) \rangle = \gamma - \frac{1}{2} [(\partial^2 C(r)/\partial r^2)]_{r=0}^{-1} \gamma_{xx}$ where $\gamma = \hat{\gamma}(\langle \Gamma \rangle)$, $C(r)$ denotes the spatial correlation of the microstrains. For an exponential $C(r) = \exp[-r/\lambda]$ or Gaussian $C(r) = \exp[-(r/\lambda)^2]$ correlation function, we can show that $\langle \hat{\gamma}(\Gamma) \rangle = \gamma + \alpha \lambda^2 \gamma_{xx}$ where λ is a correlation length and $\alpha = \{1/2 \text{ or } 1/4\}$ for exponential or Gaussian correlations. Then a constitutive equation of the form $\tau = \kappa[\langle \hat{\gamma}(\Gamma) \rangle]$ can lead through an appropriate Taylor expansion to the gradient expression of Eq.(2.2). The sign of the coefficient c and its relation to the internal lengths involved, depend on the type of the correlation functions and the corresponding microstructures, as well as on the deformation state (hardening or softening).

For the gradient elasticity relation of Eq.(2.3) the value of the gradient coefficient c may be deduced from the resulting wave dispersion equation as compared with a corresponding dispersion relation of lattice dynamics (see, for example, Brillouin's book on "Wave Propagation in Periodic Structures", Dover, 1946). This gives the estimate $\sqrt{c} \approx a/4$ where a denotes the lattice parameter. Other estimates for c are possible depending on the lattice or atomic chain model used and the interatomic potentials assumed.

3. Applications

3.1 Gradient Theory at the Nanoscale: Dislocation Cores / Crack Tips / Interfaces

In this section we first review recent results in progress based on the use of gradient theory to determine the extent of dislocation cores, the structure of the crack tip and the character of solid interfaces. Then we outline additional research topics that we plan to consider within the proposed program.

i) Dislocation Cores: Recently we have shown that elimination of strain singularity in dislocations is possible by including a gradient term in Hooke's law. The derived non-singular solutions can be used to estimate the extent of dislocation core and the nature of short range dislocation interactions, thus providing information which cannot be obtained by using classical elasticity theory. The results can also be used to calculate the elastic energy which is found to be finite without introducing an arbitrary cut-off radius. The special form of the gradient elasticity theory used is given by Eq.(2.3) with $\sqrt{c} \approx a/4$ where a denotes interatomic distance. The strain components for a screw dislocation are then obtained as

$$\epsilon_{xz} = \frac{b}{4\pi} \left[-\frac{y}{r^2} + \frac{y}{r\sqrt{c}} K_1\left(\frac{r}{\sqrt{c}}\right) \right] ; \epsilon_{yz} = \frac{b}{4\pi} \left[\frac{x}{r^2} - \frac{x}{r\sqrt{c}} K_1\left(\frac{r}{\sqrt{c}}\right) \right], \quad (3.1)$$

where b denotes the Burgers vector and r denotes the radial coordinate from the dislocation line. The first term in the bracket representing the singular classical elasticity solution and the second term with the Bessel function K_1 representing the gradient elasticity contribution. It is noted that $K_1(r/\sqrt{c}) \rightarrow \sqrt{c}/r$ as $r \rightarrow 0$ and, thus, the gradient term cancels the elastic singularity as the dislocation line is approached. It also follows that a dislocation core may be defined at $r \sim r_c = 1.25a$, and the strain achieves extreme values at a distance $\sim 12\%$ within this core.

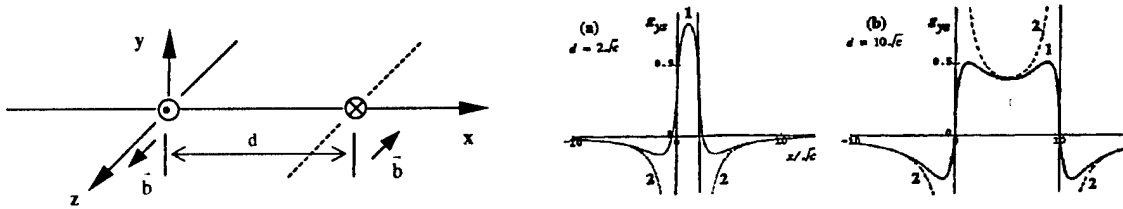


Figure 3.1: Schematics of a screw dislocation dipole with arm d and strain distribution for (a) $d=2\sqrt{c}$ and (b) $d=10\sqrt{c}$. Solid lines (1) correspond to the gradient solution and dotted lines (2) correspond to the classical elasticity solution.

The corresponding gradient elasticity total strain energy E can be calculated explicitly as ($R \gg \sqrt{c} \gg r \rightarrow 0$)

$$E = \frac{\mu b^2}{4\pi} \ln \frac{R}{2\sqrt{c}}, \quad (3.2)$$

leading to the disappearance of the cut-off radius usually assumed for the dislocation energy expression of the classical elasticity solution. Preliminary results for a dipole of screw dislocations are depicted in Fig. 3.1. They show that the strain is finite at the dislocation lines, approaching a zero value as the dipole arm

d increases to infinity (non-interacting dislocations). Moreover, the strain is finite at the central point between the two dislocations, becoming zero when the two dislocations annihilate ($d = 0$). It is interesting to observe from the sketch (b) of Figure 3.1 that the gradient and classical solutions become identical at $d = 5\sqrt{c} \approx 1.25a$, thus providing another independent estimate for the size of the dislocation core.

ii) *Crack Tips* : The above derived non-singular solutions can be used to obtain the crack opening displacement for a mode III crack by representing it with a continuous distribution of virtual dislocations. It can be shown that, in contrast to the classical elasticity prediction, the crack faces close smoothly with the strain being zero, instead of infinite, at the tip. This is shown schematically in Fig. 3.2 below

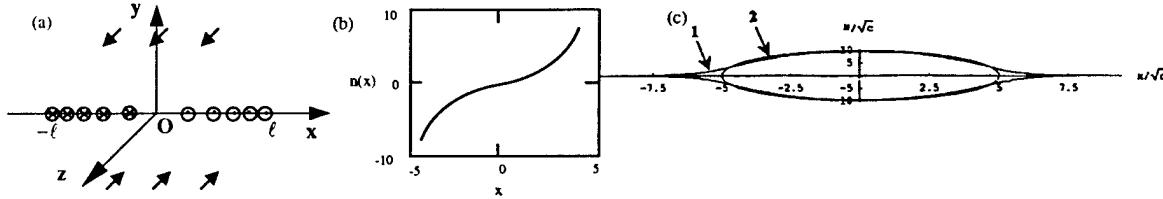


Figure 3.2: Schematics of a mode-III crack extended from $-\ell$ to ℓ [sketch (a)] and its representation by means of an array of screw dislocations with distribution $n(x) = x/\sqrt{\ell^2 - x^2}$ [sketch (b)]. Sketch (c) shows the resulting crack opening displacement and the smooth closure of the crack faces for the gradient elasticity solution (curve 1), in contrast to the parabolic profile (curve 2) of the classical elasticity solution and the associated strain singularity at the crack tip.

iii) *Interfaces* : Here we show that inclusion of the gradient term leads to a smooth transition of the strain across the bimaterial interface, in contrast to the classical theory of elasticity or plasticity giving discontinuous profiles. For the interface configuration of Figure 3.3, the corresponding strain field ϵ_{ij} , the equilibrium equation $\sigma_{ij,j} = 0$ and the gradient-dependent constitutive equation read

$$\epsilon_{ij} = \frac{1}{2} \begin{bmatrix} 0 & \gamma \\ \gamma & 0 \end{bmatrix} ; \quad \partial\tau/\partial y = 0 \rightarrow \tau = \tau^\infty ; \quad \tau = \kappa_i(\gamma) - c_i \nabla^2 \gamma, \quad (3.3)$$

here τ is the shear stress, y is the space coordinate normal to the interface and τ^∞ stands for the applied shear stress at infinity. The homogeneous part of the flow stress κ is, in general, a nonlinear function of γ and c denotes as usual gradient coefficient (the index $i = 1, 2$ designates material 1 and 2 respectively).

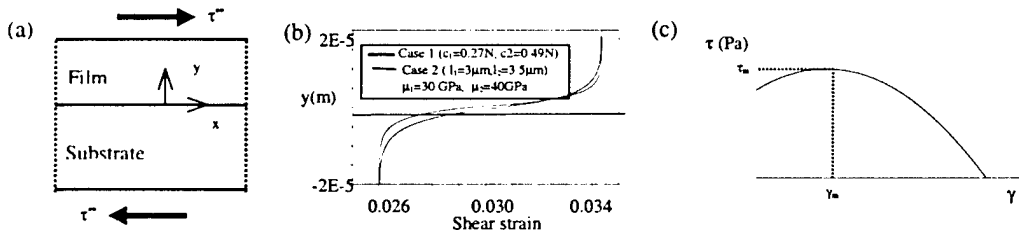


Figure 3.3: (a) Schematic of bimaterial interface, (b) strain distribution across the interface and (c) softening type of interfacial stress-strain graph for an inelastic interface.

For a linearly elastic bimaterial $\kappa_i(\gamma) = \mu_i \gamma$, where μ_1 and μ_2 denote the respective shear moduli. It then turns out that the solution for the strain distribution across the interface reads

$$\gamma = \frac{\tau^\infty}{\mu_1} \left[1 - \left(1 - \frac{\mu_1}{\mu_2} \right) e^{(-1)\gamma \sqrt{\mu_1/c_1}} \right], \quad (3.4)$$

where μ_1 denotes a “shear modulus” for the interface which is also assumed to behave elastically ($\tau_1 = \mu_1 \gamma_1$ with $\tau_1 \equiv \tau_1 = \tau_2 = \tau^\infty$ and $\gamma_1 \equiv \gamma_1 = \gamma_2$). For $\mu_1 \equiv \mu_1 \mu_2 (\sqrt{\mu_1/c_1} + \sqrt{\mu_2/c_2}) / (\mu_1 \sqrt{\mu_2/c_2} + \mu_2 \sqrt{\mu_1/c_1})$ we obtain Aifantis’ solution [71], while for $\mu_1 \equiv \mu_1 \mu_2 (\sqrt{\mu_1 c_1} + \sqrt{\mu_2 c_2}) / (\mu_1 \sqrt{\mu_2 c_2} + \mu_2 \sqrt{\mu_1 c_1})$ with $c_i = \mu_i \ell_i^2 / 2$ we obtain the solution of Fleck and Hutchinson [73a]. The first solution was obtained for the boundary conditions $\partial \gamma_1 / \partial y = \partial \gamma_2 / \partial y$ at the interface, while the second solution was obtained for the boundary conditions $\ell_1^2 \mu_1 \partial \gamma_1 / \partial y = \ell_2^2 \mu_2 \partial \gamma_2 / \partial y$. However, the problem of interest is to consider the nonlinear stress-strain behavior at the interface, as this problem relates to surface tension and crack nucleation. While the Fleck and Hutchinson theory is difficult to apply in this case, there is already a method available for considering this problem within Aifantis’ theory. In fact, for nonlinear behavior $\tau_i = \kappa(\gamma_i)$, it turns out that the strain distribution is determined by

$$y = \int_{\gamma_i}^{\gamma} \frac{d\gamma}{\sqrt{F(\gamma)}}; \quad F(\gamma) \equiv \frac{2}{c_i} \int_{\gamma_i}^{\gamma} [\kappa_i(\gamma) - \kappa_i(\gamma_i^\infty)] d\gamma, \quad (3.5)$$

where $\kappa_i(\gamma_i^\infty) = \tau^\infty$ and the values of the strain at the interface γ_i and at the two outer boundaries of the bimaterial γ_1^∞ and γ_2^∞ should satisfy the “equal area” or “Maxwell’s rule” condition $\int_{\gamma_i^\infty}^{\gamma_i} [\kappa_i(\gamma) - \tau^\infty] d\gamma = 0$, for a non-convex or softening type graph $\tau = \kappa(\gamma)$. Thus, for an inelastic interface of the form $\tau_1 = \tau_m - \alpha(\gamma_1 - \gamma_m)^2$, where τ_m denotes the maximum (taken as 10MPa) of the $\tau - \gamma$ graph depicted in sketch (c) of Fig. 3.3 and α is a numerical coefficient (taken as 0.002), the smooth transition profiles or the strain localization profiles depicted in sketches (a) and (b) of Fig. 3.4 respectively, can be obtained by utilizing the solution of Eq.(3.5) and the condition $\gamma_i < \gamma_m$ for the case (a) or the condition $\gamma_i > \gamma_m$ for the case (b).

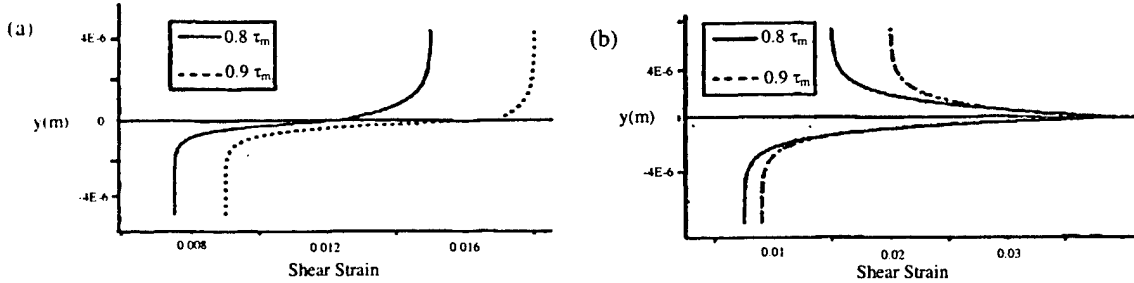


Figure 3.4: Strain distribution across the interface for (a) $\gamma_i < \gamma_m$ and (b) $\gamma_i > \gamma_m$.

These qualitative plots are given for different ratios of τ^∞/τ_m and the values $c_1 = 0.01$ N and $c_1 = 0.001$ N respectively, while the values of μ_1 and μ_2 are taken to be $\mu_1 = 30$ GPa and $\mu_2 = 40$ GPa. Results in progress for the case of a real interface between a thin film and a rigid substrate can be obtained by utilizing atomistic calculations (J.H. Rose, J. Ferrante and J.R. Smith, Phys. Rev. Lett. 47, 675-678, 1981) to motivate the expression for the “homogeneous” portion of the gradient-dependent constitutive equation for the flow stress $\kappa(\gamma)$. Research in progress suggests that the resulting expression in scaled variables $\tau^* = \tau/\tau_m e$, $\gamma^* = (\delta^{eq}/\lambda)\gamma$, is $\tau^* = \kappa(\gamma^*) = \beta^2 \gamma^* e^{-\beta \gamma^*}$, where β is a material constant, δ^{eq} is the equilibrium interface separation and λ is the range over which strong forces act. In Fig. 3.5 the scaled stress-scaled

strain (τ^* - γ^*) curve and the scaled strain distribution across the interface are depicted in sketches (a) and (b) respectively.

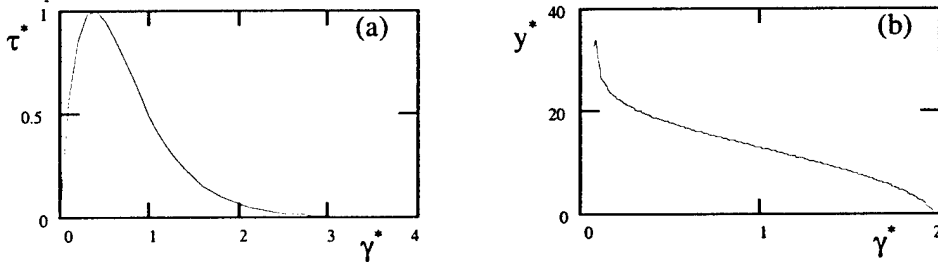


Figure 3.5: (a) Scaled stress- scaled strain curve, (b) Scaled strain distribution across the interface.

3.2 Gradient Theory at the Micro / Meso Scales: Dislocation Patterning / PSBs

In this section we first revisit (through a justification of the gradient/nonlinear terms and probabilistic arguments) the Walgraef-Aifantis (WA) reaction-diffusion model of gradient dislocation dynamics as this was first used to discuss dislocation patterning phenomena. Then a procedure is outlined for extending this model on wavelength prediction of the ladderlike dislocation structure within a persistent slip band (PSB) to consider the process of strain localization, i.e. the filling up of the specimen with multiple PSBs. The WA model that was developed to obtain the wavelength of the ladder structure of PSBs occurring in cyclic deformation distinguishes between immobile and mobile dislocations of densities ρ_i and ρ_m which are assumed to evolve according to the reaction-diffusion equations of the form [5]

$$\frac{\partial \rho_i}{\partial t} = D_i \frac{\partial^2 \rho_i}{\partial x^2} + g(\rho_i) - f(\rho_i, \rho_m) ; \quad \frac{\partial \rho_m}{\partial t} = D_m \frac{\partial^2 \rho_m}{\partial x^2} + f(\rho_i, \rho_m), \quad (3.6)$$

with (D_i , D_m) denoting the diffusion-like coefficients for the immobile and mobile dislocations, $f(\rho_i, \rho_m)$ denoting the interaction between mobile and immobile dislocations, and $g(\rho_i)$ denoting the production of immobile dislocations. The interaction term $f(\rho_i, \rho_m)$ has the form $f(\rho_i, \rho_m) = b\rho_i - \gamma\rho_m\rho_i^2$, while the production term $g(\rho_i)$ in its simplest form reads $g(\rho_i) = \alpha\rho_i^0 - \alpha\rho_i$, $-g'(\rho_i^0) = \alpha > 0$. The coefficient b , which plays the role of the bifurcation parameter of the problem and depends on the resolved shear stress, represents the freeing rate of immobile dislocations for increasing stress, while the coefficient γ represents the pinning rate of mobile dislocations by immobile dipoles. The coefficient α , which for stability purposes needs to be positive, is a constant modeling the linear creation of immobile dislocations, while ρ_i^0 is a constant denoting a reference homogeneous solution for the density of immobile dislocations.

While this initial model was the first to predict, within a nonlinear dynamic analysis, the wavelength of the ladder structure of PSBs and the transition between the various patterns of dislocation structures occurring during cyclic straining, various important issues and critical questions were not addressed satisfactorily. One such issue is concerned with the derivation of appropriate microscopic expressions for the diffusion-like coefficients D_i and D_m , and the origin of the reaction-like term $\rho_m\rho_i^2$. In fact, these three terms are necessary for discussing dislocation patterning and constitute the new

elements of the proposed WA model as contrasted, for example, to the existing Gilman-type dislocation kinetics models. Research in progress shows that a justification for the diffusion term $D_i \partial^2 \rho_i / \partial x^2$ is obtained by identifying ρ_i with the density of immobile dipoles and assuming a “dipole exchange” reaction mechanism (K. Differt and U. Essmann, Mater. Scienc. Engng. A164, 295-299, 1993). The resulting expression for D_i is $D_i \sim \rho_m \nu y_d^3 / 4$ where ν is the average dislocation velocity and y_d denotes the mean dipole height. [An expression for D_m is given in [5] on the basis of an adiabatic elimination procedure also discussed in Section 2.]

Similarly, a microscopic argument for the justification of the cubic term $\rho_m \rho_i^2$ can be provided by again identifying ρ_i with the density of the immobile dipoles and considering the coupling of the dynamics with point defect agglomerates of density ρ_0 . A kinetic equation for the evolution of the point defect agglomerates may initially be assumed of the form $\partial \rho_0 / \partial t = \alpha_0 \rho_m \rho_i - \beta_0 \rho_0 \rho_m$, with the first term denoting point defect formation by edge dipole disintegration and the second term denoting agglomerate “clean out” by moving dislocations. It may thus be assumed that a dipole stabilization occurs as a result of the competition of the process of agglomerate formation by mutual annihilation of dipole and mobile dislocation and the process of agglomerate removal by their “sweeping” by moving dislocations. By further assuming that the point defect agglomerate density ρ_0 may be adiabatically eliminating ($\partial \rho_0 / \partial t = 0$) due to the short-lifetime of these defects as compared to time-scales over which the density of dislocations (ρ_i, ρ_m) evolves, we have $\rho_0 = (\alpha_0 / \beta_0) \rho_i$, a relation which may be used directly in conjunction with the term $\rho_0 \rho_m \rho_i$ that now enters into the system of equations describing the (ρ_i, ρ_m) - dynamics, instead of the originally used term $\rho_m \rho_i^2$. This combination leads to the substitution $\rho_0 \rho_m \rho_i \rightarrow \rho_m \rho_i^2$, i.e. to the appearance again of the necessary for patterning cubic term in an indirect manner. In this connection, it is pointed out that consideration of a quadruple configuration mechanism also leads to a cubic term of the form $-(\rho_m \nu) \rho_m \rho_i^2$ or $-\dot{\gamma} \rho_m \rho_i^2$. Finally, it is noted that the dependence of the bifurcation parameter b in Eq. (3.6) on the stress τ which was not elaborated upon in the original WA model, turns out to be of an exponential form $b \sim \dot{\gamma} \exp[A\tau]$ where $\dot{\gamma}$ is the strain rate and $A = \mu b / 16\pi(1-\nu)$.

While the above arguments apply to the ladder structure of PSBs, no mechanism or theory was provided for the emergence and growth of PSBs themselves as zones of strain localization which fill gradually the specimen during the course of cyclic deformation. A phenomenological model for this problem can be developed by elaborating on the occurrence of a negative slope (unstable) regime in the cyclic stress vs. cyclic strain graph through the use of stochastic and gradient plasticity arguments to capture the evolution of the plastic strain rate in this unstable regime. Preliminary results have been reported recently (M. Zaiser, M. Avlonitis and E.C. Aifantis, Acta Materialia 46, 4143-4151, 1998) and are recast below. Specifically, the probability distribution of the local strain amplitude $\hat{\gamma}$, $P_{t_{ext}}^S(\log[\hat{\gamma}/\hat{\gamma}_0])$, which depends on the externally applied stress amplitude $\hat{\tau}_{ext}$ is given by

$$P_{t_{ext}}^S(u) = N \exp[-2V(u)/Q^2], \quad (3.7)$$

where $u = \log[\hat{\gamma}/\hat{\gamma}_0]$ with $\hat{\gamma}_0$ denoting a reference local strain amplitude, N is a normalization constant, V is a non-convex ‘potential’ associated with the ideal cyclic stress vs. local strain-amplitude graph, and Q is a measure of the fluctuation amplitude $Q \approx S_\infty^2 / 2 \hat{\tau}_{ext} S_0$ with (S_∞, S_0) denoting the asymptotic and instantaneous strain rate sensitivity]. Plots of $P_{t_{ext}}^S(\log[\hat{\gamma}/\hat{\gamma}_0])$ are shown in Fig. 3.6.

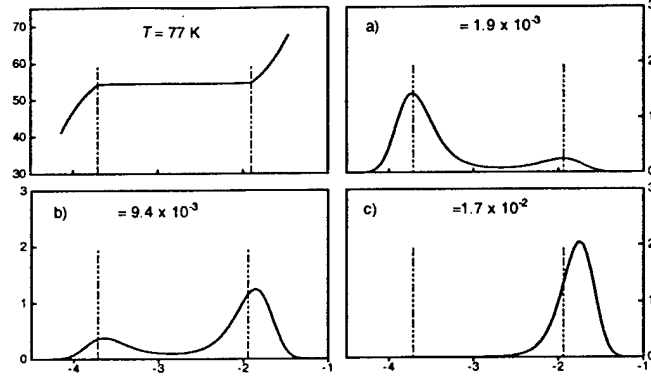


Figure 3.6: Distributions of local strain amplitudes calculated for increasing average strain amplitude. It is seen that in the course of cyclic deformation, as the average strain amplitude increases in the plateau region, the probability density for the PSBs ($\hat{\gamma}_{\text{PSB}} \approx 10^{-2}$) increases from zero to its terminal value. The opposite is true for the vein structure ($\hat{\gamma}_{\text{vein}} = 10^{-4}$).

Moreover, the following expression for the average amplitude $\{\hat{\gamma}\}(\hat{\tau}_{\text{ext}})$ as a function of $\hat{\tau}_{\text{ext}}$ holds

$$\{\hat{\gamma}\}(\hat{\tau}_{\text{ext}}) = \int P_{\hat{\tau}_{\text{ext}}}^S(\tilde{u}) \hat{\gamma}(\tilde{u}) d\tilde{u} = \hat{\gamma}_0 \int P_{\hat{\tau}_{\text{ext}}}^S(\tilde{u}) \exp[\tilde{u} \ln 10] d\tilde{u}. \quad (3.8)$$

This relation may be inverted to yield, for the case of strain-controlled deformation, the external stress amplitude $\hat{\tau}_{\text{ext}}(\hat{\gamma}_{\text{ext}})$ as a function of the imposed strain amplitude, i.e. the cyclic stress-strain curve. This determines the value of the plateau stress in the cyclic stress-strain curves in accordance with the experiment as shown in Fig. 3.7. It also turns out that a correction to Winter's rule of mixtures for the vein and the PSB structure is obtained as shown in Fig. 3.8.

To model the process of the specimen filling with PSBs in the plateau regime, we replace the homogeneous flow stress amplitude $\hat{\tau}_s(\hat{\gamma})$ with a gradient dependent expression of the form

$$\hat{\tau}_s(\hat{\gamma}) \rightarrow \hat{\tau}_s(\hat{\gamma}) - \xi^2 \hat{\tau}_s(\hat{\gamma}) [\partial^2 \log \hat{\gamma} / \partial x^2], \quad (3.9)$$

where ξ^2 is an internal length. This allows the determination of the width and spacing of the PSBs. It can be shown that periodic layers for the strain amplitude $\hat{\gamma}(x)$ with wavelength $\lambda(\hat{\tau}_{\text{ext}}, \hat{\gamma}_1)$ determined by the relation

$$\hat{\gamma}_{\text{ext}} = \frac{1}{\lambda(\hat{\tau}_{\text{ext}}, \hat{\gamma}_1)} \int_0^{\lambda(\hat{\tau}_{\text{ext}}, \hat{\gamma}_1)} \hat{\gamma}(x) dx, \quad (3.10)$$

can be derived on the basis of the above listed gradient expression for the cyclic flow stress. [The integration constant $\hat{\gamma}_1$ denotes the strain amplitude associated with the vein structure ($\hat{\gamma}_1 \approx \hat{\gamma}_{\text{vein}}$) (Fig. 3.9).

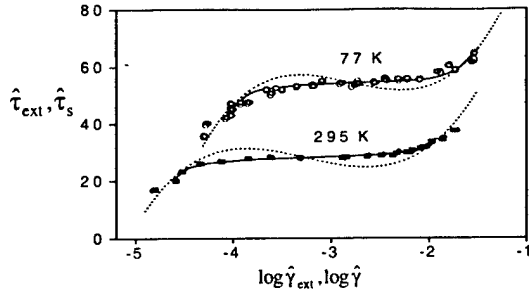


Figure 3.7: Cyclic stress-strain graphs. Dotted lines: “ideal” $\hat{\tau}_s(\hat{\gamma})$. Solid lines: calculated $\hat{\tau}_{ext}(\{\hat{\gamma}\})$ from Eq. 3.8. The open circles and solid squares are experimental data.

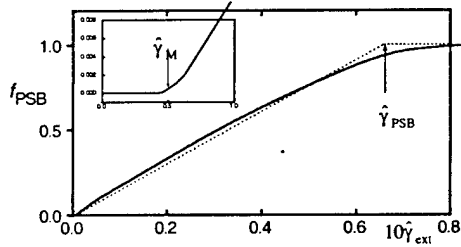


Figure 3.8: PSB volume fraction f_{PSB} as a function of $\hat{\gamma}_{ext}$. Dotted lines: Winter's rule of mixtures; Solid lines: calculated graph based on Eq. (3.7). The departure of the two curves in the $\hat{\gamma}_{PSB}$ region is confirmed by the scatter observed in experiments.

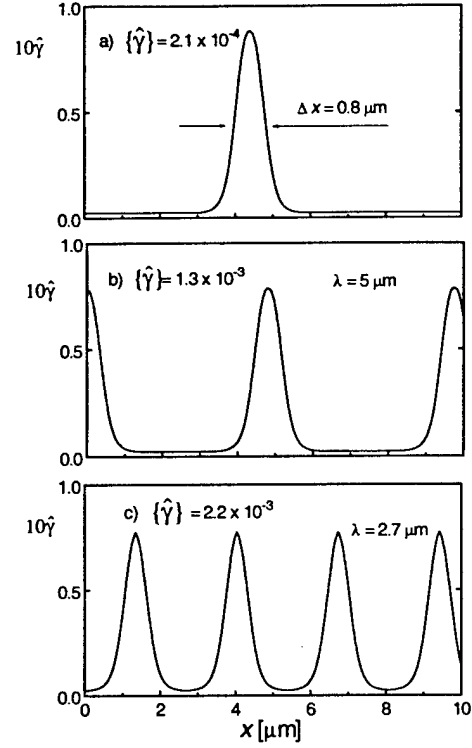


Figure 3.9: Strain amplitude patterns for increasing $\{\hat{\gamma}\}$ as predicted by Eqs. (3.8)-(3.10). It is seen that, as the strain amplitude increases, the specimen is filled-up by PSBs of approximately the same amplitude and width.

3.3 Gradient Theory at the Macroscale: Forming Limit Diagrams and Chip Formation

In this section the applicability of gradient plasticity theory in predicting spatial instability phenomena in manufacturing related processes at the macroscale is presented. Two particular problems are discussed. The first is concerned with constructing forming limit diagrams (FLDs) for sheet metals and the second is concerned with describing discontinuous chip formation during orthogonal cutting.

a) FLDs

A physical picture of localized neck formation in sheet metal forming is depicted in Figure 3.10

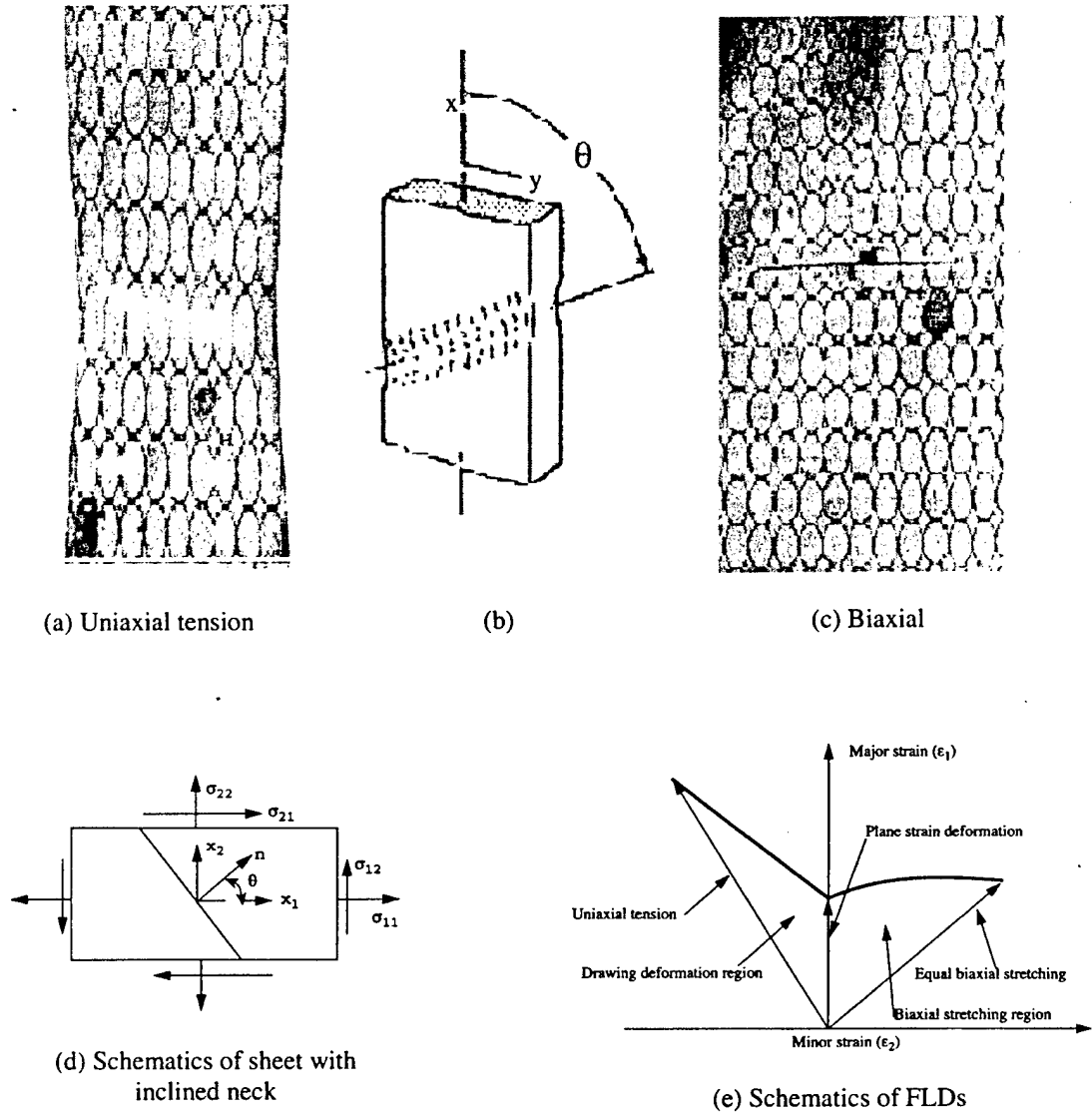


Figure 3.10: Localized neck formation in sheet metal forming (a-c).

Schematics of the sheet/inclined neck and the forming limit diagram (d,e).

A central goal is to avoid this phenomenon by operating in a safe regime of the applied strains during the forming process. This leads to defining corresponding forming limit diagrams (FLDs). For sheet metal forming processes, a vertex-type theory of plasticity (see for example Aifantis [5]) of the form

$$D_{ij} = \frac{\dot{\gamma}\tau - \gamma\dot{\tau}}{2\tau^2} \sigma'_{ij} + \frac{\gamma}{2\tau} \dot{\sigma}'_{ij} \quad (3.11)$$

may be used to describe the deformation. The quantities (D_{ij}, σ_{ij}) denote the strain rate and stress components, (τ, γ) denote, as usual, the equivalent stress and strain components, a dot denotes time differentiation, and a prime denotes deviatoric component. A gradient-dependent flow stress expression is assumed, with its rate form given by

$$\dot{\tau} = h\dot{\gamma} - c\nabla^2\dot{\gamma} \quad (3.11a)$$

with the hardening modulus h ($h = \partial \kappa(\gamma) / \partial \gamma$, $\kappa(\gamma) = k\gamma^n$) given by $h = kn\gamma^{n-1}$. For plane stress conditions ($\sigma_{33} = 0$) and proportional loading ($\beta = D_{22}/D_{11} = \text{const}$) a standard bifurcation analysis gives the following expressions for the shear band (or localized neck) angle θ_{cr} and the critical strain γ_{cr}

- $\beta < 0 \Rightarrow \theta_{cr} = \arctan \sqrt{-\beta}$, $\gamma_{cr} = \frac{2nf(\beta)}{1+\beta}$ (3.12)

- $\beta < 0 \Rightarrow \theta_{cr} = 0$, $\gamma_{cr} = \frac{2\beta^2 + n(2+\beta)^2}{(2+\beta)f(\beta)}$ (3.13)

where $f(\beta) = \sqrt{1+\beta+\beta^2}$. The above relations hold for the case $c=0$, while more complex results are obtained for the case $c \neq 0$ which, however do not affect greatly the results of localized neck orientation.

The obtained forming limit diagrams (FLDs) which correspond to the two cases $c=0$ and $c \neq 0$ are given in Figure 3.11. More details on this topic, the use of Hill's anisotropic yield criterion including gradient terms, and the effect of strain path, can be found in [104].

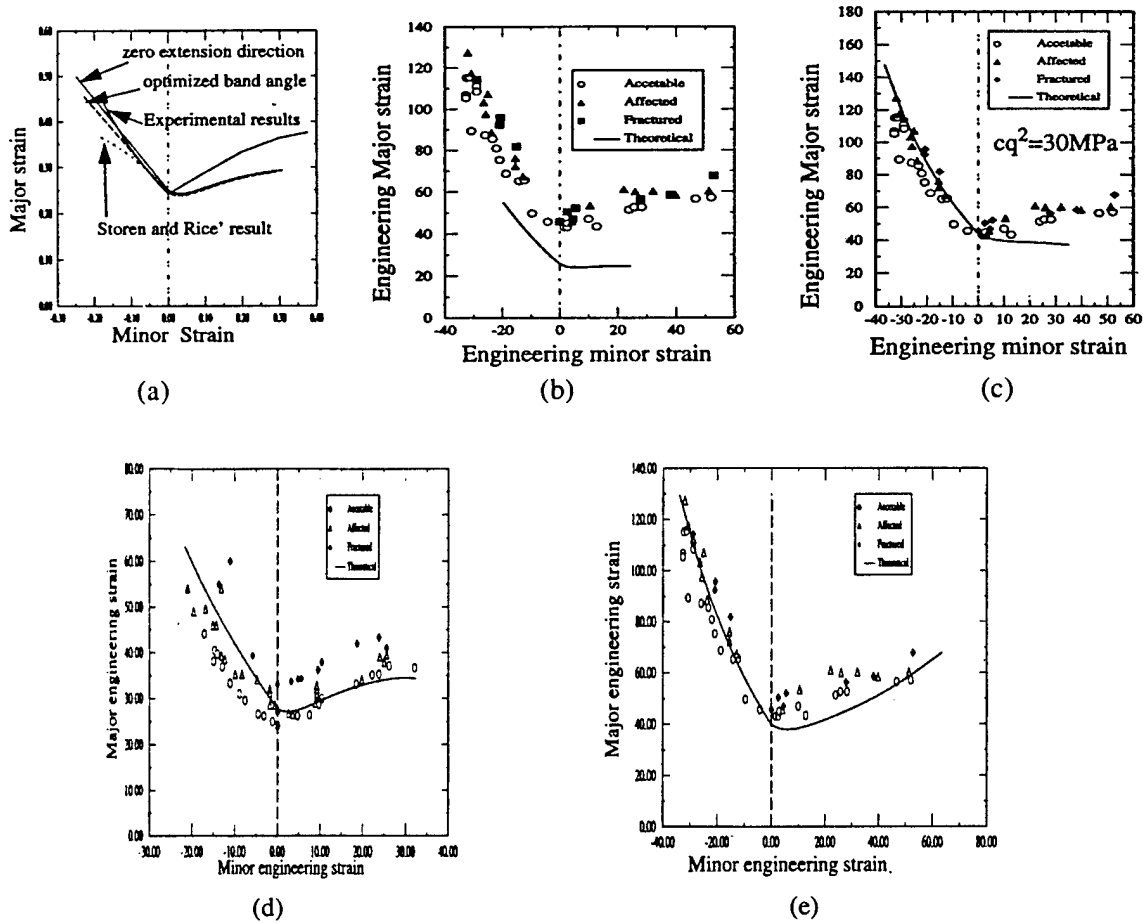


Figure 3.12: Predicted and experimental FLDs for (a) Aluminium 2036-T4, $c=0$, (b) AK-steel, $c=0$ and (c) AK-steel, $c \neq 0$, comparison of predicted and experimental results (Hecker 1975) of FLDs for (d) 2036-T4 Aluminium and (e) AK-steel using Hill's anisotropic yield criterion [104]

b) Chip Formation in Orthogonal Machining

i) A physical picture of discontinuous chip formation is given in Figure 3.13b and a schematic one in Figure 3.13a. The basic premise is to adopt a one-dimensional analysis for the shear zone region indicated in Figure 3.13b. The governing equations are

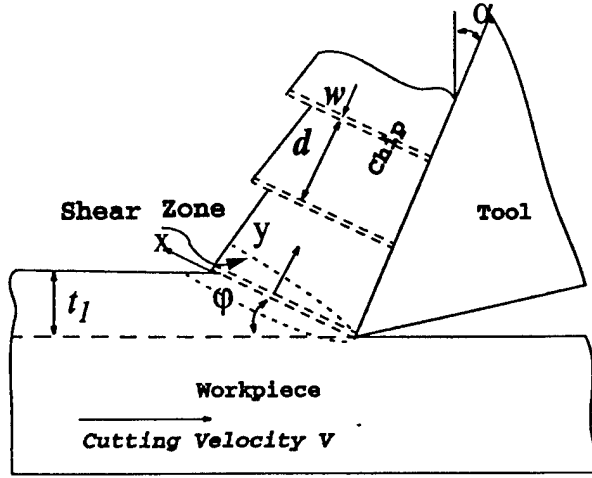


Figure 3.13a: Schematic of localized chip formation



Figure 3.13b: Localized (discontinuous) chip

$$\begin{aligned}
 \frac{\partial \tau}{\partial y} &= \rho \left(\frac{\partial v}{\partial t} + V_n \frac{\partial v}{\partial y} \right) \\
 \dot{\gamma} &= \frac{\partial v}{\partial y} = \frac{1}{G} \left(\frac{\partial \tau}{\partial t} + V_n \frac{\partial \tau}{\partial y} \right) + \dot{\gamma}^p \\
 \rho c_v \left(\frac{\partial \theta}{\partial t} + V_n \frac{\partial \theta}{\partial y} \right) &= \beta \tau \dot{\gamma}^p + k \frac{\partial^2 \theta}{\partial y^2} \\
 \tau &= \kappa(\dot{\gamma}^p, \dot{\gamma}^p, \theta) - c \frac{\partial^2 \dot{\gamma}^p}{\partial y^2}
 \end{aligned} \tag{3.14}$$

where the various symbols are as follows: The quantities (τ, γ) denote shear stress and strain, v is the material velocity in the shear direction and V_n is the feed (cutting) velocity normal to this direction, ρ is the density, G denotes shear modulus, $\dot{\gamma}^p$ denotes the plastic strain rate, c_v is the specific heat, β is the Taylor-Quinney non-dimensional coefficient that measures the fraction of plastic work converted into heat, k is the heat conductivity, θ is the temperature and c is the gradient coefficient. On neglecting elasticity ($G \rightarrow \infty$) and V_n ($V_n \ll v$), we can perform a linear instability analysis. Such an analysis illustrating the use of gradient plasticity to predict the shear band structure (and therefore the chip size) depicted in the figures is contained in [121] and more details can be found in [105]. Below we list only a summary of the main results as follows:

- Critical localization condition: $H = -\left(c + \frac{ks}{\rho c_v}\right)q^2$; where H is the strain hardening coefficient,

$$H = \frac{d\tau}{d\gamma} \Big|_{\dot{\gamma}}, s \text{ is the strain rate sensitivity, } s = \frac{\partial \tau}{\partial \dot{\gamma}} > 0 \text{ and } q \text{ is the wave number of the perturbation}$$

- Internal Length Scale : $\ell = \sqrt{-\frac{1}{H}\left(c + \frac{ks}{\rho c_v}\right)}$, Shear Band Width w : $w \propto \ell$

- Characteristic time for the formation of shear localization t_c : $t_c \equiv \frac{1}{\omega_p} \geq -\frac{k + c_v s}{c_v H} \equiv -\frac{s}{H} = -\frac{m\tau}{H\dot{\gamma}} = \tilde{t}_c$

where m is the strain rate sensitivity, $m = \frac{\partial \ln \tau}{\partial \ln \dot{\gamma}}$ and ω is the growth rate of the perturbation It

follows that the shear band spacing $d \equiv V_c t_c$ can be estimated from the relation $d = \chi_1 \frac{mf \sin \phi}{\lambda \cos \alpha}$ where χ_1 denotes a material constant with $\chi_1 > 1$, f is the feed rate and λ is shear localization

parameter defined as $\lambda = -\frac{H}{\tau} = -\left[\mu + \left(\frac{1}{\tau} \frac{d\theta}{d\gamma}\right)\Phi\right]$, with Φ being the thermal softening parameter

given by $\Phi = \frac{\partial \tau}{\partial \theta} < 0$ and $\mu = \frac{1}{\tau} \frac{d\tau}{d\gamma}$ being the normalized strain hardening coefficient. It can further

be shown [105,121] that the flow localization parameter is expressed in terms of the material properties and cutting conditions as

$$\lambda = -\left[\frac{n}{\dot{\gamma}} + \frac{\beta\Phi}{\rho c_v (n+1) \left(1 + 1.328 \sqrt{\frac{k\dot{\gamma}}{Vf}}\right)} \left(n+1 - \frac{0.664 \sqrt{\frac{k\dot{\gamma}}{Vf}}}{1 + 1.328 \sqrt{\frac{k\dot{\gamma}}{Vf}}} \right) \right] \quad (3.15)$$

Figure 3.14 shows the effects of feed rate on the shear band spacing for AISI-304 steel and Ti-6Al-4V at different cutting velocities. It is found that the predicted shear band spacing is in agreement with the experiments [122].

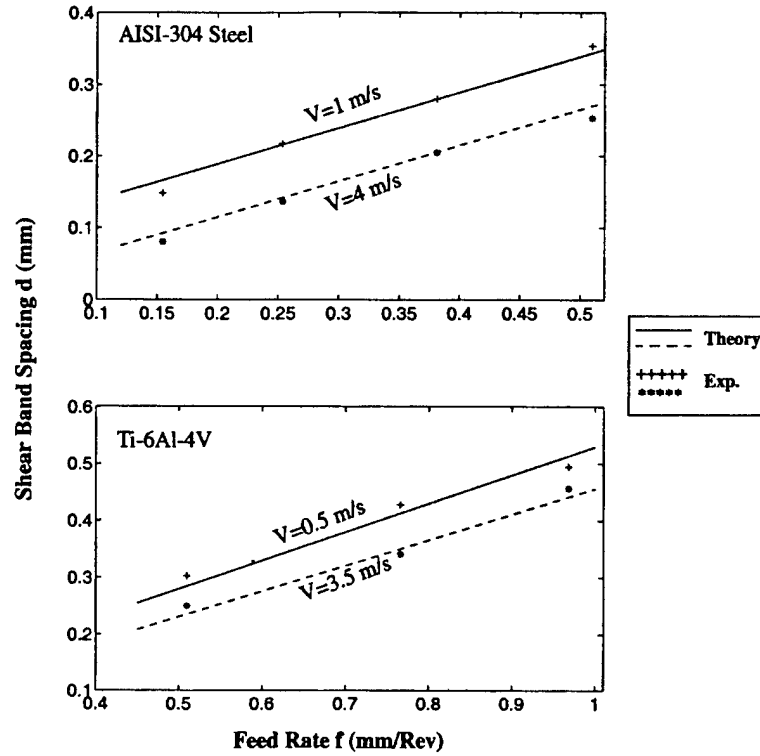


Figure 3.14: The effect of cutting conditions on the shear band spacing

A more elaborate relative perturbation analysis [105] can lead to the following threshold wavelength prediction

$$\ell_{th} = \sqrt{-\frac{m}{v} \left(\frac{k\Theta}{\tau_o \dot{\gamma}} + \frac{\rho c_v \Theta}{m \tau_o^2} \right)} \quad (3.16)$$

below which the initial perturbation will not grow. This may be viewed as a lower bound of the shear band width and can be readily evaluated for a cutting process where the rake angle, the cutting velocity and the feed rate are given. A stability condition for chip formation can then be postulated by the relation $\ell_{th} \geq \delta$, where δ is the size of shear zone. Moreover, based on the experimental observations, an instability criterion for chip formation can be established as $\frac{\ell_{th}}{\delta} \leq \Gamma^*$, where Γ^* is determined by experiments.

4. Size Effects: Gradient Theory Interpretation

In this section we first review recent and results in progress on the interpretation of size effects in torsion and bending of solid bars by using a gradient modification of the strength of materials approach. This modification amounts into employing a gradient-dependent flow stress of the type (which is a slight generalization of Eq.(2.2) with m denoting a material constant)

$$\tau = \kappa(\gamma) - c_1 (\nabla \gamma \cdot \nabla \gamma)^{m/2} - c_2 \nabla^2 \gamma. \quad (4.1)$$

The rest of the arguments (i.e., strain distribution, definitions of equivalent stress and strain, Hooke's law for the elastic strains and moment vs. stress distribution relation) are the same as in the standard mechanics of materials approach. Then, on the basis of Eq.(4.1) with $\kappa(\gamma) = \sigma_0$ and an assumed elastic-perfectly plastic behavior, it turns out that an explicit expression for the dependence of the yield strength Y at the outer surface of the bar on the size (radius α or height h) of its cross-section is obtained as follows

$$Y(\alpha) = \tau_0 \left(\frac{\alpha^2}{\alpha^2 + (c_2/G) + (c_1/G)\alpha} \right), \quad Y(h) = \sigma_0 \left(\frac{h/2}{(h/2) + (\bar{c}_1/E)} \right), \quad (4.2)$$

for torsion and bending respectively. Fig.4.1(a,b) shows the fitting of experimental results obtained for the size dependence of the yield stress Y on the radius α of cylindrical bars subjected to torsion (J.L.M. Morrison, Proc. of the Inst. of Mech. Eng. 142, 193-223, 1939) and on the height h of rectangular beams subjected to bending (C.W. Richards, Proc. Am. Soc. Testing Mats. 58, 955-970, 1958). Similarly, for the recent experiments on increased torsional hardening with decreased wire diameter reported by Fleck et al. [73], Eq.(4.1) with $\kappa(\gamma) = \tau_0 + k\gamma^n$ and an assumed fully plastic behavior we obtain the following size-dependent torque (M) vs. surface shear strain (γ_s) which is graphically shown in Fig. 4.1(c)

$$\frac{M}{\alpha^3} = 2\pi \left(\frac{\tau_0}{3} + k \frac{\gamma_s^n}{n+3} - c_1 \frac{\gamma_s}{3\alpha} - c_2 \frac{\gamma_s}{2\alpha^2} \right) \quad (4.3)$$

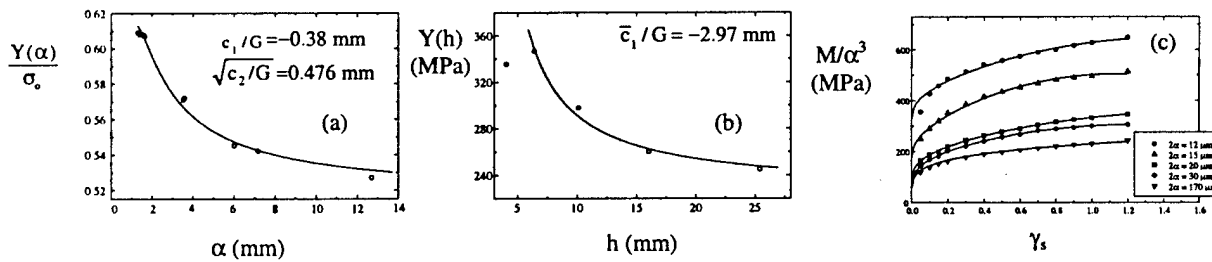


Figure 4.1: Quantitative comparison between theory and experiment: (a) yielding behavior in torsion, (b) yielding behavior in pure bending and (c) hardening behavior in torsion ($-c_1 = 538.2-1088.1$ N/m and $10^3 c_2 = 1.35-6.76$ N).

Similarly, reference is made to a recently published article by Stolken and Evans [88] where the "asymmetric stress" strain gradient plasticity model of Fleck and Hutchinson is used to interpret the observed size effect in bending of thin foils. This problem can also be discussed by using "symmetric stress" strain gradient models. In fact, by employing a gradient dependent strain energy density formulation which allows a direct comparison of the aforementioned two approaches, one may consider the form $w = w(\epsilon) + c_1 |\nabla \epsilon| + c_2 |\nabla \epsilon|^2$; $w(\epsilon) = \epsilon [3E_p \epsilon + 4\sqrt{3}\Sigma_0]/8$ is the homogeneous part of the strain

energy density with $\epsilon = (2/\sqrt{3})\kappa|y|$ denoting the equivalent strain and (c_1, c_2) being gradient coefficients. The assumed expression for the homogeneous part of the strain energy density is the same as in Stolken and Evans [88] with E_p denoting plastic modulus (hardening coefficient) and Σ_0 effective yield strength. Finally, by using the relation $M = dW/d\kappa$ ($W = \int_A w dA$) for the applied moment, we can obtain a moment (M) vs. surface strain (ϵ_s) relation depicted with solid lines in Fig.4.2(a). The dotted lines correspond to the prediction of the Fleck-Hutchinson theory employed by Stolken and Evans [88] for a value of their internal length $l_c = 6.2 \mu\text{m}$. [There is a departure of this prediction from the one reported in the aforementioned article of Stolken and Evans due to an error in their procedure when rescaling the moment and computing the corresponding theoretical values. The internal lengths l_1 and l_2 appearing in Fig.4.2 (a) are defined by $l_1 = c_1/\Sigma_0$ and $l_2 = \sqrt{c_2/E_p}$.

A more rigorous (as contrasted to the above described mechanics of materials approach) boundary value problem approach implemented by FE analysis has been used by Zhu, Zbib and Aifantis [97] for interpreting size effects in metal matrix composites. It was found that the strength of metal matrix composites decreases with increasing particle size of reinforcement under constant volume fraction for all three materials studied: Al-Si-Mg, Al-Al₂O₃, and Al-TiB₂. The results of the gradient theory were in agreement with both existing experimental data and available microscopic dislocation models for these materials, as shown in Fig.4.2(b). The solutions are cumbersome and were evaluated numerically by employing a gradient plasticity model based on Eq.(2.2).

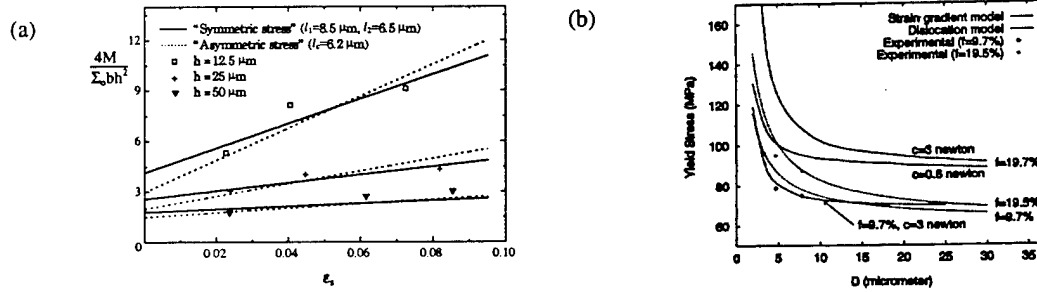


Figure 4.2: (a) Fitting of Stolken and Evans [88] thin foil bending experimental results with the “symmetric stress” and “asymmetric stress” strain gradient models. (b) Calculated yield stress (0.2% offset) vs. particle size for an Al-Si-Mg metal matrix composite, showing gradient plasticity solutions for different gradient coefficients c , and for a dislocation-based model. The values of f indicate particle volume fraction. From Zhu, Zbib and Aifantis [97].

In concluding this section on size effects, reference is made to an open problem of increasing current interest: namely, the determination of hardness and related mechanical properties from indentation tests where the size of the indenter varies from the micrometer to the nanometer regime. A deeper understanding of the mechanics and physics associated with the contact and penetration phenomena in such small volumes is important from both the scientific and technological points of view, with implications ranging from device miniaturization and computer disk drive manufacturing to magnetic recording and tribological effects on piston wear. Quite remarkable phenomena, including discontinuous yielding and size-dependent hardness, have been recorded recently in such small-volume regimes. Size effects, in particular, have been observed as the indenter diameter D is reduced from $20 \mu\text{m}$ to about $2 \mu\text{m}$. The gradient dependent form of the flow stress given in Eq.(4.2) can be utilized, in principle, to provide an explanation for the dependence of hardness on the size of the indenter. By noting that H is proportional to the stress σ ($H \sim 3\sigma$; Tabor’s relation), we have

$$H = H_0 - c_1 |\nabla \gamma| - c_2 \nabla^2 \gamma, \quad (4.4)$$

where m is again taken to be equal to 1 and H_0 is the hardness in the absence of gradient effects. By approximating γ with an average value equal to $2h/D$ (where h is the indenter's depth and D is the equivalent indenter's diameter) and using the rough estimates $\nabla\gamma \sim 2\gamma/D$, $\nabla^2\gamma \sim 4\gamma/D^2$, we can obtain from Eq.(4.4) a plot of H vs. D where the values of the gradient coefficients c_1 and c_2 are adjusted to fit the experimental data of Nix and Gao [87]. The results are shown in Fig.4.3 with the parameters (H_0 , c_1 , c_2) taking the values (0.595 GPa, -2500 N/m, $0.414 \cdot 10^{-3}$ N) for Fig.4.3(a) and (0.37 GPa, -853 N/m, $0.164 \cdot 10^{-3}$ N) for Fig.4.3(b).

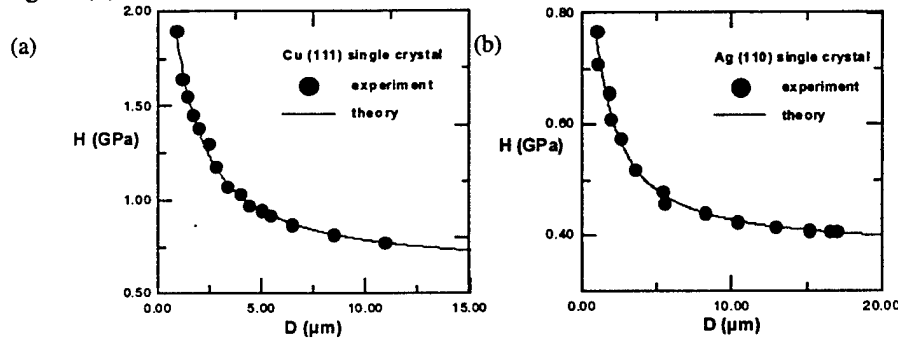


Figure 4.3: Fitting the experimental results of size-dependent hardness H vs. D according to the gradient-dependent constitutive Eq.(4.4) for (a) Cu (111) and (b) Ag (110) single crystals.

5. Nanomechanics: Experiments and Modeling

The results listed in this section are concerned with experimental and modeling studies of nanostructured materials, which is an emerging class of materials exhibiting very fine structural scales and a great deal of promise. Experiments were conducted on thin film and bulk nanostructures, and Sections 5.2 and 5.3 in this report deal with these subjects. Modeling of the mechanical and constitutive behavior of nanostructures was also accomplished, and is reported in Section 5.4.

5.1 Physical Aspects of Nanostructured Materials

Nanostructured materials are a unique class of materials having ultra fine grain sizes, typically 2-5 orders of magnitude smaller than conventional materials. For example, a typical steel has a grain size of $10\mu\text{m}$ ($10 \times 10^{-6}\text{m}$), while nanostructured materials have grain sizes below 100nm ($100 \times 10^{-9}\text{m}$). These materials have been studied in detail only recently, since about the mid-1980's, when techniques were developed to synthesize ultra-fine, single crystalline powders. Nanostructured materials have created a great deal of interest, due to the potential of improved properties in comparison to conventional structural materials. High-toughness ceramic and intermetallic materials have been developed, along with very high strength metal alloys. Processing is improved due to improved diffusion in the nanostructured material. Increased fracture strength has been obtained in brittle materials. Physical properties, such as density and thermal conductivity, are vastly different in nanostructured materials, and both metastable phases and increased solid solubility have been reported. Several reviews of processing and properties of nanostructured materials are available [123,124]. These reviews and the references quoted therein should be consulted for further information about basic materials issues.

Since the science of nanostructured materials is in its infancy, many aspects of material structure and structure/property relations are not known. Of particular interest here are the deformation behavior of nanostructured materials, and the associated constitutive behavior. As already mentioned, a material may be considered to be “nanostructured” if the grain size is on the order of 100 nm or less, while typical engineering metals have grain sizes between 5 and 100 μm . Figure 5.1 shows a physical model of a nanostructured material. Two types of atoms are present, one representing “boundary” atoms and one representing “bulk” atoms. The same two species are present in conventional materials, but only as the grain size approaches 10 nm does the fraction of “boundary” atoms become appreciable. In this range, depending on the assumed thickness of the “boundary” region, simple geometrical calculations show that the fraction of “boundary” atoms will approach that of the “bulk” atoms. Since the boundaries are more open and disordered, the material may be viewed as consisting of two “phases.”

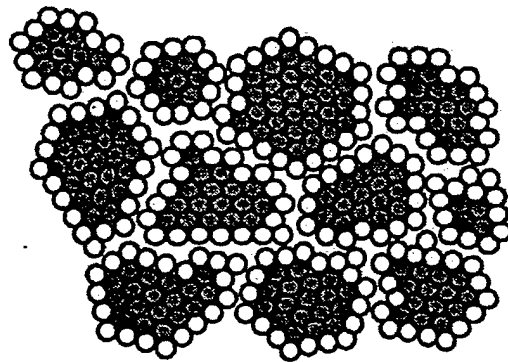


Figure 5.1: Schematic depiction of a nanostructured material, showing atoms which may be considered to be in grain interiors (grey) and atoms which may be considered to be in grain boundaries (white).

The relevant deformation and fracture mechanisms at the nanoscale have not been sufficiently studied, and they are not well understood. For example, while in traditional metals and alloys the strength increases and the ductility decreases as the grain size gets smaller, at grain sizes of 10 - 20 nm some studies have proposed that a “reverse phenomenon” of decrease in strength with decreasing grain size occurs [125]. More recent studies have cast doubt on this early result [126], but the difficulties associated with producing clean, reproducible nanostructured materials in bulk have made experimental studies very difficult and mechanical property measurements suspect. Moreover, as the grain size approaches 10 nm, the classical deformation mechanisms such as the operation of Frank-Read dislocation sources and the formation of dislocation pileups and cell walls become increasingly difficult and irrelevant (dislocation core size is comparable to the grain size). Most of the speculation for the pertinent deformation mechanisms has centered around the increase in interfacial area and grain boundary triple junction density leading to enhanced room temperature boundary sliding or creep, and triple junction and nanopore migration leading to irreversible plastic deformation. However, the effects of nanopore density and morphology are not known and a relevant issue is whether current theories of monolithic or composite material behavior may be extrapolated to systems where grain or reinforcement size and spacing approach the range of 10 nm or less.

5.2. Experimental Studies on Nanostructured Metal Thin Films

Since the deformation behavior of nanostructured materials is not known, experiments were conducted to determine these mechanisms and aid in constitutive modeling. A convenient means of studying deformation in nanostructures is to deform thin films *in situ*, inside a transmission electron microscope. In traditional grain size metals, care must be exercised when applying the results of such studies to bulk materials, because the film thickness is significantly smaller than the grain size. In nanostructured metal films, this is less of a concern, because the film thickness is the same magnitude or greater than the grain size. Deformation mechanisms may be observed directly, at high resolution, in an atomic resolution microscope fitted with a straining stage. The experimental studies accomplished direct observation of deformation in nanocrystalline metals and composites, with grain sizes down to 8 nm.

The geometry of the thin film experiments is shown in Figure 5.2. A substrate, which is aluminum, a polymer, or carbon, is coated with a nanocrystalline gold layer [108-109]. If the substrate is the polymer or aluminum, it deforms in a controlled, ductile fashion, as shown in the figure. If the substrate is carbon, the substrate is brittle and much thinner, and it tends to crack and fail at a high rate. In either case, the deformation in the coating can be viewed directly after the loading has been interrupted. By loading in steps, the sequence of deformation can be ascertained with very high resolution. The observer is looking down from the top of the film.

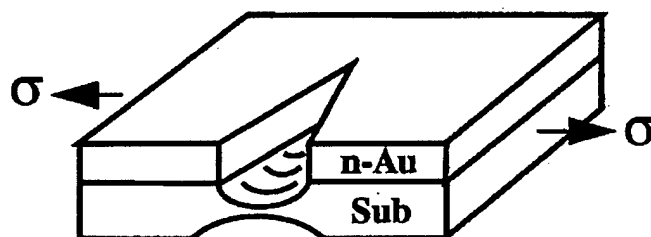


Figure 5.2 Schematic diagram illustrating the geometry of the *in situ* deformation and fracture experiment. A nanostructured gold coating (n-Au) on an aluminum, polymer, or graphite substrate is deformed and observed in the transmission electron microscope.

Such studies have been conducted with nanostructural gold coatings (to observe the deformation characteristics of the nanophase material), and also with brittle silica coatings (to observe the deformation and fracture of the aluminum substrate at high strains.) The major new findings of these studies, related to deformation of nanostructured gold films, may be summarized as follows: i) Nanostructured films deform in a ductile manner, at grain sizes down to at least 8 nm; ii) Plastic deformation occurs in the finest grained samples (8-25 nm) without dislocation activity; iii) Nanopores which are present in grain boundary triple junctions grow during deformation, by an apparently diffusive nature, even at room temperature. This is a very low temperature for gold, and large scale diffusion would not be expected in traditional grain size regimes; iv) Direct evidence of grain rotation and presumably grain boundary sliding during deformation of these films has been observed. Again, grain boundary sliding would not be expected in traditional gold until a much higher temperature; v) Nanostructured gold coatings strained at high rates (on a carbon substrate) exhibit undulated fracture surfaces with a wavelength much larger than the grain size. Details of these experimental results are presented in References [108,109,111]. Key features are presented below.

(i) *General Features of Deformation and Fracture - Nanostructured Gold [108]*

Figure 5.3 shows a typical microstructure during deformation of a gold film with an average grain size of 8 nm. In this case the gold film was deposited on top of aluminum, and similar results were obtained when the gold was deposited on a thin polymer substrate (which would have little effect on the deformation characteristics of the gold coating.) In the micrograph, the observer is looking down, perpendicular to the film which is being strained in the plane of the paper.

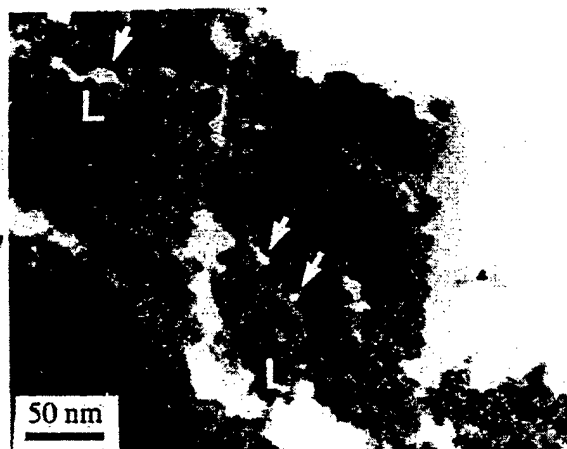


Figure 5.3 TEM micrograph showing extensive plasticity, ligament formation, and crack growth by void coalescence and link-up in nanocrystalline gold (8 nm grain diameter) on Al substrate.

Several important observations may be elucidated. First, *the nanocrystalline gold deformed in a very ductile manner*. This is clearly observable by examining the mating gold crack faces in the secondary cracking region; the material adjacent to the crack faces has deformed extensively, and the crack faces do not “mesh” as they would in the case of brittle fracture. Additionally, one may observe ductile ligaments which are bridging the secondary cracks (indicated by “L’s” in the figure). These ligaments are necking and deforming permanently as the crack tip opening displacement increases. Figure 5.3 also shows evidence of crack growth by microvoid coalescence and link-up. These “nanopores” are indicated by arrows, and appear to be growing along the grain boundaries. This leads to a grain boundary “grooving” effect which can be clearly observed in the nanopores in the figure. [For example, the pore above the uppermost “L” is not symmetric; it is semicircular on top, but a grain boundary groove has formed on the bottom.] It is difficult to imagine this type of void growth and grain boundary grooving occurring without the aid of extensive diffusion, even though the homologous temperature is very low. The cracks observed in Figure 5.3 grew along the grain boundaries, apparently due to the growth and link-up of grain boundary voids.

This growth of grain boundary nanopores has been directly observed in atomic resolution microscopy. Figure 5.4 shows a sequence of micrographs taken during crack growth in a nanostructural gold film. Ahead of the crack tip, a nanopore nucleated, Figure 5.4(a). Under further loading, the pore grew until only a ligament separated the pore from the crack, Figure 5.4(b). The ligament connected two different grains and narrowed until it pinched off at the grain boundary. After pinching off, the ligament rapidly disappeared to produce a grain surface of uniform curvature, Figure 5.4(c).

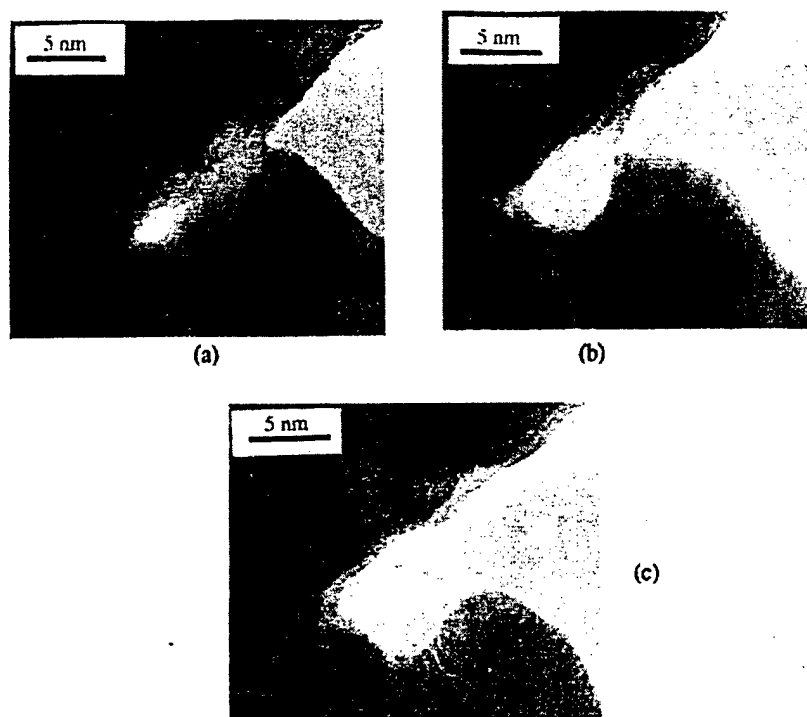


Figure 5.4 Lattice-image micrographs of *in situ* crack propagation in 8 nm grain diameter gold on a thin carbon substrate. (a) Intergranular crack propagation and nanopore formation in the grain boundaries ahead of the crack tip. (b) Crack growth and ligament formation. (c) Diffusion-based elimination of the ligament.

The shape changes just described occurred without any apparent dislocation activity within the ligament. The smoothing of the ligament after pinching off at the grain boundary is certainly a diffusive process, and it is proposed here that the thinning of the ligament itself is caused by mass diffusion. A natural question which arises is whether this ligament formation and diffusion-based deformation is a thin-film effect or an artifact of the TEM environment. Although surface diffusion may be a factor, temperature probably is not, as previous investigators have determined that beam-heating of thin foils is limited to about 100°C. Furthermore, *in situ* straining experiments on coarse-grained materials [127] have resulted in ligament formation during ductile fracture, but this ligament formation was always associated with dislocation activity. Therefore, the observations of diffusion-based deformation in these nanometer grain size thin films cannot be ascribed to thin film effects alone; the grain size and atomic structure must be significant factors.

A final observation concerning fracture regards periodic instabilities observed in 25 nm grain size gold films on carbon substrates. Figure 5.5 shows that the crack path became undulated, in an almost sinusoidal shape, after which crack bifurcation occurred. The wavelength of the crack undulation is significantly larger than the grain size.

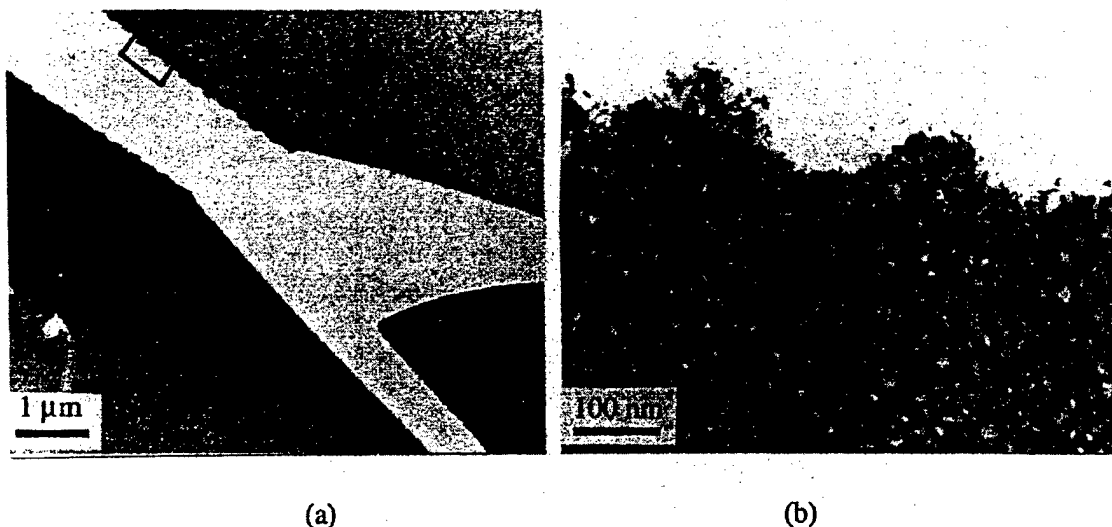


Figure 5.5 Plastic deformation and fracture of 25 nm grain diameter gold film on carbon. (a) TEM micrograph showing periodicity before crack bifurcation. (b) Higher magnification TEM micrograph showing periodicity of crack path and plastic thinning along crack face.

(ii) The Mechanisms of Plasticity in Smaller (<10 nm) Grain Size Nanostructures [111]

As noted above, there was no experimental indication of dislocation activity within individual grains. That is, no dislocation images were observed within the grains after straining, and no contrast changes associated with moving dislocations were observed on videotape during in situ straining. This suggests that the ductile behavior was due to grain boundary processes such as grain boundary sliding.

The deformation behavior was studied in the thin films, in the region ahead of a growing crack tip. The $\{111\}$ and $\{200\}$ lattice fringe images are easily observed for properly-oriented grains. These fringes lie parallel to the trace of the respective crystal planes. Because of the small scattering angle for electron diffraction, fringe images are expected to be observed only for those crystal planes with normals approximately perpendicular to the incident beam direction. Thus, a misorientation angle is specified in the image plane (corresponding closely with the film plane) for two nanocrystals with observable lattice fringes. A change in the misorientation between two grains by rotation is then observable by a change in the angle between the lattice fringes. This technique works very well, as long as the axis of rotation is nearly parallel to the electron beam and film normal; otherwise, the lattice fringes will go out of contrast as the diffracting planes are rotated away from the beam. It has been our experience that during deformation, lattice fringe contrast may change in some grains but not others, and that the loss of lattice fringe contrast in a given grain may be transient.

An example is shown in Figure 5.6, in which a crack is growing from left to right in the micrograph and lattice fringes are imaged in most grains. The angles between the lattice fringes among several grains (labelled with letters in Figure 5.6) were measured at successive straining stage displacements. The grain misorientation angle between most of these grains was altered during deformation, indicating that the grains underwent a relative rotation with respect to each other. The relative rotation of the of the lattice fringes from two typical grains is shown in Figure 5.7.



Figure 5.6: High resolution lattice image of grains ahead of a crack tip, growing from left to right in the top half of the photo. 8 μm macroscopic displacement.

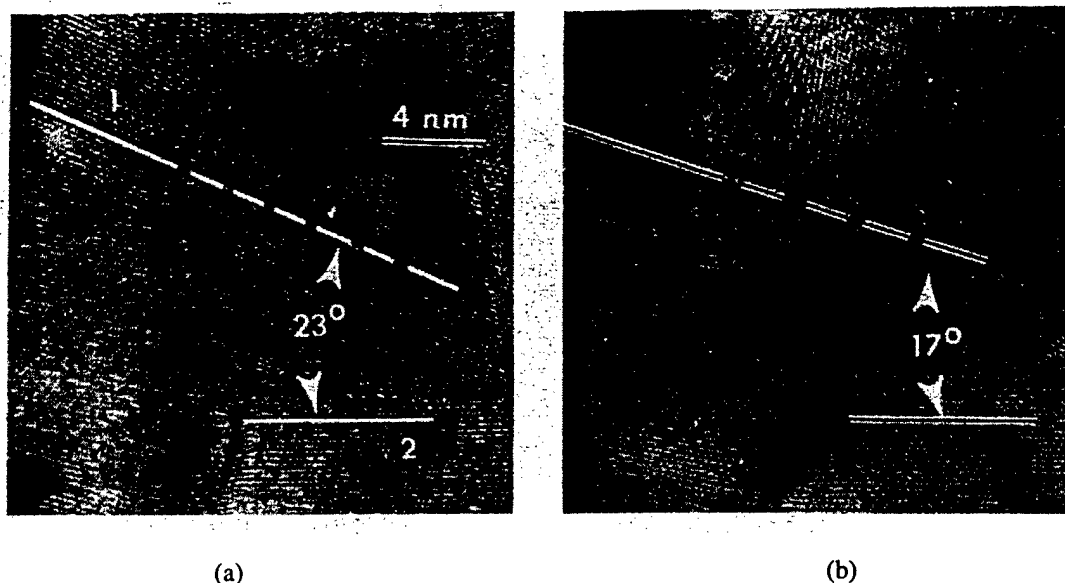


Figure 5.7: High resolution lattice images in the same area as Figure 6, showing a 6 degree change in the angle between lattice fringes of neighboring grains during straining. The grains being measured are labelled 1 and 2. (a) Before straining. (b) After 25 μm macroscopic displacement.

The rotations observed for representative grains are given in Table I and plotted in Figure 5.8(a). The sign convention is as follows: the lattice fringes in Grain I define a material reference axis, and a counter-clockwise rotation of any grain with respect to the fringes in Grain I is arbitrarily defined as a positive rotation. Several interesting conclusions may be drawn from this data. First, significant relative rotations occurred; Grains F and I, which are separated by only one grain, rotated 15 degrees with respect to each other. Second, the rotation was inhomogeneous; for example, adjacent Grains C and D did not rotate at all, while adjacent Grains D and F rotated by 7 degrees. Finally, the measurements are self-consistent within approximately 2 degrees; that is, the rotations of pairs CI and DI are equal, and the sum of the rotations of pairs DF + DI are within 2 degrees of the rotation of pair FI, as is required by geometry.

Table 5.1: Relative rotations of representative grains during straining

Displacement, μm	Relative rotation between grain pairs, degrees				
	CD	DF	DI	CI	FI
1	*	1	-1	-1	0
2	0	*	*	*	-1
6	*	*	*	5	4
8	-1	4	4	5	10
25	0	7	6	6	15

* = insufficient lattice image contrast for accurate measurement

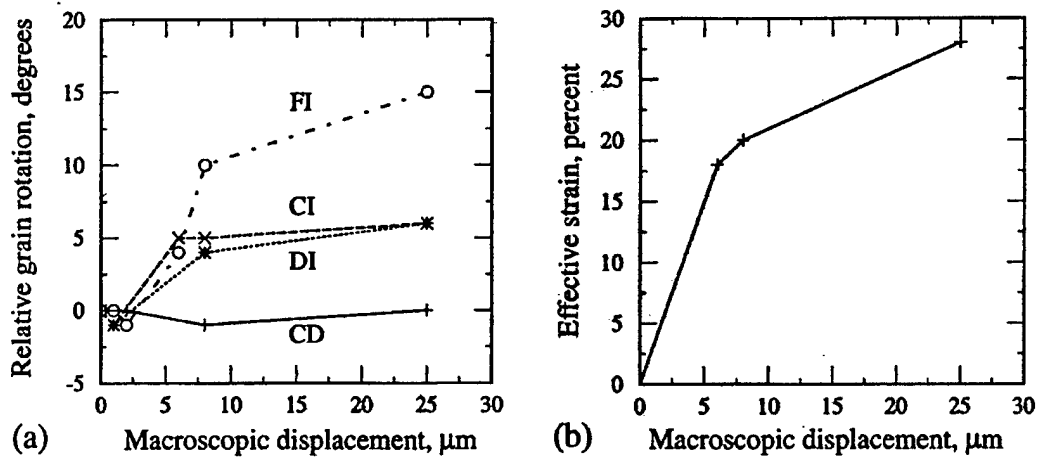


Figure 5.8 Grain rotation and plastic strain during in situ loading. (a) Relative changes in angle during deformation between representative pairs of grains shown in Figure 5.6, as a function of displacement of the straining stage. Accuracy of measurement is ± 2 degrees. (b) Effective plastic strain measured in the same area.

The observation of grain rotation may imply the occurrence of strain via grain boundary sliding. Thus, it is of interest to determine the local strain tensor and the level of plastic strain associated with the deformation. Tensile loading of a cracked thin film is a plane stress situation, which simplifies the analysis. Therefore, the 2-D strain tensor may be determined by measuring the change in shape of a triangle in the deforming zone. By measuring the change in length of the sides of the triangle, an indication of normal strain in three different directions is obtained. This is analogous to a standard mechanical engineering "strain gage rosette" technique for measuring strains in a plane, and elementary relations are available for determining the strain tensor in two dimensions from the three independent normal strain measurements [128]. This technique should give a good approximation of the 2-D strain tensor when the changes in angle between the sides of the triangle are small. If elastic strains are much smaller than plastic strains, constancy of volume can be assumed, requiring that the sum of the normal strains must be zero. This allows the calculation of the normal (Poisson) strain in the direction of the film normal. A simple, scalar indication of the extent of plastic deformation is the "effective strain", which can be easily calculated from the plastic strain tensor [129]. In uniaxial tension, the effective strain is equal to the plastic strain.

The difficulty in applying the technique described above lies in identifying three material points which can be unambiguously tracked during displacement of the straining stage. In the first analysis, the triangle shown in Figure 5.6 was used to determine the strain tensor. The corners of the triangle were the areal center of Grain S, and the centers of identifiable twins in Grains T and R. A second triangle, using grain boundary triple junctions in the same general area, yielded essentially the same results. With respect to a Cartesian coordinate system in which the foil normal is parallel to z , the crack is propagating along x , and the stress is being applied along y , the following strain tensor was calculated (using the triple junction triangle) for the complete deformation sequence (25 μm macroscopic displacement):

$$\underline{\varepsilon} = \begin{bmatrix} 0.05 & -0.11 & 0 \\ -0.11 & 0.19 & 0 \\ 0 & 0 & -0.24 \end{bmatrix}$$

It is difficult to access the accuracy of this strain tensor. There are inevitable errors in identifying the same material point from step to step, which is necessary for placing the triangle. This is the major source of error. The measurement of the lengths of the triangle sides and angles will introduce further error. Finally, there is likely a stress gradient in the zone of interest ahead of the crack tip, and the analysis assumes uniform strain. Due to all of these uncertainties, the above- determined strain tensor must be viewed as a first approximation only. At this level of accuracy, the rosette-like analysis is a reasonable means for measuring the strain tensor. Confidence in this approach was developed further by comparison with a rigorous analysis, including finite plasticity and determination of the rotation tensor, which gave essentially similar results.

The effective strain associated with the above plastic strain tensor is 28%. Even with the uncertainties in strain determination, it is clear that large plastic strains occurred, and that the plastic strain was much larger than the elastic strain. The effective strain is plotted against macroscopic displacement in Figure 5.8(b). The trends are consistent with the observed grain rotations (Figure 5.8(a)), in that the relative grain rotations and the effective plastic strains both changed much more rapidly in the first 8 μm of macroscopic displacement than in the final 17 μm .

(iii) *The Mechanisms of Plasticity in Larger (>100nm) Grain Size Nanostructures [111]*

Thin films with larger grain sizes were prepared by evaporation. Due to significant advantages in ease of film preparation and in the quality of the films, silver was used for this portion of the research instead of gold. In thin films with grain sizes around 110 nm, dislocations were observed both during and after *in situ* straining. An example is shown in Figure 5.9, in which a silver film with a grain diameter around 110 nm was strained until the film necked and fractured. Figure 5.9(a) shows a number of dislocations present in the vicinity of the neck, as observed by strain contrast, while Figure 5.9(b) shows a single dislocation present in the neck, as observed by lattice fringe contrast. Dislocation motion was also evident on video images obtained during the straining process. These experiments confirm that dislocations will be found in the *in situ* straining experiments if they are present, and therefore verify that there was no dislocation activity in the 10 nm grain size films.

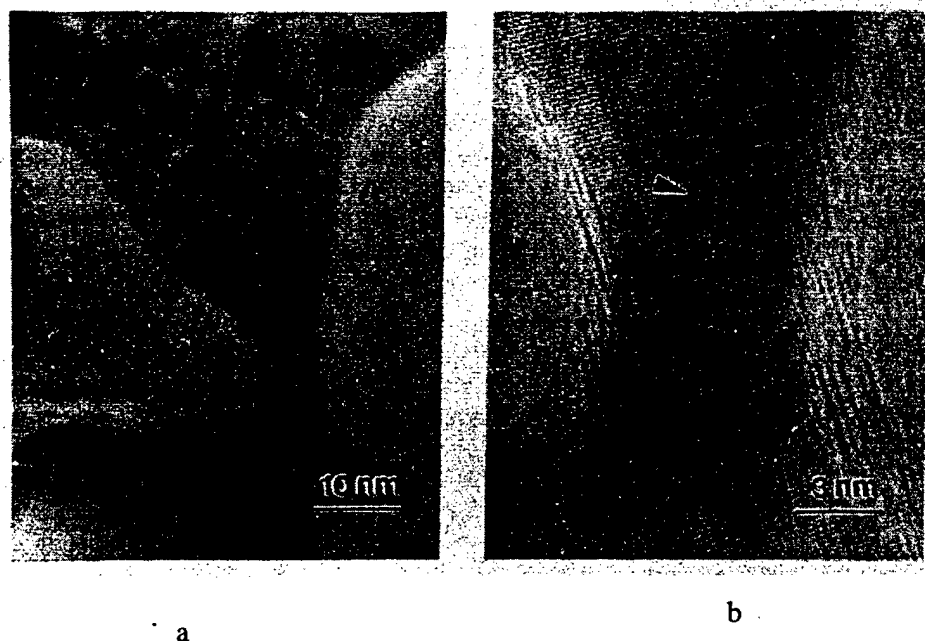


Figure 5.9 Dislocations present after straining a silver film with 110 nm grain size. (a) Multiple dislocations, observable by strain contrast. (b) A single dislocation, observable by lattice fringe contrast.

(iv) Summary of the Deformation Observations of Nanostructured Metal Thin Films [111]

Our studies on nanostructured thin film metals and composites deformed inside a transmission electron microscope (TEM), have allowed us to directly observe deformation mechanisms while they took place. These experiments were the first to demonstrate that metal films deform by grain boundary sliding and grain rotation, even at very low temperatures, when the grain size is 25 nm and smaller [108,111]. These are mechanisms that are normally observed in metals at much higher temperatures. We may summarize our observations in two parts as follows:

a) 10 nm grain size: It is apparent that significant plastic strain occurred simultaneously with the observed grain rotations. These observations are similar to the behavior observed in larger-grain superplastic alloys deformed at elevated temperature. Investigators who study superplasticity generally believe grain rotation is a result of unbalanced shear stresses associated with inhomogeneous grain boundary sliding.

The rotation axis of most of the grains was essentially parallel to the film normal. This is clear because the lattice fringes remained visible after large relative rotations in the film plane, implying that there were no significant rotations which would cause a large change in the Bragg deviation parameter for the lattice planes being imaged. The observation that the grain rotation axis was perpendicular to the film implies that these rotations occurred in response to the applied stress, not to reduce surface energy, grain boundary energy, or in response to some other unspecified driving force.

The magnitude of grain rotation was inhomogeneous, as seen in Figure 5.8. Two possible reasons for this behavior are that the grain boundary structure was not conducive to grain boundary sliding, or that the grain shapes inhibited the rotation process. In any case, the experimental observation suggests that strain inhomogeneities may be present to the extent that local grain boundary fracture processes may be induced. This is consistent with the observation of multiple crack formation in nanocrystalline films with 'pore' formation and growth occurring at triple junctions [108].

The extensive grain boundary sliding, leading to grain rotation, is an effective mechanism of stress relaxation. At this small rate of macroscopic displacement and small grain size, the majority of the plastic strain appears to occur by grain boundary processes. If the contribution of grain boundary sliding to the plastic strain is large, the local stress may not exceed the stress required to generate mobile dislocations inside the grains. The lack of experimentally observed dislocation activity certainly suggests that the stress never exceeded the yield point of the individual grains.

b) *Effects of grain size [111]*: At 10 nm grain size, no apparent dislocation activity was observed and fracture was intergranular, while at 110 nm grain size significant dislocation activity occurred and fracture was transgranular. Further work is in progress to identify the transition grain size. The observation of dislocation activity in the larger-grained films is important, because it verifies that there is no experimental difficulty in imaging dislocations in these nanostructured thin film straining experiments when dislocations are present.

It may be argued that nanostructured metals deform by very rapid dislocation activity, in which dislocations sweep from grain boundary to grain boundary almost instantaneously, thus precluding direct observation. While this may or may not be the case in bulk nanostructured metals, it is difficult to imagine that such a mechanism could occur in thin films like the ones studied here without significant and experimentally-measurable consequences. Plastic strains around 30%, along with relative grain rotations up to 15 degrees, were observed. The grain rotation axis was normal to the foil, and only minor changes in grain shape occurred. In the absence of grain boundary sliding, this deformation would require the motion of a large number of dislocations, with a special distribution of Burgers vectors and slip planes. Presumably, at least a small fraction of these dislocations would be trapped in the grains during deformation, due to dislocation intersection processes if nothing else. Since no evidence of dislocation activity has been found in numerous experiments, it is likely that no significant intragranular dislocation activity occurred in these 10 nm grain size, thin film specimens.

In summary, it was found that nanocrystalline gold films with grain sizes from 8-25 nm deform at room temperature in a ductile manner. However, dislocation motion is not responsible for the deformation, as it would be in traditional grain size gold. Instead, diffusion, pore growth, grain boundary sliding and grain rotation appear to be responsible for the plasticity. Some question remains as to whether this thin film behavior is representative of bulk behavior.

5.3. Experimental Studies on Bulk Nanostructures

While the thin film experiments described above are of fundamental interest for determining deformation mechanisms, and are of interest in the areas of microelectronics and coatings, they are not structural materials. The production of bulk nanostructures for load-bearing components has been problematic for the entire materials community. The production of nanostructures is only possible in processes occurring far from equilibrium, by techniques such as gas condensation, ball milling, or thin film deposition. The product is a powder or thin film that must be consolidated. Consolidation of powders generally requires time at high temperatures, which coarsens the grain size catastrophically.

In this research, two techniques have been utilized to avoid catastrophic coarsening during consolidation. First, a two-phase system (Fe/Cu) which phase-separates has been chosen for initial studies; this type of system allows for pinning of grain boundaries by the minor phase, resulting in less coarsening. Second, rapid powder forging techniques have been adopted to fully consolidate nanostructured powders in a very short time at high temperature. The details are reported in Refs. [112,114].

(i) Structure and Mechanical Behavior of Bulk Fe-10%Cu Nanostructures [112,114]

Mechanical ball milling was used to produce nanostructured powder particles with grain sizes around 15 nm. (Smaller grain sizes, down to 4 nm, have been obtained by others with this technique.) A 90% iron - 10% copper alloy was studied, because copper is insoluble in iron. The structure which results after consolidation consists of copper precipitates on the iron grain boundaries, and these precipitates impede grain growth during processing. Consolidation of the powders into bulk materials was accomplished by hot isostatic pressing (HIP) and forging. The forging technique, which is more promising than the HIP technique because it is faster, is under development presently and is discussed in the next section.

Alloys HIP'ed at 600 and 700°C for 30 minutes at 170 MPa were fully dense. As expected, the grain size coarsened substantially from the original 18 nm size. The final average grain sizes were approximately 100 nm after a 600°C HIP and 130 nm after a 700°C HIP. While significantly coarser than the 10 nm grain-size materials discussed above, these materials are still much finer than traditional steels, and may be considered to be in the upper range of "nanostructured materials."

The mechanical and deformation behavior of these materials were quite surprising; essentially, they behaved in an elastic-perfectly plastic manner. This is demonstrated in the stress strain curves of Figure 5.10. In this figure, the iron material had much coarser grain size than the alloys, and it exhibited traditional strain-hardening behavior. The nanostructured alloys, however, exhibited either no strain hardening or softening upon yield.

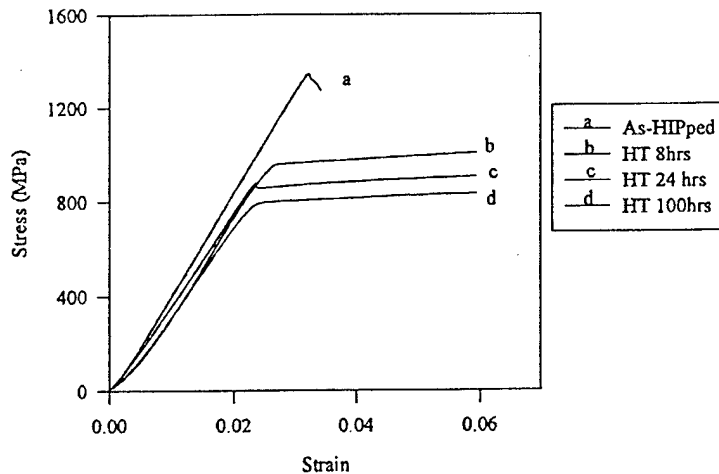


Figure 5.10: Stress-strain curves obtained in compression, nanostructured Fe/Cu alloys.

The deformation mechanisms observed were also quite surprising. The first mechanism of plastic deformation was intense shear banding. Shear banding at the yield point was observed at all grain sizes investigated, from 100 nm to around 650 nm. As the grain size increased, the strength decreased and the shear band width increased. Typical shear bands from representative specimens are shown in Figure 5.11.

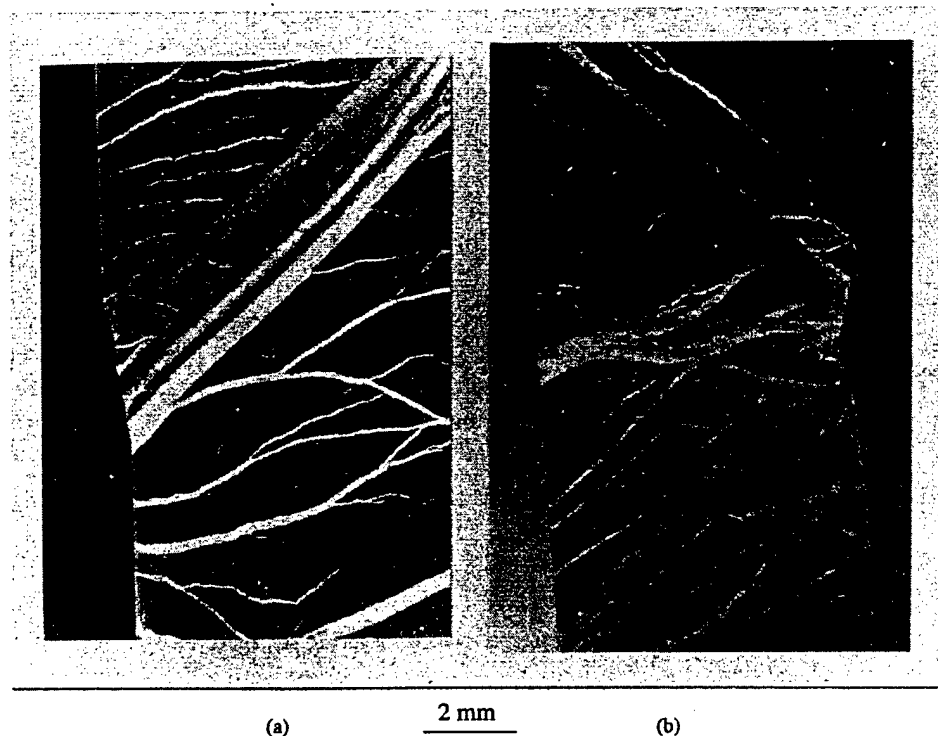


Figure 5.11 Massive shear bands observed on surfaces of compression specimens. (a) 100 hour heat treatment, grain size approximately 500 nm. (b) 500 hour heat treatment, grain size approximately 650 nm.

The observation of shear banding as the first mechanism of permanent deformation, at static strain rates, appears to be unique among metals. Shear banding is normally observed at very high strain rates, and/or after large amounts of cold work, but not in annealed metals at slow strain rates. This behavior is observed, however, in amorphous polymers and metallic glasses [112]. This commonality of behavior between the nanostructured metals and amorphous materials is intriguing, and is being studied currently. Another interesting point is that the grain sizes present in these nanostructured alloys are on the same order of magnitude as the *sub-grain* size which is typically obtained before cold-worked metals begin to undergo shear-banding instabilities. This similarity may be a key in understanding shear banding, both in nanostructured metals and heavily cold worked metals.

The mechanism of plastic deformation inside the shear bands is a topic of continuing study. Transmission electron microscopy of shear-banded material has revealed that the deformation within the bands is intense, while there is no deformation outside the bands. Figure 5.12 shows transmission electron microscope photos of a nanostructured iron alloy HIP'ed at 600°C, with an average grain size around 100 nm. In Figure 5.12(a), the grains maintain their original structure, while in Figure 5.12(b), the grains have been deformed and elongated to an aspect ratio of about 10:1. These photos were taken in

adjacent regions of the same specimen, approximately 10 μm apart, giving lucid evidence of the localized deformation mechanism which is occurring.

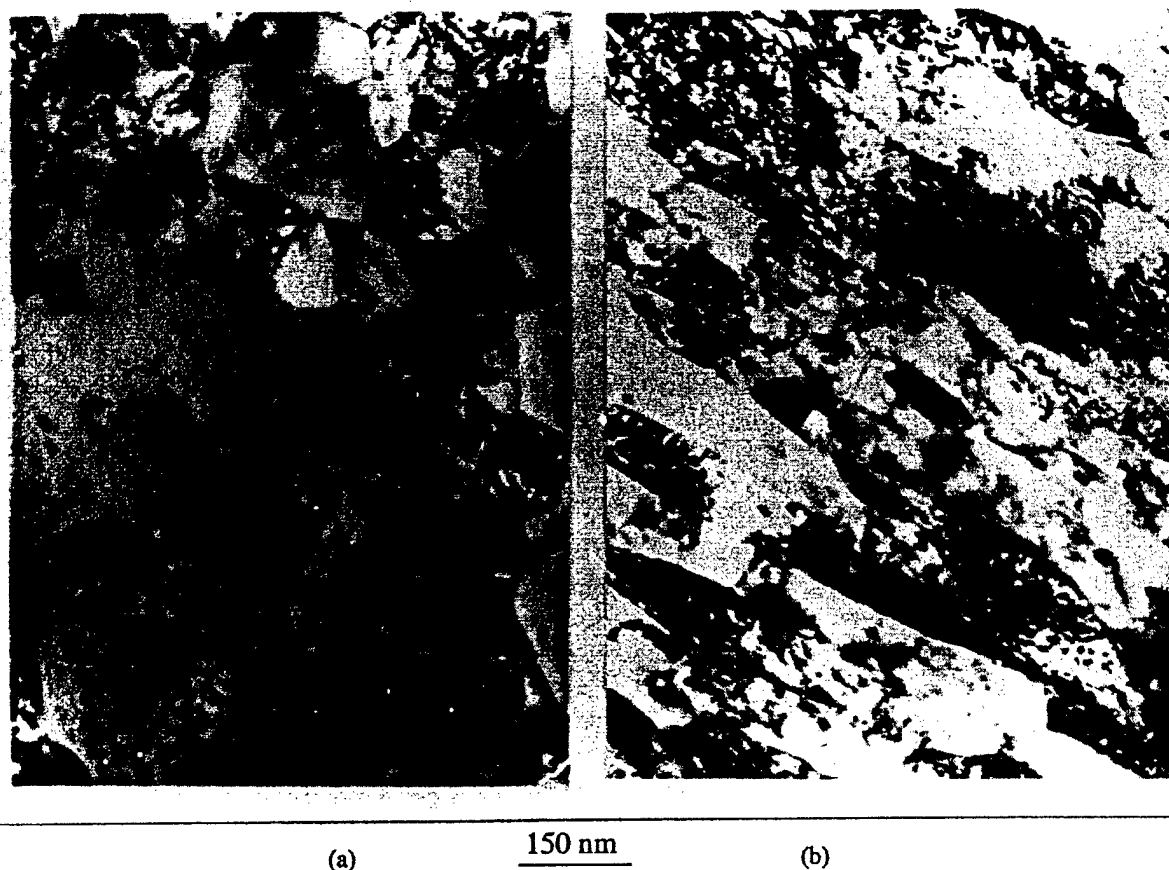


Figure 5.12 Transmission electron micrographs of shear banding in approximately 100 nm grain size Fe-10% Cu. (a) undeformed region. (b) highly deformed region about 10 μm away from the region shown in (a).

(ii) Rapid Powder Forging of Bulk Nanostructures

The HIP techniques were not able to consolidate Fe/Cu materials to full density without coarsening the grain size to a minimum of 100 nm. Further, the lack of shear deformation in the isostatic press precludes the shear flow necessary to heal processing defects. Therefore, rapid powder forging was evaluated as a consolidation technique at the end of this program.

Nanostructured iron/copper powders were cold pressed to approximately 90% density with a uniaxial pressure of 700 MPa at room temperature in a disposable 316 stainless steel die. The die was a cylinder, with a 25 mm outside diameter and a 12 mm inside diameter, along with a lower disk and a plunger made of a nickel-base superalloy. Cold pressing was conducted in the same argon glove box that mechanical milling and storing of the powders were done in, to avoid contamination and oxidation. The same die was transferred quickly to an argon-filled chamber in a servohydraulic loading frame. The

entire die/powder assembly was rapidly heated under argon with an induction heater to temperatures between 500-700°C, and then pressed at 500 MPa and quickly cooled. The time at temperature was less than 2 minutes, as compared to approximately 40 minutes in the HIP. The specimen processed at 700°C, which is the only one which has been evaluated to date, was fully dense. The hardness of this specimen was approximately the same as the specimen which was HIP'ed at 100°C cooler, indicating that the grain size was approximately 100 nm. Current research is exploring lower temperature forging processes, in the hopes of obtaining fully-dense materials with grain sizes in the 50 nm regime.

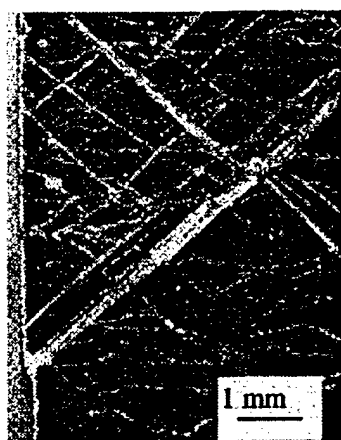
(iii) Summary of Fabrication and Deformation Behavior of Bulk Nanostructures

A brief summary of both fabrication and deformation behavior including shear band formation results of bulk nanostructured metals is given below:

a)*Processing:* These materials are very difficult to produce in bulk form, because the typical processing procedures used to obtain nanostructured grains result in fine powders. These powders must be consolidated into bulk form by the application of pressure and temperature simultaneously. Unfortunately, the application of high temperature results in rapid grain growth, since the driving force for coarsening (reduction of grain boundary area) is high at ultra-fine grain sizes. We developed a rapid forging technique that resulted in fully-dense nanostructured metals, with very high purity. Mechanics modeling was successfully applied, and can be used to predict the densification rate. These results are reported in [130]. Iron with 10% copper was the model system chosen for this work, because it is possible to prepare it by ball milling with limited contamination, and consolidate it with minimal grain growth. Bulk samples with grain sizes from 45nm to 1.7 μ m were prepared.

The most interesting aspect of the work has been the recently-discovered mechanical behavior. These nanostructured metals behave differently than any other known material. In some ways, they behave like amorphous materials such as metallic glasses and glassy polymers. In other ways, they behave like metals, and some aspects of their behavior are unique. These issues are briefly explained below. Results are available in our already-published papers [112,116,117,118], and a comprehensive description of the results can be found in [119]

b)*Deformation behavior:* The deformation behavior of the nanostructured metals is different than any known metal. The materials are elastic-perfectly plastic; that is, there is a well-defined yield point, followed by plasticity without strain hardening. At the finer grain sizes, a strain softening instability was observed. This stress-strain response is accompanied by highly localized deformation, in the form of macroscopic shear bands. The shear banding occurs immediately after yield, and in no case was homogeneous plasticity observed. Shear bands were observed in both tension and compression. Examples of the shear bands and shear offsets which occurred in compression are shown in figure 5.13. It is seen that the widths of the shear bands increases as grain size increases.



a) 150 nm



b) 450 nm



c) 600 nm



d) 100 nm - fracture

Figure 5.13: Optical photographs of shear bands in compression specimens. Grain sizes are indicated. Wavy lines are intersections of shear bands coming out of the plane of the paper at an angle. (d) shows shear fracture at the end of a test, while (c) shows buckling instead of fracture at a larger grain size.

While metals generally require the occurrence of significant homogeneous plasticity prior to shear banding, metallic glasses and amorphous polymers behave in the same manner as the nanostructured metals. They shear band as the first and only mechanism of plastic deformation, and exhibit perfectly plastic response as well. At the finest grain sizes below 100 nm, it may be considered that the nanostructured metal is a composite consisting of a crystalline “grain” phase and an amorphous “boundary” phase. In such a composite, it is reasonable to postulate that the amorphous phase might control the mechanical behavior, and this would result in similarities between amorphous metals and nanostructured metals. However, in this study, amorphous-like behavior was observed at grain sizes up to almost 2 μm ; in this size regime, the fraction of boundary material is negligible, so amorphous-like behavior would be difficult to rationalize based on a composite model. Research is continuing to explore these issues.

c) *Shear Band Angles and Tension-Compression Anisotropy*: The shear bands did not occur on the plane of maximum shear stress, or on the plane of zero extension, as would be predicted by continuum models. In uniaxial compression, the shear band planes were reproducibly inclined at 49° to the stress axis, instead of at 45° , in plane strain tension, the angles were between 52° and 54° , instead of 55° . Further, the strength in compression was about 30% higher than the strength in tension. While this type of behavior has not been observed in metals, it has been observed in amorphous polymers and some metallic glasses. In these materials, the angle of the shear band and the tension-compression anisotropy have been ascribed to a dependence of yielding on the hydrostatic pressure or the normal stress. In this research, we derived a modified von Mises yield criterion with pressure sensitivity. In conjunction with a zero extension shear instability criterion, this yield criterion was able to correctly predict the angle of the shear band planes and the tension-compression anisotropy of the yield strength. More details can be found in [116] and [117] where results on shear band angles and widths/spacings on bulk ultra fine grained Fe-10%Cu polycrystalline alloys with grain sizes in the 50-2000nm range which were deformed in tension and compression are reported. The experimental results clearly show a strong dependence of the yield stress on the hydrostatic pressure (or normal stress), as well as a perfectly plastic behavior (no hardening or softening) which has not previously been observed for metals. They confirm, moreover, that excessive spatially distributed shear banding is the mechanism responsible for the observed perfectly plastic behavior. In addition, the measured shear band angles and widths were in good agreement with the predictions of the gradient theory.

d) *Effects of Grain Size and Temperature on Strength*: While the nanostructured metals behaved like glasses with respect to deformation behavior and an apparent pressure sensitivity of plasticity, they behaved like traditional metals with respect to the grain size dependence of strength. In traditional metals, the strength (and hardness) as a function of grain size is usually described quite well by the Hall-Petch relation

$$\sigma = \sigma_0 + kd^{-1/2}$$

where σ is the yield stress, σ_0 and k are material constants, and d is the grain diameter. Figure 5.15 shows the nanostructured metal hardness data in the form of a Hall-Petch plot, demonstrating clearly that the nanostructured metals are similar to traditional metals in this respect. Further, the material constants were close to those for pure, coarse-grained iron.

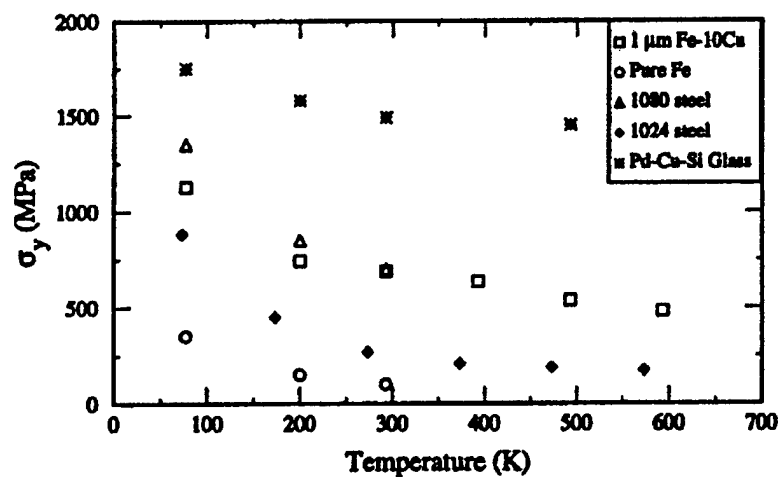


Figure 5.14: Yield strength as a function of temperature for ultra-fine grained Fe-10Cu and other engineering materials.

Figure 5.14 shows the temperature sensitivity of the strength of Fe-Cu materials heat treated to have a grain size near $1\mu\text{m}$. The plot shows data mostly for temperatures below room temperature, a regime in which traditional steels and metallic glasses exhibit a strengthening effect. It is observed that the fine-grained iron-copper behaves in a way that is intermediate between iron and metallic glasses, and behaves almost exactly like 1080 steel.

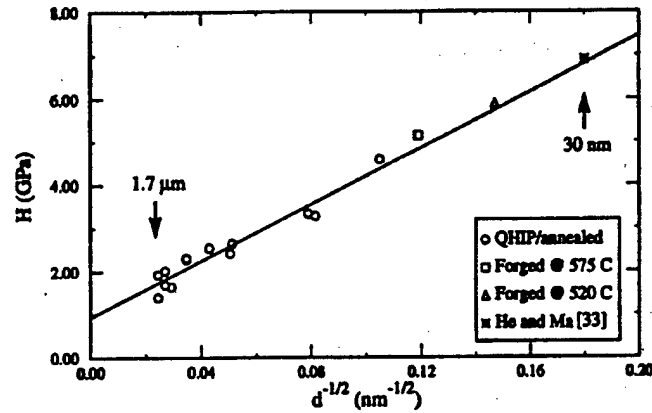


Figure 5.15: Hall-Petch plot of the hardness of the ultra-fine grained Fe-10Cu alloys. Hall-Petch relation is obeyed, and the constants are reasonably close to those of pure iron.

It follows from the above a)-d) that the behavior of the nanostructured and micron-size Fe-Cu materials is unique. They act like metallic glasses and amorphous polymers with respect to deformation localization, shear band angles, and the tension compression anisotropy of strength, but they behave like steels with respect to Hall-Petch behavior and temperature sensitivity of strength. These observations have given us the opportunity to full explore deformation instabilities in several classes of materials. Our goal is to develop a deeper understanding of the mechanical behavior of materials in general, across the material structure length scales spanning from subnanometer (amorphous materials) to nanometer (nanostructured metals) to micrometer and millimeter (traditional metals).

5.4. Modeling the Mechanical Properties of Nanostructures

Modeling of nanostructured materials has been approached in an interdisciplinary environment, from several different points of view. In particular, we have established (i) A model for the grain size dependence of the yield strength of nanostructures, (ii) A model for the critical grain size and strain rate necessary for dislocation-based plasticity in nanostructures, (iii) A gradient elasticity model for nanostructures with application to predicting oscillatory crack profiles, (iv) Two plasticity models for nanostructures accounting for nanopore growth and coalescence and (v) A model of shear band inclination and thickness analysis in relation to the observed asymmetry in tension/compression of bulk nanostructures. Some of these results can be found in Refs [110] for (i), [131,132] for (iii), [107] and [113] for (iv). Results on (ii) and (v) can also be found in Refs [115] and [116,117] and these will also be summarized below:

(i) A Model for the Critical Grain Size and Strain Rate Necessary to Obtain Dislocation- Based Plasticity in Nanostructured Materials [115]

As discussed earlier in Section 5.2, there was a transition in deformation mechanisms in the nanostructured metal thin films as a function of grain size. Below 25 nm, dislocations were not present, and fracture was observed to occur along the grain boundaries. However, above 100 nm grain size films show traditional deformation mechanisms usually observed in large grain size materials; that is, extensive dislocation activity which induces plastic thinning, ligament formation and ductile fracture within an individual grains. The strain rate in both cases was slow, $\sim 10^{-4}$ /s. The purpose of this section is to examine the change in deformation mechanism which was observed between specimens with a 10 nm grain size and specimens with a 100 nm grain size. Given that the strain rates for the deformation experiments on the large and small grain materials are essentially the same, a key question is what role that grain size might play in this phenomenon.

There are indications that the local stresses are quite high during the deformation of the 10 nm materials. Small pores (~ 1 nm) are observed to open up at the grain boundary triple junctions located just ahead (~ 50 -100 nm) of the crack tip [108,115]. These pores appear to be what are referred to as r-type cavities [133], known to occur as a result of grain boundary sliding. Based on the usual analysis, the pore diameter can be related to the local stress through the relation

$$\sigma > \frac{n\gamma}{r} \quad (5.1)$$

where γ is the interfacial energy and r is the pore radius. The value of n in the case of a cylindrical pore at a triple junction may be taken as 0.5-0.7 depending on the contact angle. The stress is therefore determined to be on the order of ~ 1 GPa or $\sim 10^{-2} G$, where G is the shear modulus. Although this is well beyond the yield point of 'normal' Au or Ag, no dislocation-based plasticity was observed in the experiments described in Section 5.2(ii). The individual crystals in the nanograin material appear to have a significantly higher yield point than the corresponding normal grain size material. It is proposed here that this is related to the lack of dislocations, and thus the lack of dislocation sources, in the interior of nanocrystalline grains. This points to an analogy with the mechanical behavior of a defect-free whisker. It should not be surprising that the behavior of a grain in the nanocrystalline material has a high yield point for dislocation-based plasticity if dislocation production is difficult.

As previously noted, no dislocations were observed in the interior of the grains in the 10 nm grain size material. A possible explanation of this observation and the resulting implications for the mechanical behavior of the nanocrystalline material is the image forces on dislocations due to the close proximity of grain boundaries. Attractive forces between dislocations and grain boundaries arise because there are no long range stresses associated with the low energy dislocation structure at a grain boundary. The elastic energy of a dislocation is therefore less in the organization of a grain boundary structure than a dislocation isolated in the grain interior [134]. As a result, there will be a reduction in energy as the dislocation approaches the grain boundary, provided there is sufficient thermal energy to allow for rearrangement of the grain boundary structure. This type of thermal energy is likely present during the deposition process. The strain energy of a dislocation can be written in a general form applicable to the two limiting cases to be considered in this model

$$\frac{\text{energy}}{\text{length}} = \frac{Gb^2}{4\pi} \ln \left(\frac{x + D/2}{b} \right) \quad (5.2)$$

Eq. (5.2) is applicable when $x \gg D$ and when $x=0$, where x is the distance from grain boundary and D is the spacing of dislocations in the grain boundary. For these two limiting cases, Eq. (5.2) reverts to the relevant expressions in [134]. The magnitude of the image force per unit length is determined by the derivative of Eq. (5.2) with respect to x . The image force per unit length (τb) acting to move a dislocation in the center of a grain of diameter d to the grain boundary is thus determined as the derivative of Eq $\sigma_f(\epsilon) = \sigma_{\infty}(\epsilon) + \beta'(\epsilon)d^{-1/2}$ evaluated at $x=d/2 \gg D$, or

$$\tau b \approx \frac{Gb^2}{2\pi d} \quad (5.3)$$

where τ is the image stress. For a dislocation to be stable in the vicinity of the grain boundary during processing, the image stress must be less than the stress necessary to move dislocations from their original (grown in) positions. It is not straightforward to determine this stress. In the case of glissile dislocations on the $\{111\}$ glide planes, and ignoring pinning effects of the grain boundaries on the “ends” of the dislocations as well as line tension forces (as the dislocation bows towards the grain boundary) and solute strengthening, this resisting stress would be the $\{111\}<110>$ CRSS of pure gold, about 1-3 MPa depending on the purity. However, grown-in dislocations often thread crystals on planes other than the glide planes, and so the resisting stress may be dominated by the CRSS on non-glide planes. Further, thin film deposition is an energetic process, and so climb may be important. As a first approximation, we assume here that the resisting stress is about equal to the “yield stress” of commercial purity gold or silver, about 35 MPa. For $d=10$ nm, the image stress is on the order of $4 \times 10^{-3}G$ or around 300 MPa. This is substantially greater than the yield point of normal Au or Ag (~35 MPa). This suggests that any dislocations which might be present in the grain interior during processing when the material is ‘hot’ would be forced to the grain boundary, resulting in dislocation free nanocrystallites. However; if the 100 nm grains are considered, Eq 5.3 determines an image stress on a dislocation at the grain center which is less than the yield stress. This suggests that the dislocations are stable at the grain center and may act as sources for dislocation reproduction.

The image force approach can be extended to consider the stress required to activate a grain boundary source by evaluating the derivative of Eq.(5.2) with respect to x at $x=0$ and assuming that $D=b$. This approximates the stress required to pull a grain boundary dislocation into the grain interior as

$$\tau_{gb} \approx \frac{G}{2\pi} \approx 12 \text{ GPa} \quad (5.4)$$

This appears to be well above the stress determined by the pore diameter measurements. In fact, at low strain rates grain boundary sliding may act to keep the stress lower than τ_{gb} . Application of the Mukherjee model [135] of grain boundary sliding controlled plasticity to our case where $d=10$ nm, the strain rate is $10^{-4}/s$, and the grain boundary diffusion coefficient is $10^{-15} \text{ cm}^2/s$ gives a stress which is consistent with the pore diameter measurement. For this diffusion coefficient, the Mukherjee model has the form for Au/Ag

$$\dot{\epsilon} \approx \frac{10^4}{s} \left(\frac{b}{d} \right)^2 \left(\frac{\sigma}{G} \right)^2 \quad (5.5)$$

Using Eqs (5.4) and (5.5), it is possible to determine a critical strain rate at which dislocation based plasticity due to grain boundary sources might occur. In other words, when the stress in Eq. (5.5)

approaches the value of $\dot{\epsilon}_c$ in Eq. (5.4), grain boundary sources may become active. Carrying out this algebraic manipulation determines the critical strain rate at

$$\dot{\epsilon}_{\text{critical}} \approx \frac{10^4}{s} \left(\frac{b}{d} \right)^2 \frac{1}{4\pi^2} \quad (5.6)$$

Eq. (5.6) agrees with the experimental observations in that the strain rate present in our experiments ($10^{-4}/s$) is too low to observe grain boundary dislocation sources in the 10 nm material. But this strain rate is also just below what is required to observe active grain boundary dislocation sources in the 100 nm grain size material. However, dislocation sources may be present in the interiors of these larger grains. Another limiting factor as to the operation of grain boundary sources is the consideration that the large stresses required to activate dislocation sources in the 10 nm grains will not occur at the head of a pile-up, for there are no dislocations in the grain interior. In this case, dislocation structures cannot induce a line source of stress at the grain boundary. Instead, the stress will be applied more uniformly to the grain boundary. This may cause a loss of cohesion at the grain boundary and failure by brittle fracture before the activation of grain boundary sources.

(ii) Yield and Shear Band Analysis of Bulk Nanostructured Materials

This section is devoted to the discussion of the yield behavior of pressure-sensitive ultra-fine grained Fe-10%Cu alloys with emphasis on shear band width and orientation in both tension and compression. For convenience we divide the discussion in three parts

a) *Summary on Sample Preparation and Testing:* Fe-10% Cu alloys were fabricated with powder metallurgy techniques. Mechanical alloying of elemental powders with an attritor system resulted in an ultra fine grained, single phase, supersaturated solid solution powder alloy in which the copper atoms occupied sites on the bcc iron lattice. The grain size was estimated with x-ray diffraction techniques to be 18 nm. Consolidation of the powders by hot-isostatic-pressing caused phase separation, nucleation and growth of copper particles, and coarsening of the iron grains. The copper grains were nucleated on the iron grain boundaries and triple junctions. The average grain size of the consolidated samples ranged from 90 nm to 160 nm depending on the consolidation parameters. Subsequent annealing treatments effectively coarsened the structure such that the average grain size of the alloy (including both copper and iron grains) ranged from 90 nm to 1.7 μm . Average grain sizes of the coarsened structures were estimated by point-counting techniques with electron and optical microscopy. Mechanical testing of these alloys included Vickers hardness testing, uniaxial compression testing and uniaxial tension testing. The compression test sample geometry was rectangular with an approximately square cross-section and an aspect ratio of ~ 2 , as shown in Figure 5.16. The tensile test samples were rectangular, dogbone-shaped samples, also shown in Figure 5.16. Hardness test results displayed positive grain size hardening as compared with the scale of the microstructure and in accordance with the Hall-Petch relationship as detailed by Carsley [136] and are also explained in [119].

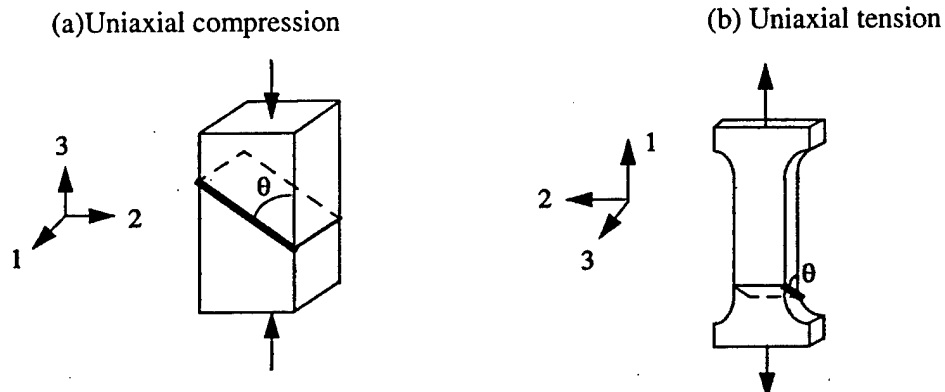


Figure 5.16: The geometry of the test samples, with schematic representation of the shear band planes

Plastic deformation of these samples was not uniform, but proceeded by inhomogeneous, localized shear banding. Figure 5.17 shows an optical micrograph of a typical compression sample with its corresponding stress-strain curve. It is seen that the alloy displayed nearly perfectly plastic behavior right from the yield point and deformed by intense shear banding as the only mode of plastic deformation. The angle between the load axis and the plane of the shear band was 49° as shown in the micrograph of Figure 5.17 and the schematic of Figure 5.16. All compression samples shear banded at this orientation regardless of the structural scale.

Results of the tension testing also indicated perfectly plastic behavior with deformation occurring by shear banding as shown in Figures 5.16 and 5.18. It is seen that the shear band is contained within the "fillet" region rather than in the gage section of the sample. This was true for all tests. The trace of the shear band planes on the surface of the sample shown (plane 1-2) are at $\sim 90^\circ$ with respect to the load axis. The shear band planes, however, are oriented at an angle of $\sim 54^\circ$ from the load axis (as seen on plane 1-3). This angle was measured from the trace of the shear band plane on the thin sample surface which is also shown in the Figure 5.18. Further, the magnitude of the tensile yield strengths were observed to be only about 70% of the compressive yield strengths for common grain sizes.

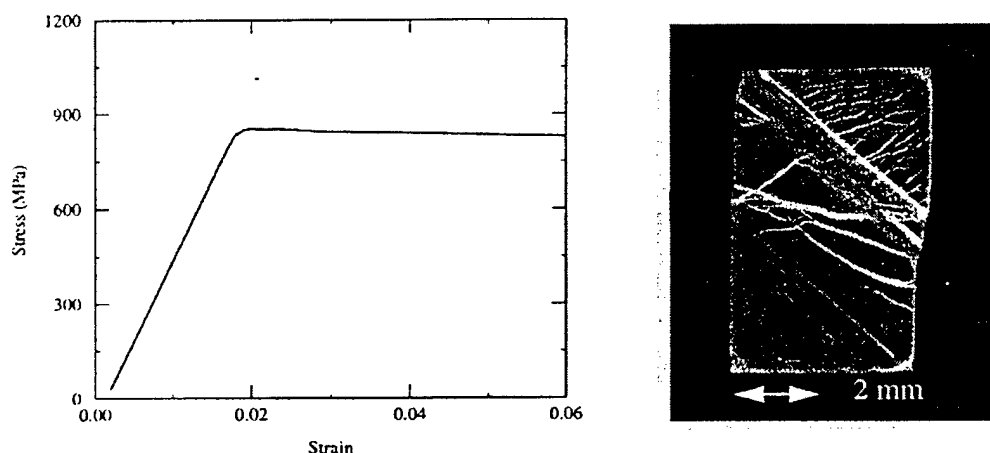


Figure 5.17: Compression test sample: stress-strain curve and optical micrograph showing the shear bands.

As already pointed out, the aforementioned experimental details and results are contained in [136] and they are also reported in [119]. The yield and associated shear band angle and shear band width measurements can be directly used to validate the various, theoretical arguments proposed to modeling the mechanical behavior of these materials as discussed in [116].

b) *Basic Theoretical Relations Employed:* The main theoretical relations from [116] to be used in connection with the experimental results given here are the following:

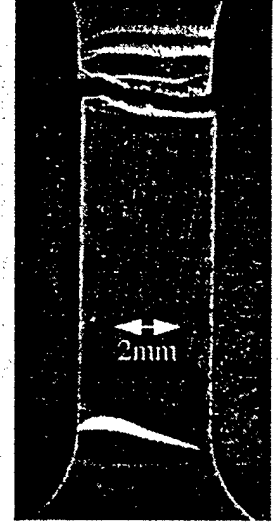
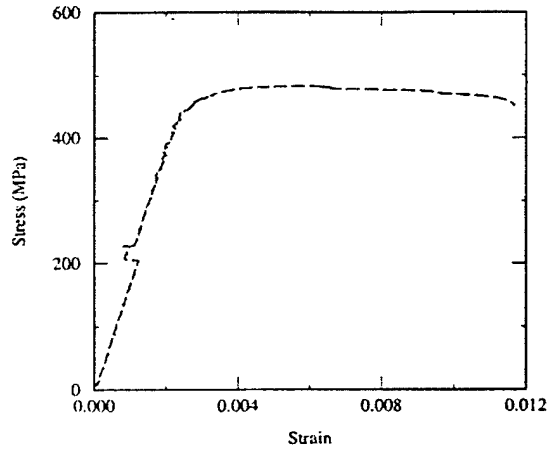


Figure 518: Tension test sample: stress-strain curve and optical micrographs showing the shear bands.

- Yield strength in tension:
$$\sqrt{J_2} + \alpha p = \frac{1}{\sqrt{3}} \sigma_1^{ys} + \frac{\alpha \sigma_1^{ys}}{3} = \kappa \quad (5.7)$$
- Yield strength in compression:
$$\sqrt{J_2} + \alpha p = -\frac{1}{\sqrt{3}} \sigma_3^{ys} + \frac{\alpha \sigma_3^{ys}}{3} = \kappa \quad (5.8)$$
- Shear band angle in plane strain tension:
$$\theta = \frac{\pi}{4} + \frac{1}{2} \sin^{-1} \left(\alpha \sqrt{\frac{3}{3-\alpha^2}} \right) \quad (5.9)$$
- Shear band angle in uniaxial compression:
$$\theta = \frac{\pi}{2} - \frac{1}{2} \cos^{-1} \left(\frac{1}{3} - \alpha \frac{4}{3\sqrt{3}} \right) \quad (5.10)$$
- Shear band width:
$$w = 0.4 \sqrt{\frac{R^2}{10} \left(G \frac{7-5\nu}{15(1-\nu)} + h \right)} \quad (5.11)$$

The above relations result from a pressure-dependent yield condition, a zero-extension shear band criterion, and a gradient-dependent estimate of shear band width as discussed below:

- Pressure-Dependent Yield Condition

The pressure-dependent yield condition reads

$$f = f(\sigma_{ij}) = \sqrt{J_2} + \alpha p - \kappa = 0 \quad (5.12)$$

where $p = \frac{1}{3} \sigma_{kk}$ is the pressure and $J_2 = \frac{1}{2} S_{ij} S_{ij}$ ($S_{ij} = \sigma_{ij} - p \delta_{ij}$) is the second invariant of the deviatoric stress. The coefficient α is a material parameter denoting the effect of hydrostatic stress on the yield strength κ . Moreover, Eq (5.12) indicates that plastic deformation must be accompanied by a change in

volume proportional to the magnitude of α which must be less than $\sqrt{3}/2$ because a greater value would imply expansion in three dimensions under uniaxial tension. This property, commonly known as dilatancy, was the initial motivation for postulating on a phenomenological basis a yield criterion of the form of Eq (5.12) for soils (Drucker-Prager yield condition, see also [5]). A motivation for adopting Eq (5.12) for the present ultra-fine grained alloys may be sought to our earlier mentioned observations on nanostructured thin films and ultra fine grained bulk samples revealing the possibility of plastic deformation via the mechanisms of void formation and growth at triple grain boundary junctions as well as by grain rotation in addition to the traditional mechanism of conservative dislocation glide which is the dominant mechanism of plastic flow at larger grain sizes. It is thus natural to expect that yielding in these materials would depend on hydrostatic pressure, as this has a direct effect on vacancy generation and motion which, in turn, facilitate dislocation climbing processes, as well as void nucleation and growth. In fact, the pressure-dependent yield condition given by Eq (5.12) was readily derived in [5] on the basis of dislocation glide and climbing processes.

- Zero-Extension Criterion for Shear Band Orientation

A simple zero extension criterion $\epsilon_t = 0$ was proposed in [137] in conjunction with the yield condition (5.12) for determining shear band angles in pressure-sensitive plastic materials. This criterion, which proposes that the shear band occurs on the plane in which the normal strain is zero, has been shown [138] to be more appropriate than using the maximum shear stress as the angle criterion. It turns out [116,117] that for the compression and tension configurations depicted in Figure 5.16, the above criterion produces the following results for the shear band inclination angle θ .

Compression Samples: In the case of compression, the deformation state is uniaxial throughout the sample. The stress state is a special case of plane stress ($\sigma_1 = \sigma_2 = 0$, $\sigma_3 < 0$) and the shear band angle on

the 2-3 plane is given by [137] $\theta = \frac{\pi}{2} - \frac{1}{2} \cos^{-1} \left(\frac{1}{3} - \alpha \sqrt{\frac{16}{27}} \right)$

Tension Samples: When shear band failure takes place in section B, the sample is in an overall state of uniform, uniaxial tension. Then, it turns out that the zero extension criterion gives [137]

$$\theta^B = \frac{\pi}{4} + \frac{1}{2} \sin^{-1} \left(\frac{1}{3} + \alpha \sqrt{\frac{16}{27}} \right)$$

Next, we consider the case when shear band failure takes place in section A. This section is in plane strain tension on plane 2 ($d\epsilon_2$). The shear band angle on plane 2 is determined by applying the zero extension

criterion on this plane and is found in [137] as $\theta^A = \frac{\pi}{4} + \frac{1}{2} \sin^{-1} \left(\alpha \sqrt{\frac{3}{3-\alpha^2}} \right)$

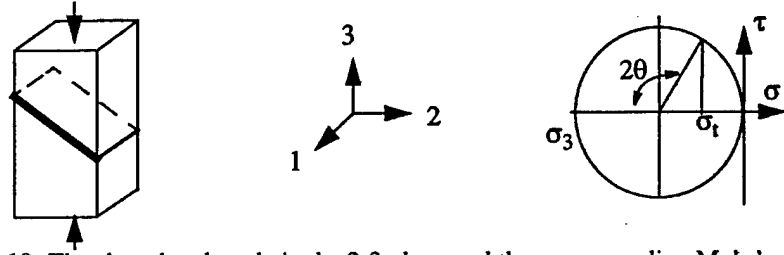


Figure 5.19: The shear band angle in the 2-3 plane and the corresponding Mohr's circle.

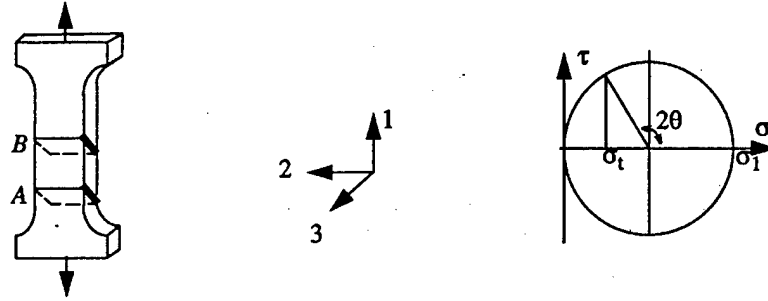


Figure 5.20: The shear band angle in the 1-3 plane and the corresponding Mohr's circle.

In fact for the two shear band configuration depicted in Figure 5.20 the corresponding state of stress is such that $\sigma_1^A = \sigma_1^B = \sigma_1$. In section *B* the planes 2 and 3 (plane *i* with $i=1,2,3$ designates the plane perpendicular to the *i*- axis) are stress free implying that $\sigma_2^B = \sigma_3^B = 0$. In section *A*, because of the influence of the fillet, we have $\sigma_2^A \neq 0$, $\sigma_3^A \neq 0$. The flow rule, $d\epsilon_{ij} = d\lambda \frac{\partial f}{\partial \sigma_{ij}}$, based on Eq. (5.12), reads

[5] as $d\epsilon_{ij} = d\lambda \left(\frac{S_{ij}}{2\sqrt{J_2}} + \frac{\alpha}{3} \delta_{ij} \right)$ where ϵ_{ij} is the plastic strain (elastic deformation is neglected) and the

plastic coefficient λ is determined, as usual, from the yield (or consistency) condition. During the tension process, the fillet region constrains the deformation in section *A* in the 2-direction which implies that

$d\epsilon_2^A$ is very small ($d\epsilon_2^A \sim 0$), i.e. plane strain approximation. Then it follows that $S_2^A = -\frac{2}{3}\alpha\sqrt{J_2^A}$ and,

subsequently, a simple calculation [137] for pressure-dependent plastic materials yields ($\sigma_3 = 0$)

$J_2^A = (\sigma_1^A)^2 / 4 \left(1 - \frac{\alpha^2}{3} \right)$ leading, finally, to the relation $A\sigma_1^A = \kappa^A$ where

$A = \left(\frac{1}{2} \sqrt{\frac{3}{3-\alpha^2}} + \left(\frac{\alpha}{2} - \frac{\alpha^2}{6} \sqrt{\frac{3}{3-\alpha^2}} \right) \right)$. Section *B* is in a state of pure uniaxial tension, so it is easily

concluded that $B\sigma_1^B = \kappa^B$ where $B = \sqrt{\frac{1}{3}} + \frac{\alpha}{3}$. It is noted that κ^A and κ^B denote the stress quantity used to express the yield condition given by Eq. (5.12).

- Shear band width analysis

The results of the previous paragraph on the shear band angles are based on a simple but effective theoretical argument which, however, does not provide any information on shear band widths. An instability analysis for the emergence and evolution of shear bands proposed recently by Aifantis and co-workers [3,5,7a,7b] can provide both shear band angles and shear band widths. This analysis is based on a strain gradient theory of plasticity with a gradient-dependent flow stress of the form $\tau = k(\gamma) - c\nabla^2\gamma$ where τ and γ denote respectively the effective stress and strain ($\tau = \sqrt{J_2} = \sqrt{\frac{1}{2}S_{ij}S_{ij}}$, $\gamma = \sqrt{2\varepsilon_{ij}\varepsilon_{ij}}$,) and c is the strain gradient coefficient. Based on the above mentioned gradient-dependent flow stress expression, an approximate relationship between the width of the shear band w and the gradient coefficient c has been developed in [7b], which reads $w = 0.4\sqrt{c}$. This formula, which was derived for AISI 4340 steel on the basis of an exact nonlinear shear band solution first proposed in [3] (in analogy with a mechanical theory of fluid interfaces [139,140]), can be used to model shear band width trends in a variety of materials.

While shear band width data can be used for the evaluation of the gradient coefficient c , it is desired to obtain independent experimental or theoretical estimates for it. A discussion on the determination of the gradient coefficient c can be found in a recent review article [68,71]. In particular, as detailed in [59] the following relation can be obtained between the gradient coefficient c and the grain size $d = R/2$ of a polycrystalline metal (a typical grain was assumed to be spherical with radius R)

$c = \frac{R^2}{10}(\beta + h)$. The coefficient $h = d\tau/d\gamma$ denotes the plastic hardening modulus and the coefficient β depends on the elastic constants and the self-consistent model used as $\beta = G \frac{7-5\nu}{15(1-\nu)}$ where

G is the shear modulus and ν is Poisson's ratio. The combination of the last three equations listed above lead to Eq. (5.11)

- Comparison with Experiments

In this final section, we use the theoretical relations provided above to describe yielding, shear band angles and shear band widths for the interpretation of the experimental results obtained for the aforementioned ultra fine grained Fe-10%Cu alloy. The details will be given in [119] (see also [136]) and only a brief summary will be reported here which, however, is sufficient to validate the theoretical arguments advanced.

The most consistent and reproducible data obtained from the experiments was the measurement of the shear band angle from the uniaxial compression test samples. The plane of the shear band was oriented at 49° to the load axis and was independent of the scale of the microstructure. Based on this shear band angle, the pressure-sensitive material parameter α was calculated with Eq (5.10) to be 0.25. Shear banding in the tensile samples occurred in the fillet area between the gage and grip sections which is undergoing plane strain deformation, as explained earlier. The angle between the load axis and the plane of the shear bands was measured on the 1-3 plane, as shown in Figures 5.16, 5.18, to be approximately 54° . These

data were used to verify the calculation of the pressure- sensitive parameter. For $\alpha = 0.25$, Eq (5.9) was used to predict a shear band angle for plane strain tension of 52.3° which compares well with the above experimental value.

The observed strength differences in tension and compression (see [119, 136]) provided another opportunity to confirm the pressure dependence of this material. For a given grain size, the yield strength in tension was $\sim 70\%$ of the yield strength in compression as shown in Table 5.2. The yield constant k was estimated from Eqs (1) and (2) for both uniaxial compression and for plane strain tension with a pressure-sensitivity coefficient $\alpha = 0.25$. In actuality, the yield constant is independent of the mode of testing. The calculated results for k , listed in Table 5.2, indicate that the value used for the pressure-sensitivity coefficient ($\alpha = 0.25$) models sufficiently well the measured yield strengths s_1^{ys} and s_2^{ys} entering Eqs (5.7) and (5.8).

Table 5.2: Verification of the yield condition for $\alpha = 0.25$.

Grain size (nm)	Tensile yield strength (MPa)	Compressive yield strength (MPa)	k (tensile) (MPa)	k (compressive) (MPa)
1170	526	721	348	356
1370	484	694	320	343

The yield strengths were used to verify the magnitude of the pressure-sensitivity coefficient α via a different approach. For a given grain size, the yield constant k and the pressure sensitivity coefficient α were solved for simultaneously using Eqs (5.7) and (5.8) and the measured yield strengths in tension and compression. The calculated parameters are listed in Table 5.3. The results indicate that α has a value near 0.25 as determined above. The values of k and α were subsequently used to calculate the shear band angles shown in Table 5.3 with Eqs (3) and (4). Again, the obtained values for the shear band angles agree very well with the experimental data.

Table 5.3: Verification of the pressure-sensitivity coefficient.

Grain size (nm)	k (MPa)	α	θ° (compression)	θ° (tension)
1170	351	0.27	48.6	53.9
1370	329	0.308	47.8	54.1

This close agreement among the determined parameters using two separate approaches (as shown in Tables 5.2 and 5.3), provides further confidence in the model used.

The width of the shear bands was observed to broaden with increasing structural scale (or grain size) of the compression test samples. The widths of the most prominent shear bands were compared to the grain size of the alloys as shown in Figure 5.21. Also shown in the figure (with the solid line) is the obtained estimate of shear band width as a function of grain size given by Eq 5.11. For this purpose, the shear modulus and Poisson's ratio were approximated as those of pure iron as found in the literature. The strain hardening parameter h was assumed to be zero because these materials were nearly perfectly plastic.

It is concluded that the ultra fine grained iron-copper alloys investigated herein, exhibited a mechanical behavior which suggested a strong pressure-dependence of plastic flow. Shear banding occurred as the only mode of plastic deformation from the yield point with nearly perfectly plastic behavior in both tension and compression. The experimental observations on tension/compression yield

strength differences, shear band orientations and shear band widths were consistently interpreted on the basis of a pressure-dependent yield condition and a gradient theory of plasticity with the use of only one additional material parameter.

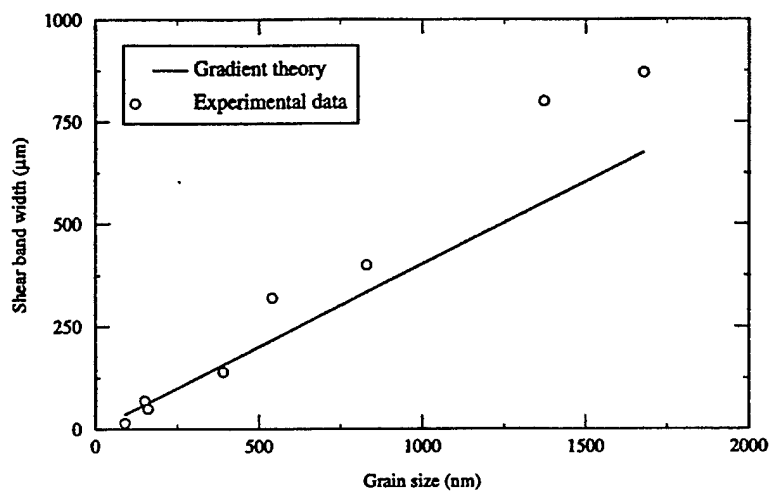


Figure 5.21: Shear band width versus grain size for the compression test samples

6. References

- [1] E.C. Aifantis (1982) Some thoughts on degrading materials. In S.N. Atluri and J.E. Fitzgerald (eds) *NSF Workshop on Mechanics of Damage and Fracture, Georgia Tech., Atlanta*, pp. 1-12.
- [2] E.C. Aifantis (1983) Dislocation kinetics and the formation of deformation bands. In G.C. Sih and J.W. Provan (eds) *Defects, Fracture and Fatigue (Proceedings of International Symposium held in May 1982, Mont Gabriel, Canada)*, pp. 75-84, Martinus-Nijhoff, The Hague.
- [3] E.C. Aifantis, On the microstructural origin of certain inelastic models, *J. Mater. Engng. Technol.* (Transactions of ASME) **106**, 326-330, 1984.
- [4] E.C. Aifantis, Remarks on media with microstructures, *International Journal of Engineering Science* **22**, 961-968, 1984.
- [5] E.C. Aifantis, The physics of plastic deformation, *Int. J. Plasticity* **3**, 211-247, 1987.
- [6] D. Walgraef and E.C. Aifantis, Dislocation patterning in fatigued metals as a result of dynamical instabilities, *J. Appl. Phys.* **58**, 688-691, 1985.
- [7] a) H.M. Zbib and E.C. Aifantis, On the localization and post-localization behavior of plastic deformation - I,II,III, *Res Mechanica* **23**, 261-305, 1988.
 b) H.M. Zbib and E.C. Aifantis, On the structure and width of shear bands, *Scripta Met.* **22**, 703-708, 1988.
- [8] I. Vardoulakis and E.C. Aifantis, Gradient - Dependent dilatancy and its implications in shear banding and liquefaction, *Ingenieur - Archiv* **59**, 197-208, 1989.
- [9] H.B. Mühlhaus and E.C. Aifantis, A variational principle for gradient plasticity, *Int. J. Solids Struct.* **28**, 845-857, 1991.
- [10] B.D. Coleman and M.L. Hodgdon, On shear bands in ductile materials, *Arch. Rat. Mech. Anal.* **83**, 115-137, 1983.
- [11] B.D. Coleman and D.C. Newmann, On adiabatic shear bands in rigid-plastic materials, *Acta Mechanica* **78**, 263-279, 1989.
- [12] L.P. Kubin and J. Lepinoux (1988) The dynamic organization of dislocation structures. In P.O. Kettunen et al (eds) *Strength of Metals and Alloys (ICSMA 8)*, vol. 1, pp. 35-59, Pergamon Press, Oxford.
- [13] L.P. Kubin (1993) Dislocation patterning. In H. Mughrabi (ed) *Materials Science and Technology* (Eds. R.W. Cahn, P. Haasen, E.J. Kramer) - Vol. 6: *Plastic Deformation and Fracture of Materials*, pp. 137-190, VCH, Weinheim-New York-Basel-Cambridge.
- [14] J. Kratochvil and S. Libovicky, Dipole drift mechanism of early stages of dislocation pattern formation in deformed metal single crystals, *Scripta Met.* **20**, 1625-1630, 1986.
- [15] J. Kratochvil, On the dynamic origin of dislocation structures in deformed solids, *Mater. Sci. Engng.*, **A164**, 15-22, 1993.
- [16] P. Hähner, Modelling the spatiotemporal aspects of the Portevin-Le Chatellier effect, *Mater. Sci. Engng.* **A164**, 23-34, 1993.
- [17] P. Hähner, Stochastic dislocation patterning during cyclic plastic deformation of persistent slip band and matrix structures, *Appl. Phys.* **A62**, 473-481, 1996.
- [18] L.J. Sluys and R. de Borst, Dispersive properties of gradient and rate-dependent media, *Mech. Mater.* **183**, 131-149, 1994.
- [19] L.J. Sluys, R. de Borst and H.B. Mühlhaus, Wave propagation, localization and dispersion in a gradient-dependent medium, *Int. J. Solids Struct.* **30**, 1153-1171, 1996.
- [20] T. Belytschko and D. Lasry, Localization limiters in transient problems, *Int. J. Solids Struct.* **24**, 581-597, 1988.
- [21] T. Belytschko and M. Kulkarni, On the effect of imperfections and spatial gradient regularization in strain softening viscoplasticity, *Mech. Res. Comm.* **18**, 335-343, 1991.

- [22] Y. Tomita, Simulations of plastic instabilities in solid mechanics, *Appl. Mech. Rev.* **47**, 171-205, 1994.
- [23] A. Huerta and G. Pijaudier -Cabot, Discretization influence on regularization by two localization limiters, *J. Eng. Mech.* **20**, 1198-1218, 1994.
- [24] A.C. Eringen, *Continuum Physics*, Vols. I-IV, Academic Press, New York, 1971 (Vol. I), 1975 (Vol. II), 1976 (Vols. III,IV).
- [25] A.C. Eringen, Theories of nonlocal plasticity, *Int. J. Engng. Sci.* **21**, 741-751, 1983.
- [26] Z.P. Bazant and T.P. Chang, Instability of nonlocal continuum and strain averaging, *J. Engng. Mech.* **110**, 1441-1450, 1984.
- [27] Z.P. Bazant, T.B. Belytschko and T.P. Chang, Continuum theory of strain softening, *J. Engng. Mech.* **110**, 1666-1692, 1984.
- [28] Z.P. Bazant, Mechanics of distributed cracking, *Appl. Mech. Rev.* **39**, 675-705, 1986.
- [29] Z.P. Bazant and G. Pijaudier-Cabot, Nonlocal continuum damage, localization instability and convergence, *J. Appl. Mech.* **55**, 287-293, 1988.
- [30] R.J. Amodeo and N.M. Ghoniem, A review of experimental observations and theoretical models of dislocation cells and subgrains, *Res Mechanica* **23**, 137-160, 1988.
- [31] L.P. Kubin, Dislocation patterning during multiple slip of FCC crystals-A simulation approach, *Phys. Status Sol. A* **135**, 433-443, 1993.
- [32] I. Groma and G.S. Pawley, Computer simulations of plastic behavior of single crystals, *Phil. Mag.* **A67**, 1459-1470, 1993.
- [33] J.P. Hirth, M. Rhee and H.M. Zbib, Modeling of deformation by a 3D simulation of multiple curved dislocations, *J. Computer-Aided Mat. Design* **3**, 164-166, 1996.
- [34] N. Triantafyllidis and S. Bardenhagen, On higher-order gradient continuum theories in 1-D nonlinear elasticity derivation from and comparison to the corresponding discrete models, *J. Elasticity* **33**, 259-293, 1993.
- [35] N. Triantafyllidis and E.C. Aifantis, A gradient approach to localization of deformation - I. Hyperelastic materials, *J. Elasticity* **16**, 225-238, 1986.
- [36] G.A. Maugin, Internal variables and dissipative structures, *J. Non-Equil. Thermody.* **15**, 173-192, 1990.
- [37] G.A. Maugin and W. Muschik, Thermodynamics with internal variables, part I: general concepts. Part II: applications, *J. Non-Equil. Thermody.* **19**, 217-249, 250-289, 1994.
- [38] K.C. Valanis, A gradient theory of internal variables, *Acta Mech.* **116**, 1-14, 1996.
- [39] C. Polizzotto and G. Borino, A thermodynamics-based formulation of gradient-dependent plasticity, *Eur. J. Mech. A/Solids* **17**, 741-761, 1998.
- [40] H.L. Schreyer and Z. Chen, One-dimensional softening with localization, *J. Appl. Mech.-T. ASME* **53**, 791-797, 1986.
- [41] F. Oka, A. Yashima, T. Adachi and E.C. Aifantis, Instability of gradient dependent viscoplastic model for clay saturated with water and FEM analysis, *ASME Appl. Mech. Rev.* **45**, 140-148, 1992.
- [42] L.J. Sluys and W.M. Wang (1998) Macroscopic modelling of stationary and propagative instabilities. In R. de Borst and E. van der Giessen (eds) *Material Instabilities in Solids*, pp. 489-505, John Wiley and Sons, Chichester.
- [43] S. Ramaswamy and N. Aravas, Finite element implementation of gradient plasticity models, Part I: Gradient-dependent yield functions. Part II: Gradient-dependent evolution equations, *Comput. Methods Appl. Mech. Engrg.* **163**, 11-32, 33-53, 1998.
- [44] G. Pijaudier-Cabot, B. Gerard, N. Burlion and L. Molez (1998) Localisation of damage in quasi-brittle materials and influence of chemically activated damage. In R. de Borst and E. van der Giessen (eds) *Material Instabilities in Solids*, pp. 441-456, John Wiley and Sons, Chichester.
- [45] M.G.D. Geers, R.H.J. Peerlings, R. de Borst and W.A.M. Brekelmans (1998) Higher-order damage models for the analysis of fracture in quasi-brittle materials. In R. de Borst and E. van der Giessen (eds) *Material Instabilities in Solids*, pp. 405-424, John Wiley and Sons, Chichester.

- [46] C. Comi and L. Driemeier (1998) On gradient regularization for numerical analyses in the presence of damage. In R. de Borst and E. van der Giessen (eds) *Material Instabilities in Solids*, pp. 425-440, John Wiley and Sons, Chichester.
- [47] M. Fremond and B. Nedjar, Damage, gradient of damage and principle of virtual power, *Int. J. Solids Struct.* **33**, 1083-1103.
- [48] H. Costa Mattos, M. Fremond and E.N. Namiya, A simple model of the mechanical behaviour of ceramic-like materials, *Int. J. Solids Struct.* **29**, 3185-3200, 1992.
- [49] Y. Estrin, B. Sluys, Y. Brechet and A. Molinari (1998) A dislocation based gradient plasticity model. In A. Bertram et al (eds) *Mechanics of Materials with Intrinsic Length Scale (Proc. Euromech-Mecamat EMMC2)*, pp. 128-135, Otto-von-Guericke-Universität, Magdeburg.
- [50] A. Benallal and V. Tvergaard, Nonlocal continuum effects on bifurcation in the plane strain tension-compression test, *J. Mech. Phys. Solids* **43**, 741-770, 1995.
- [51] L.P. Mikkelsen and V. Tvergaard (1998) A 2-D non-local analysis of hydroforming of thin sheets. In A. Bertram et al (eds) *Mechanics of Materials with Intrinsic Length Scale (Proc. Euromech-Mecamat EMMC2)*, pp. 242-249, Otto-von-Guericke-Universität, Magdeburg.
- [52] Y.M. Leroy and A. Molinari, Spatial patterns and size effects in shear zones: A hyperelastic model with higher-order gradients, *J. Mech. Phys. Solids* **41**, 631-663, 1993.
- [53] C.Faciú and A. Molinari, A non-local rate-type viscoplastic approach to patterning of deformation, *Acta Mechanica* **126**, 71-99, 1998.
- [54] G. Frantziskonis (1993) Heterogeneity and its implications - Micromechanical, statistical, fractal approach and their similarity. In G.Z. Voyiadjis (ed) *Damage in Composite Materials*, pp. 137-160, Elsevier, Amsterdam.
- [55] H. Dai and G. Frantziskonis, Heterogeneity, spatial correlations, size effects and dissipated energy in brittle materials, *Mech. of Materials* **18**, 103-118, 1994.
- [56] G. Frantziskonis, Letter to the Editor, Discussion of "Stochastic approaches for damage evolution in standard and non-standard continua - *Int. J. Solids Struct.* **32**, 1149-1160, 1995", *Int. J. Solids Struct.* **33**, 2261-2265, 1996.
- [57] H.M. Zbib, Strain gradients and size effects in nonhomogeneous plastic deformation, *Scripta Metall. Mater.* **30**, 1223-1226, 1994.
- [58] H.M. Zbib (1994) Size effects and shear banding in viscoplasticity with kinematic hardening. In R.C. Batra and H.M. Zbib (eds) *Material Instabilities*, AMD-Vol. 183 / MD-Vol. 50, pp.19-33, ASME, New York.
- [59] J. Ning and E.C. Aifantis (1996) Anisotropic and inhomogeneous deformation of polycrystalline solids. In A.S. Krausz and K. Krausz (eds) *Unified Constitutive Laws of Plastic Deformation*, pp.319-341, Academic Press, San Diego.
- [60] J. Carmeliet, Optimal estimation of gradient damage parameters from localization phenomena in quasi-brittle materials, *Mech. Coh.- Frict. Mater.* **4**, 1-16, 1999.
- [61] W.J. Drugan and J.R. Willis, A micromechanics-based nonlocal constitutive equation and estimates of representative volume element size for elastic composites, *J. Mech. Phys. Solids* **44**, 497-524, 1996.
- [62] V.A. Buryachenko, Some nonlocal effects in graded random structure matrix composites, *Mech. Res. Comm.* **25**, 117-122, 1998.
- [63] A.E. Romanov and E.C. Aifantis, On the kinetic and diffusional nature of linear defects, *Scripta Met. Mater.* **28**, 617-622, 1993.
- [64] N. Liosatos, A.E. Romanov, M. Zaiser and E.C. Aifantis, Non-local interactions and patterning of misfit dislocations in thin films, *Scripta Materialia* **38**, 819-826, 1998.
- [65] K. Cholevas, N. Liosatos, A.E. Romanov, M. Zaiser and E.C. Aifantis, Misfit dislocation patterning in thin films, *Phys. Stat. Sol. B* **209**, 295-304, 1998.
- [66] E. van der Giessen and A. Needleman (1994) On the solution of two-dimensional plasticity problems with discrete dislocations. In A.K. Noor and A. Needleman (eds) *Computational Material Modeling*, AD-Vol. 42 / PVP-Vol. 294, pp. 53-70, ASME, New York.

- [67] E. van der Giessen and A. Needleman, Discrete dislocation plasticity: a simple planar model, *Modelling Simul. Mater. Sci. Eng.* **3**, 689-735, 1995.
- [68] E.C. Aifantis, On the role of gradients on the localization of deformation and fracture, *Int. J. Engng. Sci.* **30**, 1279-1299, 1992.
- [69] E.C. Aifantis, Gradient effects at macro, micro, and nano scales, *J. Mech. Behavior* **5**, 355-375, 1994.
- [70] E.C. Aifantis (1994) Spatio-temporal instabilities in deformation and fracture. In A.K. Noor and A. Needleman (eds) *Computational Material Modeling*, AD-Vol. 42 / PVP-Vol. 294, pp. 199-222, ASME, New York.
- [71] E.C. Aifantis, Pattern formation in plasticity, *Int. J. Engng. Sci.* **33**, 2161-2178, 1995.
- [72] E.C. Aifantis, Non-linearity, periodicity and patterning in plasticity and fracture, *Int. J. Non-Linear Mechanics* **31**, 797-809, 1996.
- [73]a) N.A. Fleck and J.W. Hutchinson, A phenomenological theory for strain gradient effects in plasticity, *J. Mech. Phys. Solids* **41**, 1825-1857, 1993.
- [73]b) N.A. Fleck, G.M. Müller, M.F. Ashby and J.W. Hutchinson, Strain gradient plasticity: Theory and experiment, *Acta Metall. Mater.* **42**, 475-487, 1994.
- [74] N.A. Fleck and J.W. Hutchinson (1997) Strain gradient plasticity. In J.W. Hutchinson and T.W. Wu (eds) *Advances in Applied Mechanics*, **33**, pp. 295-361.
- [75] A. Acharya and J.L. Bassani (1995) Incompatible lattice deformation and crystal plasticity. In N. Ghoniem (ed) *Plastic and Fracture Instabilities in Materials*, AMD-Vol. 200/MD- Vol. 57, pp. 75-80, ASME, New York.
- [76] A. Acharya and J.L. Bassani (1996) On non-local flow theories that preserve the classical structure of incremental boundary value problems. In A. Pineau and A. Zaoui (eds) *IUTAM Symp. on Micromechanics of Plasticity and Damage of Multiphase Materials* (Paris, Aug. 29- Sept. 1, 1995), pp. 3-9, Kluwer, Netherlands.
- [77] J.W. Hutchinson, Plasticity at the micron scale. In *Research Trends in Solid Mechanics (A report from the US National Committee on Theoretical and Applied Mechanics)*, to be published.
- [78] Q. Ma and D.R. Clarke, Size dependent hardness of silver single crystals, *J. Mater. Res.* **10**, 853-863, 1996.
- [79] V.P. Smyshlyaev and N.A. Fleck, The role of strain gradients in the grain size effect for polycrystals, *J. Mech. Phys. Solids* **44**, 465-495, 1996.
- [80] Z.C. Xia and J.W. Hutchinson, Crack tip fields in strain gradient plasticity, *J. Mech. Phys. Solids* **44**, 1621-1648, 1996.
- [81] Y. Wei and J.W. Hutchinson, Steady-state crack growth and work of fracture for solids characterized by strain gradient plasticity, *J. Mech. Phys. Solids* **45**, 1253-1273, 1997.
- [82] M.R. Begley and J.W. Hutchinson, The mechanics of size-dependent indentation, *J. Mech. Phys. Solids* **46**, 2049-2068, 1998.
- [83] J.Y. Shu, N.A. Fleck and W.E. King (1996) Bicrystals with strain gradient effects. In *Symposium on Interface Engineering for Optimized Properties, MRS Proceedings*, pp.295-300.
- [84] J.Y. Shu and C.Y. Barlow (1998) Strain gradient effects in the deformation of metal-matrix composites. In A.S. Khan (ed) *Constitutive and Damage Modeling of Inelastic Deformation and Phase Transformation (Plasticity '99)*, pp. 523-526, Neat Press, 1998.
- [85] Y. Huang, L. Zhang, T.F. Guo and K.C. Hwang, Mixed mode near-tip fields for cracks in materials with strain-gradient effects, *J. Mech. Phys. Solids* **45**, 439-465, 1997.
- [86] Z.Y. Chen and Y. Huang, Fracture analysis of cellular materials: A strain gradient model, *J. Mech. Phys. Solids* **46**, 789-828, 1998.
- [87] W.D. Nix and H. Gao, Indentation size effects in crystalline materials: A law for strain gradient plasticity, *J. Mech. Phys. Solids* **46**, 411-425, 1998.
- [88] J.S. Stolken and A.G. Evans, A microbend test method for measuring the plasticity length scale, *Acta Materialia* **46**, 5109-5115, 1998.

- [89] J.S. Stolken (1997) *The role of oxygen in nickel-sapphire interface structure*. PhD dissertation, University of California, Santa Barbara.
- [90] W.D. Nix, Mechanical properties of thin films, *Metall. Trans.* **20A**, 2217-2245, 1997.
- [91] W.D. Nix and H. Gao, Indentation size effects in crystalline materials: A law for strain gradient plasticity, *J. Mech. Physics Solids*, **46**, 411-425, 1998.
- [92] N.A. Stelmashenko, A.G. Walls, L.M. Brown and Y.V. Milman, Microindentations on W and Mo oriented single crystals: An STM study, *Acta Metall. Mater.* **41**, 2855-2865, 1993.
- [93] W.J. Poole, M.F. Ashby and N.A. Fleck, Micro-hardness of annealed and workhardened copper polycrystals, *Scripta Metall. Mater.* **34**, 559-564, 1996.
- [94] D.J. Lloyd, Particle reinforced aluminum and magnesium matrix composites, *Int. Mater. Reviews* **39**, 1-23, 1994.
- [95] E.C. Aifantis (1996) Higher order gradients and size effects. In A. Carpinteri (ed) *Size-scale Effects in the Failure Mechanisms of Materials and Structures*, pp. 231-242, E. & F.N. Spon, Chapman and Hall, London.
- [96] I. Vardoulakis and E.C. Aifantis (1995) Heterogeneities and size effects in geomaterials. In A. Misra and C.S. Chang (eds) *Mechanics of Materials with Discontinuities and Heterogeneities*, AMD-Vol. 201, pp. 27-30, ASME, New York.
- [97] H.T. Zhu, H.M. Zbib and E.C. Aifantis, Strain gradients and continuum modeling of size effect in metal matrix composites, *Acta Mechanica* **121**, 165-176, 1997.
- [98] D.J. Unger and E.C. Aifantis, The asymptotic solution of gradient elasticity for model III, *Int. J. Fracture* **71**, R27-R32, 1995.
- [99] G. Exadaktylos, I. Vardoulakis and E.C. Aifantis, Cracks in gradient elastic bodies with surface energy, *Int. J. Fracture* **79**, 107-119, 1996.
- [100] I. Vardoulakis, G. Exadaktylos and E.C. Aifantis, Gradient elasticity with surface energy: Mode III crack problem, *Int. J. Struct.* **33**, 4531-4559, 1996.
- [101] M.Yu. Gutkin and E.C. Aifantis, Screw dislocation in gradient elasticity, *Scripta Materialia* **35**, 1353-1358, 1996.
- [102] M.Yu. Gutkin and E.C. Aifantis, Edge dislocation in gradient elasticity, *Scripta Materialia* **36**, 129-135, 1997.
- [103] K.S. Kim (1997) Nanomechanics of dislocation cores and their instability. 2nd Euroconference and International Symposium on Material Instabilities in Deformation and Fracture, 31 August - 4 September, Thessaloniki.
- [104] X.H. Zhu, Theoretical Analysis of Sheet Metal Formability, Ph.D. Dissertation, Michigan Technological University, 1999.
- [105] J. Huang, Adiabatic Shear Banding and Shear Localized Chip Formation, Ph.D. Dissertation, Michigan Technological University, 2000.
- [106] W.W. Milligan, S.A. Hackney and E.C. Aifantis, Observations and modelling of deformation and fracture in nanostructural materials, in: *AFOSR Mechanics of Composites Review*, pp. 1-10, Wright Patterson Lab, 1992.
- [107] W.W. Milligan, S.A. Hackney and E.C. Aifantis, Deformation and damage at the nanoscale: Preliminary observations and modelling, in: *Damage Mechanics & Localization*, AMD - Vol. 142/MD-Vol. 34, Eds. J.W. Ju and K.C. Valanis, pp. 153-165, ASME, 1992.
- [108] W.W. Milligan, S.A. Hackney, M. Ke and E.C. Aifantis, In situ studies of deformation and fracture in nanophase materials, *Nanostructured Materials* **2**, 267-276, 1993.
- [109] M. Ke, W.W. Milligan, S.A. Hackney, J.E. Carsley and E.C. Aifantis, HREM study of fracture and deformation behavior of nanostructured thin films, in: *Thin Films-Stresses and Mechanical Properties*, MRS Proc. Vol. 308, pp. 565-569, MRS, 1993.
- [110] J.E. Carsley, J. Ning, W.W. Milligan, S.A. Hackney and E.C. Aifantis, A simple, mixtures-based model for the grain size dependence of strength in nanophase metals, *Nanostructured Materials* **5**, 441-448, 1995.

- [111].M. Ke, S.A. Hackney, W.W. Milligan, and E.C. Aifantis, Observation and measurement of grain rotation and plastic strain in nanostructured metal thin films, *Nanostructured Materials* **5**, 689-698, 1995.
- [112].J.E. Carsley, W.W. Milligan, S.A. Hackney and E.C.Aifantis, Glass-like behavior in a nanostructured Fe/Cu alloy, *Metallurgical Transactions* **26A**, 2479-2481, (1995).
- [113].W.W. Milligan, S.A. Hackney and E.C. Aifantis, (1995) Constitutive modeling for nanostructured materials, in: *Continuum Models for Materials with Microstructure*, Ed. H.B. Muhlhaus, pp. 379-393, Wiley
- [114].J.E. Carsley, W.W. Milligan, S.A. Hackney and E.C. Aifantis, (1996) Deformation mechanisms in bulk Fe - 10% Cu nanostructures, in: *Processing and Properties of Nanocrystalline Materials*, Eds. C. Suryanarayana et al, pp. 415-420, TMS, Warrendale, PA.
- [115] S. Hackney, M. Ke, W.W. Milligan and E.C. Aifantis, (1996) Grain size and strain rate effects on the mechanisms of deformation and fracture in nanostructured metals, in: *Processing and Properties of Nanocrystalline Materials*, Eds. C. Suryanarayana et al, pp. 421-426, TMS, Warrendale, PA.
- [116] X.H. Zhu, J.E. Carsley, W.W. Milligan, and E.C. Aifantis, On the failure of pressure-sensitive plastic materials: Part I. Models of yield and shear band behavior, *Scripta Materialia* **36**, 721-726, 1997.
- [117] J.E. Carsley, W.W. Milligan, X.H. Zhu and E.C. Aifantis, On the failure of pressure-sensitive plastic materials: Part II. Comparisons with experiments on ultra fine grained Fe-10% Cu alloys, *Scripta Materialia* **36**, 727-732, 1997.
- [118] J.E. Carsley, G.R. Shaik, W.W. Milligan and E.C. Aifantis, (1997).Mechanical behavior of bulk nanostructured Fe/Cu alloys, *Symp. Chemistry and Physics of Nanostructures and Related Non-equilibrium Materials*, Eds. E. Ma et al, pp. 183-192, TMS, Warrendale, PA
- [119] J.E. Carsley, A. Fisher, W.W. Milligan and E.C. Aifantis, Mechanical behavior of a bulk nanostructured iron alloy, *Metallurgical and Materials Transactions* **29A**, 2261-2271A, 1998.
- [120] H. Gao, Y. Huang, W.D Nix, J.W Hutchinson, Mechanism-based strain gradient plasticity I.Theory, *Journal of Mechanics and Physics of Solids*, **47**, 1239-1263, 1999.
- [121] J. Huang and E.C. Aifantis, A note on the problem of shear localization during chip formation in orthogonal machining, *J. Mater. Engng. & Performance* **6**, 25-26, (1997).
- [122] A.E. Bayoumi, J.Q. Xie, Some Metallurgical Aspects of Chip Formation in Cutting, *Mater. Sci. and Eng. A* **190**, 173-180, 1995.
- [123] R.W. Siegel, Nanostructured materials-Mind over matter, *Nanostructure Materials*, **3**, 1-18, (1993).
- [124] H. Gleiter, *Prog. Nanocrystalline Materials*, *Progress in Materials Science*, **33**, 223-315, 1989.
- [125] A.H. Chokshi, A. Rosen, J. Karch, and H. Gleiter, *Scripta Metallurgica*, **23**, 1679-1684, 1989.
- [126] G.E. Fougere, J.R. Weertman, R.W. Siegel, and S. Kim, *Scripta Metall. Mater.*, **26**, 1879-1883, 1992.
- [127] S.A. Hackney and W.W Milligan, A new in situ technique for studying deformation and fracture in thin film ductile/brittle materials, *Ultramicroscopy*, **37**, 79-89, 1991.
- [128] E.P. Popov, *Introduction to the Mechanics of Solids*, Prentice-Hall, Englewood Cliffs, NJ, 312, 1968.
- [129] G.E. Dieter, *Mechanical Metallurgy*, 3rd Edition, McGraw-Hill, New York, 88, 1986.
- [130] G.R. Shaik, and W.W. Milligan, Consolidation of nanostructured metal powders by rapid forging: processing, modeling, and subsequent mechanical behavior, *Metallurgical and Materials Transactions A* **28A**, 895-904, 1997.
- [131] E.C Aifantis, Gradient effects at macro, micro, and nano scales, *Journal of Mechanical Behavior of Materials*, **5**, 355, 1994.
- [132] E.C. Aifantis, (1993) Higher order gradients and self-organization at nano, micro, and macro scales, in: *Continuum Models for Discrete Systems CMDS-7 (Materials Science Forum, Vols. 123-125)*, Eds. K.H. Anthony and H.J. Wagner, pp. 553-566, Trans. Tech. Publ.
- [133] G.E. Dieter, *Mechanical Metallurgy*, 3rd Edition, McGraw-Hill, New York, 455, 1986.
- [134] J. P. Hirth, and J. Lothe, (1982) *Theory of Dislocations*, Wiley, NY, 731-745.

- [135] A. K. Mukherjee, (1975) Grain Boundaries in Engineering Materials, Claitor Publishing, Baton Rouge, LA, 93.
- [136] J.E. Carsley, Mechanical Behavior of Nanostructured Metals, Ph.D. Dissertation, Michigan Technological University, 1996.
- [137] T.W. Webb, X.H. Zhu and E.C. Aifantis, A simple method for calculating shear band angles for pressure-sensitive plastic materials, *Mech. Res. Comm.* **24**, 69-74, 1997.
- [138] R. Hill, *J. Mech. Phys. Solids*, **1**, 19, 1952.
- [139] E.C. Aifantis and J.B. Serrin, The mechanical theory of fluid interfaces and Maxwell's rule, *Journal of Colloid and Interface Sciences* **96**, 517-529, 1983.
- [140] E.C. Aifantis and J.B. Serrin, Equilibrium solutions in the mechanical theory of fluid microstructures, *Journal of Colloid and Interface Sciences* **96**, 530-547, 1983.